Charles University in Prague

Faculty of Mathematics and Physics

DOCTORAL THESIS

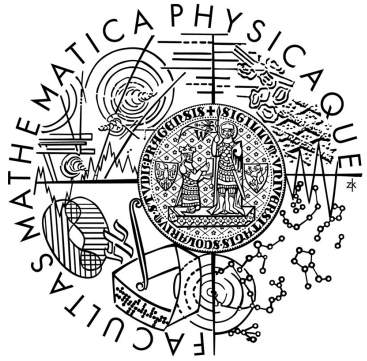

Igor Píš

Electronic structure of bimetallic systems - study of gas molecule interaction

Department of Surface and Plasma Science

Supervisor of the doctoral thesis:
doc. RNDr. Václav Nehasil, Dr.

Study programme: Physics

Specialization: F-5 Surface and Interface Physics

Prague 2013

Acknowledgement

First of all, I would like to thank to my supervisor doc. RNDr. Václav Nehasil, Dr., to whom I am grateful for his guidance, valuable advices, discussions and help. Then I would like to give my thanks to people who helped me with experiments at the Materials Science Beamline at Elettra synchrotron, namely to RNDr. Ing. Tomáš Skála, Ph.D., Mgr. Jiří Libra, Ph.D., Mgr. František Šutara, Ph.D., Mgr. Miloš Cabala, Mgr. Michal Škoda, Ph.D., Mgr. Martin Vondráček and Bc. Miroslav Kettner. For the assistance with STM measurements, I am thankful to RNDr. Josef Mysliveček, Ph.D., Mgr. Vitalii Stetsovych and Mgr. Filip Dvořák. Many thanks also belong to Professor Spyridon Ladas and Manos Symianakis for their help during my stay at the University of Patras. Special thanks belong to all the members of the Surface Physics Group for their valuable help with many technical and scientific problems and for the very motivating environment.

I declare that I carried out this doctoral thesis independently, and only with the cited sources, literature and other professional sources.

I understand that my work relates to the rights and obligations under the Act No. 121/2000 Coll., the Copyright Act, as amended, in particular the fact that the Charles University in Prague has the right to conclude a license agreement on the use of this work as a school work pursuant to Section 60 paragraph 1 of the Copyright Act.

In Prague, February 4, 2013

Igor Píš

Název práce: Změny elektronické struktury bimetalických systémů při interakci s molekulami plynu

Autor: Igor Píš

Katedra / Ústav: Katedra fyziky povrchů a plazmatu

Vedoucí doktorské práce: doc. RNDr. Václav Nehasil, Dr., Katedra fyziky povrchů a plazmatu

Abstrakt: Práce je věnována studiu bimetalického Rh–V systému pomocí metod fyziky povrchů. Vlastnosti ultra-tenkých Rh–V vrstev nesených na γ-Al_20_3 byly porovnány s modelovými systémy připravenými vakuovou depozicí V na Rh(111), Rh(110) a polykrystalické rhodium. Bylo zkoumáno vytváření V–Rh(111)–(2×2), V–Rh(110)–(2×1) a V–Rh(110)–(1×2) podpovrchových slitin a jejich elektronická a atomární struktura. Byly navrženy modely povrchových rekonstrukcí těchto slitin. Dále byl zkoumán vliv vzniku podpovrchové slitiny na interakci s molekulami CO a O_2 a vliv adsorpce molekul na tuto slitinu. Vazba mezi CO molekulami a povrchem slitiny byla oslabena v důsledku markantních změn ve struktuře valenčního pásu kovového povrchu. Kyslík adsorbovaný na povrchu slitiny reagoval při zvýšené teplotě s podpovrchovým vanadem, což zabraňovalo interakci kovového substrátu s molekulami CO.

Klíčová slova: Rh, V, povrchová slitina, adsorpce CO, kyslík

Title: Electronic structure of bimetallic systems - study of gas molecule interaction

Author: Igor Píš

Department / Institute: Department of Surface and Plasma Science

Supervisor of the doctoral thesis: doc. RNDr. Václav Nehasil, Dr., Department of Surface and Plasma Science

Abstract: Bimetallic Rh–V system was studied by means of surface science experimental methods. Properties of ultra-thin Rh–V layers supported by γ-Al_20_3 were compared with model systems prepared by vacuum V deposition on Rh(111), Rh(110) and polycrystalline rhodium. Formation of ordered V–Rh(111)–(2×2), V–Rh(110)–(2×1) and V–Rh(110)–(1×2) subsurface alloys and their electronic and atomic structure were investigated and models of the surface reconstructions were proposed. Influence of the subsurface alloy formation on interaction with CO and O_2 molecules as well as the influence of the molecule adsorption on this alloy was investigated. The bond between CO molecules and Rh–V alloy surface was weakened due to pronounced changes in surface valence band structure. Oxygen which adsorbed on the alloy surface reacted with the subsurface vanadium at elevated temperature and blocked the interaction of the metal substrate with CO molecules.

Keywords: Rh, V, surface alloy, CO adsorption, oxygen

Contents

1 INTRODUCTION

1.1 Solid metal catalysts and heterogeneous catalysis

Any real solid material is terminated by surfaces. The atoms at surfaces are at different environment as their bulk counterparts. They have unsaturated valencies which originate mainly in the lower coordination numbers, i.e. number of bonded neighbour atoms. The free valencies on surface are in reach of the molecules from the gas or liquid phase surrounding the solid material and may form bonds with them. The bonds can be so intense that the electronic structure and the spatial distribution of the electron charge around the chemisorbed molecule can change its reactivity. This is the basic principle underlying the phenomenon of heterogeneous catalysis on solid surfaces [1].

A huge fraction of all industrial chemical processes involve heterogeneous catalysis. Typically, the solid catalyst is situated inside a reactor, which is operated in continuous gas flow. Reactants enter the reactor at the inlet, react inside the reactor and products leave the reactor at the outlet. Under steady-state conditions, the rate of the catalytic reaction inside the reactor is determined by the external parameters, such as partial pressures, temperature, flow rate and by the nature of the catalyst. The basic elementary processes involved on the solid catalyst are depicted in Fig. 1.1.

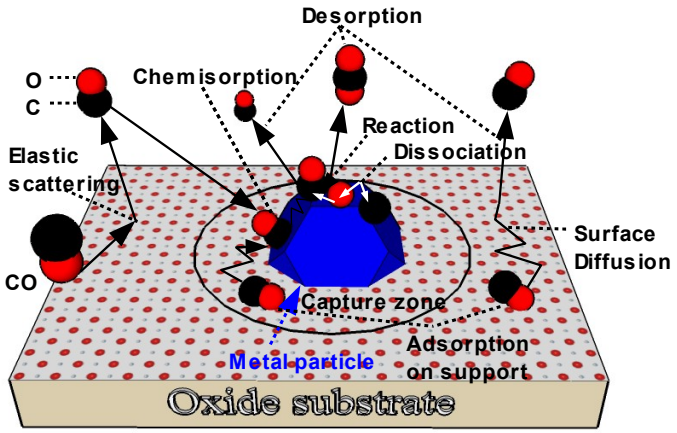

Fig. 1.1 The principle of heterogeneous catalysis. A model of CO to CO_2 conversion mechanism on a supported metal particle.

The first elementary process necessary in heterogeneous catalysis is the adsorption of at least one of the reactants on a solid surface. The molecular

adsorption can be either non-dissociative or dissociative. The next step is the surface diffusion of the adsorbates and then their surface reaction to product molecules. The final step is desorption from surface. Surface reaction can occur either as soon as the adsorbed reactants are close enough to each other for a sufficient period of time (Langmuir-Hinshelwood and Eley-Rideal mechanisms) or after diffusion of at least one of the reactants to a specific active site.

Since heterogeneous catalysis is a surface phenomenon, the rate of the reaction is proportional to exposed catalyst surface. It is desirable to maximize the specific surface area of the catalyst. This can be achieved by designing highly porous materials. On the other hand, if a precious metal is the active catalyst, it is optional to reduce the amount of the catalyst to very thin layers. But a few monolayers (ML) of metals lack mechanical strength. Therefore, they are deposited on high surface area ceramic supports such as alumina, magnesia, silica or ceria. Supported metal catalysts have typically shape of nanometre-sized particles (nanoparticles) that expose different crystal phases with various structural defects. The size of the dispersed particles can have considerable influence on the overall reactivity. If nanoparticles consist of more than one component (bimetallic catalysts, for instance) the surface composition may be very different from that of the bulk. Thus metal nanoparticles may exhibit electronic properties and hence chemical reactivity different from those of the bulk material.

Structure and composition of a real catalyst as well as the reaction mechanism of catalysis are often highly complex. Any direct study of the catalyst and catalysis under working conditions is almost unachievable task. Therefore, surface science approach have been employed in order to get closer insight into the nature of the catalysts and elementary steps involved in heterogeneous catalysis on solid surfaces.

The goal in the research of catalysts and catalysis is to obtain such broad knowledge of the catalytic mechanism that will enable to describe and predict the kinetics of catalytic reactions on the catalyst. It means to identify all possible reaction intermediates, active sites of the catalyst, rate constants of elementary steps and to identify possible structural and morphological influence of the reactants on the catalyst. Sometimes it is sufficient to identify the rate-limiting step. Understanding such step enables designing new catalysts with higher activity. Heterogeneous catalysts may create several side-products and sometimes the formation of a desired

molecule or the suppression of the formation of an undesired molecule becomes more important than the overall reactivity. It is related to the selectivity of the catalyst.

1.2 Model catalysts

The surface science approach to research of catalysts by studying well defined single-crystal surfaces have already been proposed by Irving Langmuir in the beginning of 20th century. The strategy is based on attention focused on plane surfaces and reactions on them. If the principles at well-defined plain surfaces are well understood, we should be able to extend the theory to the case of more complex catalysts.

The surface science approach became fully available after the introduction of ultra-high vacuum (UHV) techniques and development big variety of surface physical methods. It has, however, two main disadvantages which are usually referred as "pressure" and "materials gap".

Most of the surface science techniques can not be operated under high-pressure conditions typical for catalytic reactions used, for instance, in industry. Reaction mechanisms at surfaces can be different at ultra low-pressures and we talk about the "pressure gap". By the "materials gap", it is meant that the properties of well-defined single-crystal surfaces may be quite different from the surface properties of real catalyst with a complex surface structure. Moreover, both "gaps" might be tightly linked together. For instance, the surface of a catalyst can be structurally or chemically altered at high pressures. A good example demonstrating the appearance of the both "gaps" is the CO oxidation on Ru catalysts [1]. While CO oxidation mechanism and kinetics on Rh, Pt, and Pd are similar for supported catalysts and single crystals, this is not true for Ru. Ruthenium supported catalysts at atmospheric pressure have been found more reactive than the other metals. On the contrary, Ru single-crystals have been found much less active under UHV conditions [2]. The existence of the pressure gap was finally explained by the formation of a thin RuO_2(110) overlayer on top of the Ru(0001) surface in an oxidizing atmospheric pressure and at elevated temperature [3]. The RuO_2(110) surface posses coordinatively unsaturated Ru atoms on which CO and oxygen adsorb. The adsorbed molecules react following the Langmuir-Hinshelwood with significantly lower

activation energy as at the Rh(0001) surface. Later it was discovered that the most active supported Ru catalysts are the so-called core-shell nanoparticles with Ru metal core covered by an ultra-thin RuO_2(110) and (100) shell [4]. The similarity between the single-crystal model and supported catalyst is evident and this example shows that it is possible to bridge the materials and pressure gap.

The materials and pressure gap can be bridged by different ways. One of them is systematic study with the use of different single-crystal surfaces; different bimetallic or multimetallic alloy surfaces; surfaces with well-defined defects; surfaces doped by other elements; comparative studies on supported particles with different but well known sizes; etc.

Some details about reaction mechanisms can be obtained by studying backward reactions, since they proceed through the same intermediate microscopic steps.

A useful concept to study the chemical properties of an oxide-metal phase boundary is the so-called "inverse model catalyst" approach. This type of model catalyst consists of metal single crystal surface decorated by submonolayer coverages of atomically ordered oxide islands.

Vapour deposited thin metal and mixed metal films on an oxide substrate can be considered as a step between well defined model catalysts and complex real catalysts. The main difference between a single-crystal model catalyst and supported thin film is the presence of the substrate. Supported metal systems are influenced by the interaction with the support. The influence of the support might be straightforward through the strong bonding with the metal atoms or indirect, by influencing the structure and morphology of the metal films or particles. In the case of supported mixed films, the relations between the constituents, their influence on the interaction with the support and vice versa must be considered.

Thin metal films or particles vapour deposited on well-defined oxide surfaces, under clean UHV conditions, serve as a useful model of real catalysts. Such model catalysts are accessible to the surface science techniques, which make possible to study fundamental details of their catalytic behaviour. Besides, under well defined and controlled conditions typical for surface science experimental systems, it is possible to design a catalyst with novel catalytic properties.

1.3 Bimetallic systems

Bimetallic systems with nanometre dimensions may form structures and phases which have no bulk counterparts. These materials may exhibit novel properties, which originate from spatial confinement to atomic dimensions, mixing of otherwise immiscible metals, novel heteroatomic metal-metal bonds, etc. The formation of a bimetallic surface or subsurface alloy can have tremendous effects on the reactivity of metal catalyst.

One of the possible desirable effect of the presence of the second metal constituent is the possibility of having two different reactions occurring simultaneously on different metallic centres. An example is three-way catalyst (TWC) for car exhausts. The typical TWC contains Pt-Rh alloys, where CO is oxidized and NO reduced [5].

Another desirable effect in a bimetallic system can be alloying which can induce an increase in the yield of a specific reaction by reducing the energy barrier of the rate-limiting step in the reaction mechanism. An example is the approximately five-fold increase of the catalytic activity of Rh surfaces after alloying with V in hydrogenation of CO (Fig. 1.2).

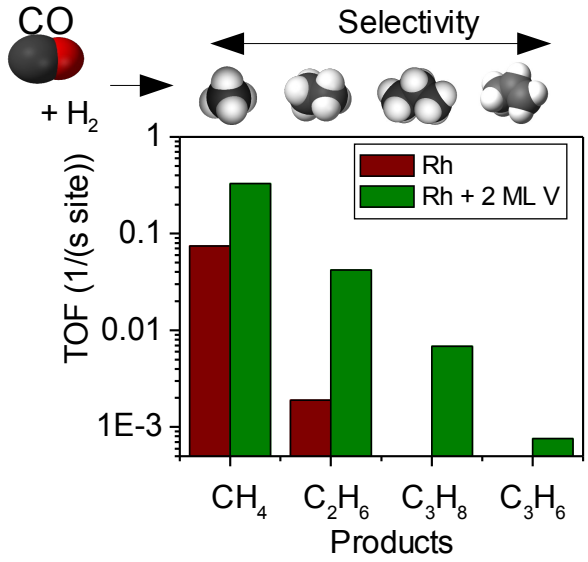

Fig. 1.2: Activity (Turn Over Frequency-TOF) and selectivity of bare polycrystalline Rh foil and the Rh foil with 2 ML of V annealed at 950 K. Reaction conditions: 40 mbar CO, 360 mbar H_2, 600 mbar He, 573 K [6].

Alloying can open up new chemical reaction pathways or suppress undesired side products by altering the selectivity. Furthermore, the presence of the second metal

constituent can prevent the main metal constituent from poisoning and thus from the deactivation of the surface. The second metal can also stabilize the surface structure under reaction conditions. On the other hand, the second metal constituent can have undesired effects, such as deactivation of the active sites of a specific reaction, or it can react with the gas reactants and cover the metal catalyst with an inert layer.

The altered catalytic properties can be often rationalized by concepts of "electronic" and "ensemble" effects. The "ensemble" requirement for reaction on surface is usually connected with the group of active sites on the surface which is necessary for a particular reaction. Undesired reactions can be suppressed by removing or poisoning the responsible active sites. An example of the "ensemble" effect is complete suppression of O_2 adsorption on the $(\sqrt{3}\times\sqrt{3})$R30° Sn-Rh(111) surface alloy at room temperature and low pressures [7]. Molecules of O_2 adsorb dissociatively on the clean Rh(111) surface and the dissociated oxygen atoms sit in three-fold fcc-hollow sites. Such sites are not available on the $(\sqrt{3}\times\sqrt{3})$R30° Sn-Rh(111) surface alloy, where each three-fold hollow site is affected by the presence of a tin atom which substituted the surface Rh atom.

"Electronic" effects refer to altered catalytic properties which originate in the altered electronic structure of the surface induced by metal-metal bonding. A good example is the change of the strength of the CO bond with metal surface atoms induced by electronic changes upon alloying with other metals [8,9].

Sometimes the situation is more complex and both concepts must be considered simultaneously. Understanding the ensemble and electronic effects can be effectively exploited in the control of the activity and selectivity of chemical reactions on solid catalysts. The development of new heterogeneous catalysts can benefit a lot from the surface science studies of model catalysts such as those presented in this work.

In the case of supported mixed bimetallic films, the relations between metal A – metal B, metal A-support, and metal B-support interactions must be considered. An example which demonstrates some extraordinary phenomena on supported nano-sized bimetallic layers is Ni-Co ultra-thin layer deposited on oxygen terminated ZnO $(000\bar{1})$ surface [10]. This bimetallic system demonstrates how the morphology, chemical composition, and structure can be significantly influenced by the bimetallic interaction and by the interaction between the constituents and the support. A schematic model depicting behaviour of the bimetallic layer under certain

experimental conditions is shown in Fig. 1.3. It has been observed that at room temperature and at low metal coverage, cobalt is partially oxidized, while nickel remains in zero valence. When the bimetallic Ni-Co layer was annealed at 773 K in UHV, the oxidation state of Ni and Co remained unaffected, in high contrast with monometallic Ni and Co layers. The monometallic layers treated under the same conditions were extensively oxidized upon a strong interaction with the substrate. The synergy interaction between Ni and Co strongly affected the metal-support interaction. On the other hand, the annealing influenced the morphology by stimulating a significant agglomeration and cobalt surface segregation. The agglomeration was more pronounced on the O-terminated ZnO surface in comparison to Zn-terminated surface, which is another example of the support influence.

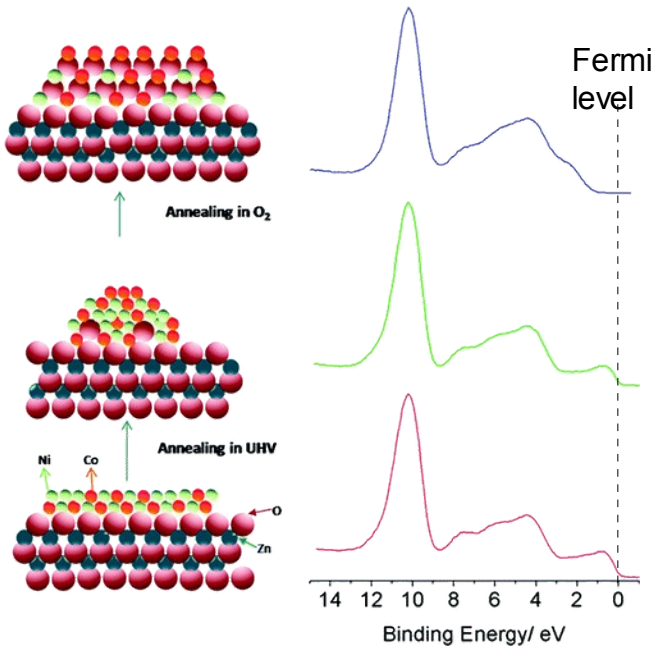

Fig. 1.3 (Left) Schematic model of Ni-Co ultrathin bimetallic layer on $(000\bar{1})$ ZnO substrate and (right) corresponding valence band photoelectron spectra. From [10].

Due to the great importance in many industrial applications, supported Rh model catalyst has been investigated extensively [11-16]. A lot of studies have been devoted to the investigation of chemisorption properties of Rh thin films and particles on oxides, which are very important in understanding basic processes occurring on oxide-supported metal catalysts. Gas surface interaction plays a crucial role in

catalytic reactivity. CO has been used widely as a probe molecule to study adsorption processes on various types of well ordered surfaces. It has been shown how the CO chemisorption properties depend on average particle size or film thickness and morphology [17].

As it has been mentioned before, bimetallic systems can exhibit chemical and catalytic properties that are very different from those of the surfaces of the individual metals. The metal-metal surface bonding can produce significant perturbations in the electronic properties of a metal [9] and/or form very original structure that leads to some special catalytic properties. Such interaction is often exhibited between early (such as V) and late-transition (such as Rh) metals with a significant difference in *d*-band occupation.

In general, the magnitude of the perturbations depends on the relative position of the metal constituents in the Periodic table. The strongest metal-metal interaction has been observed in systems that combine late-transition metals with almost fully occupied valence band and metals with almost empty valence band (s,p metal and early-transition metals). These electronic perturbations have enormous influence on the reactivity of metal surface. The formation of bimetallic bonds is often accompanied with core-level shifts in energy.

Rodriguez and Goodman showed a strong correlation between the surface core level shift (SCLS) at binding energy scale and CO chemisorption energy [8]. The larger the shift in binding energy (BE) towards higher values the lower CO adsorption energy. On the other hand, a shift in binding energy towards lower values increases the strength of the bond between the metal and CO molecule. It was observed that the shifts in the core levels usually track shifts in their valence *d* bands. Generally, the larger the shift in the core-level the larger shift of the centre-of-mass of the valence band. The shift of the valence band centroid to the higher BE is often connected with reduction of the density of states (DOS) near the Fermi level.

In order to explain the correlation between the electronic structure perturbations and CO-metal bond strength change, the nature of the CO adsorption bond must be considered. The bonding between CO and metal surface involves electron transfer from the 5σ CO orbital into the empty bands of the metal (σ-donation), and electron transfer from the occupied bands of the metal into the CO $2\pi^*$ orbital (π-backdonation) [18]. A significant contribution to the metal-CO bond comes from the

hybridization or mixing of the metal *d* band with CO $2\pi^*$ orbital. Several density-functional theory studies showed, that *d*-electron states near the Fermi level are responsible for the CO 2π-backbonding [9]. The weakening or strengthening of the CO-metal bond thereby originates in the reduction or raise of the π-backbonding.

Hammer et. al. introduced a theoretical model of CO chemisorption on metal surfaces and overlayers [19] which rationalized the results by Rodriguez and Goodman [8]. According to this model, the CO adsorption energy on metal surface should be roughly proportional to the occupancy N_d of the metal *d* band, and inversely proportional to the separation between the *d*-band centroid and the CO $2\pi^*$ orbital:

$$E_{ad}^{CO} \propto \frac{N_d}{\left(E_{CO2\pi} - E_{M(d)}\right)} \tag{1}$$

1.4 Rh–V bimetallic systems

Noble metals such as Rh, Pd or Pt are widely used as three-way catalysts in gas-exhaust catalysis to convert toxic CO to CO_2 and NO to N_2 [5]. The efficiency of a noble metal three-way catalyst can be significantly enhanced on bimetallic surfaces like Pd/Rh or Pt/Rh. Despite the fact that the technology of gas-exhaust catalysis is on very good level nowadays, there is still a search for new materials for more efficient low-temperature NO_x reduction.

In recent years, the attention of materials science research has been extensively focused on new clean sources of energy. A promising technology is the production of electrical power with the help of hydrogen fuel cells. Hydrogen as gas is rather difficult and hazardous to store and transport. Therefore, it is desirable to convert hydrogen into liquid products such as methanol from which it can be extracted on demand. One of the ways how to extract hydrogen form methanol is steam reforming. Catalyst required for methanol steam reforming must posses high stability, high catalytic activity and the suppression of carbon monoxide at low temperatures. Until now, the most common catalysts used in methanol steam reforming have been based on Cu [20]. However, the Cu based catalysts are pyrophoric and are easily deactivated by thermal sintering. Group 8–10 catalysts have been reported as highly stable but with lower reactivity and selectivity in

comparison with copper-based catalysts. On the other hand, bimetallic alloys of the 8–10 catalysts exhibited catalytic properties approaching those of copper-based catalysts.

The alloy surfaces consisting of early (such as V) and late transition metals (such as Rh or Pd) have become of a particular interest since a strong *d–d* hybridization between the element with almost full and almost empty valence band can result in a unique electronic structure with an extraordinary influence on surface reactivity.

Several studies employing different surface science techniques have been devoted to Pd–V and Rh–V model systems [9,21-24]. Structure, adsorption properties and reactivity have been studied by means of Scanning Tunnelling Microscopy (STM), Auger electron spectroscopy, low energy ion spectroscopy, temperature programmed desorption (TPD) and molecular beam methods as well as by *ab-initio* DFT calculations. It has been shown that, under certain conditions, stable subsurface alloys are formed with V atoms located in the second atomic layer. These subsurface alloys exhibited some extraordinary catalytic properties. Carbon monoxide hydrogenation and methanol dehydrogenation were chosen as model catalytic reactions to probe the catalytic behaviour of the bimetallic alloys. In both cases the activity was significantly enhanced on the alloys in comparison with pure noble metals. There is strong evidence that the enhanced reactivity originates mainly in the electronic structure changes at the surface. The centre of *d*-band shifts from the Fermi level to higher binding energies due to a strong *d–d* hybridization. As a result, bonding of simple molecules such as CO and H_2 with metal surface is weaker on the alloy surface and leads to an increase in the reactivity. This explanation was proposed on the basis of detailed theoretical study of Hirschl and Hafner[25,26] and experiments [24] on Pd–V surface and subsurface alloys. However, Rh–V surface and subsurface alloys have not been studied in this way.

Results of the previous research on Rh–V bimetallic systems will be summarised in next paragraphs. An excellent review of the Pd–V and Rh–V model system properties can be also found in [27].

In the beginning, it is quite informative to examine the constitution diagram for bulk Rh–V alloy system. The experimentally determined constitution diagram [28] gives six intermediate phases, which are summarised in Tab.1. Stability of fcc-based bulk Rh–V alloys was investigated by *ab-initio* calculations [29]. Three ground state

structures were derived: an $L1_0$ of RhV stoichiometry (formation energy E_{for} = -510 meV/atom) and two $L1_2$ structures of Rh_3V (E_{for} = -432 meV/atom) and RhV_3 (E_{for} = -326 meV/atom) with ordering energies -163, -153 and -89.5 meV/atom, respectively. The calculations indicate that RhV and Rh_3V compounds are thermodynamically favoured. Structure models of these two phases are displayed in Fig. 1.4.

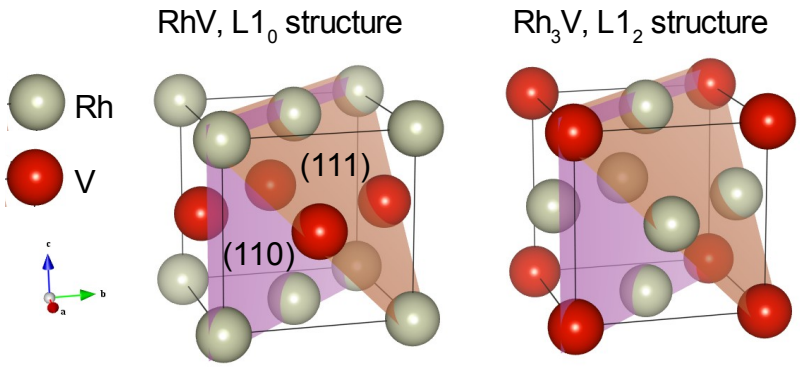

Fig. 1.4: Ball models of the structures of the most stable Rh–V ordered bulk alloys predicted by ab initio calculations [29].

Phase	Crystal system	Structure type	Space group	Space gr. number	Composition limits (at.% V; T)
γ–Rh	Cubic	Cu	Fm-3m	225	0– ~19; 1573 K
γ'–VRh_3	Cubic	$L1_2$, $AuCu_3$	Pm-3m	221	23.0–33.5; 1573 K
ε–V_3Rh_5	Orthorhombic	$V(V_{0.5}Rh_{0.5})Rh_2$	Cmcm	63	37.0– ~38.5; 1573 K
α_2–$(V_{0.88}Rh_{0.12})Rh$	Tetragonal	$L1_0$, AuCu	P4/mmm	123	40.5–47.5; 1573 K
α_3–VRh	Orthorhombic	α–VIr	Cmmm	65	49.0–52; 1373 K
α_1–VRh	Unknown	Unknown	-	-	50.0–55; 1793 K
β–V_3Rh	Cubic	A15, Cr_3Si	Pm-3n	223	61.0–75.5; 1793 K
α–V	Cubic	W	Im-3m	229	~84–100; 1793 K

Table 1: Crystallographic data for V–Rh phases [28].

It was found that a stable V–Rh subsurface alloy can be obtained by annealing vanadium metal overlayers on polycrystalline rhodium and single-crystal Rh(111) substrates at a temperature of 773 K and higher [6,23]. At 423 K, vanadium is still on top of the surface. After annealing at 950 K, the top layer consists exclusively of rhodium atoms with V in located in near-surface layers. The structure and

composition as a function of nominal vanadium coverage and temperature treatment were studied. It was found that the composition of the near-surface layers is almost independent of the amount of V deposits between 1 and 2.5 ML after heating to 950 K. With increasing initial V coverage excess vanadium is dissolved in the rhodium bulk after the high temperature annealing.

Initial stages of the growth of V on Rh(111) at different substrate temperatures were characterized in the work [30]. Sub-monolayer and monolayer amount of V was deposited onto the Rh(111) at room temperature. Three-dimensional island growth with pseudomorphic first V layer was observed. The samples were annealed after the deposition. Significant diffusion of the V to subsurface layers was observed at temperatures higher than 673 K. At a temperature of 673 K a few small domains with a (2×2)–V–Rh(111) substitutional surface alloy were observed by STM. The V diffusion from the first layer to deeper layers was complete after the samples with 0.5 ML and lower V deposits were annealed at 823 K. On the other hand, some amount of V remained on the surface even after the annealing at 823 K when the amount of deposited V was equal to 1 ML.

The (2×2)–V–Rh(111) surface alloy observed at 673 K disappeared after the annealing at 823 K and triangular-like features formed by Rh atoms appeared. The V atoms situated in the second layer induced appearance of small surface areas with Rh atoms in (2×2) and $(\sqrt{3}\times\sqrt{3})R30°$ reconstruction. The heat of formation of the surface and subsurface Rh(111)–V alloys as a function of V concentration was estimated from first-principles calculations. The calculations showed that the alloying is an exothermic process and the most stable structure was predicted for the V concentration of 0.25 which corresponds to the (2×2) phase. Models of the subsurface V–Rh(111) alloys with corresponding surface reconstruction have been proposed as displayed in Fig. 1.5.

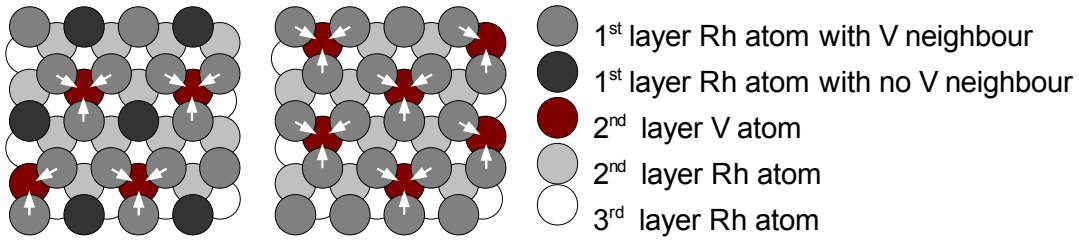

Fig. 1.5: Models of V–Rh(111) subsurface alloys with (2×2) (left) and $(\sqrt{3}\times\sqrt{3})R30°$ *(right) reconstructions proposed by Konvicka [30]. The arrows indicate the direction of surface atoms lateral contraction.*

Carbon monoxide hydrogenation to higher hydrocarbons as products is well known as the Fischer-Tropsch synthesis. Extensive research has been done in order to explore this reaction. Nowadays, it is commonly used as a model reaction to investigate the activity of novel catalytic surfaces.

Hydrogen and carbon monoxide adsorption and hydrogenation of CO on Rh(111) and V/Rh(111) subsurface alloys were studied in works [21,31,32]. It was found that the subsurface V slightly reduces hydrogen desorption energy and significantly reduces the desorption energy of molecular CO. The reaction rate of CO methanation on the alloy was enhanced at least by the factor 4 on the alloy surface as compared with pure Rh. Two possible explanations were proposed. First, lowering the CO desorption energy results, under identical reaction conditions, in a reduced surface coverage by CO molecules. Since the high surface concentration of CO inhibits the reaction, lower amount of adsorbed CO means higher activity. The second explanation concerns an increased number of catalytically active step and kink sites at the alloy surface as compared with the clean flat Rh surface.

The influence of vanadium on the CO hydrogenation on Rh was studied also on polycrystalline Rh [6,23]. The reactivity of the surface with V on top of the Rh and of the V–Rh subsurface alloy was compared with the bare Rh surface and with V_2O_3 islands on top of the polycrystalline Rh. The surface with the vanadium oxide was more reactive than bare Rh due to the enhanced activity on the oxide-metal interface. But the subsurface alloy exhibited even higher catalytic activity. The activity was measured at different CO and H_2 partial pressures as well as at different temperatures. Under the all experimental conditions, the activity of the subsurface alloy was 4–5 times higher (Fig. 1.2). For instance, while the conversion of CO at

623.5 K was 19% on bare Rh surface, it was increased to 88% on the alloy. Moreover, a change in the selectivity was observed. Selectivity toward alkanes and particularly alkenes was enhanced. It is worthy to note that the subsurface alloy remained stable without vanadium back-segregation to the surface, even under high pressure reaction conditions (40 mbar CO, 360 mbar H_2, He added to 1 bar). High initial activity exhibited also V islands on the Rh surface. However, this surface was deactivated rapidly by oxide and carbide formation.

Another catalytic reaction studied on Rh–V bimetallic systems was dehydrogenation of methanol [33,34]. The catalytic properties of the alloy were compared with clean Rh(111) and Rh(111) covered with V islands. On all the clean surfaces only CO and H_2 as reaction products were observed. The reaction pathway via O–H bond cleavage was not altered on the bimetallic surfaces as compared with pure Rh. However, it was observed that while on the clean Rh(111) surface methanol adsorption and dissociation ceases above 198 K, on the bimetallic surface adsorption and subsequent dissociation occurs up to 473 K. The dehydrogenation reaction of methanol on the alloy was faster than on the clean Rh surface. The reaction mechanisms and pathways were the same at both bare Rh and Rh/V alloy surfaces, but the activation energies of individual reaction steps were different, most probably due the electronic interaction between Rh and V atoms. The reactivity was the highest for V islands on Rh(111). But this surface was again deactivated fast due to CO dissociation.

In conclusion, Rh–V bimetallic system, especially in form of an alloy is an interesting material not only from the point of view of fundamental research but also from the point of its possible applications in several heterogeneous catalytic reactions in chemical industry and environmentally friendly technologies.

1.5 The Scope

The aim of the this study was to investigate the influence of the vanadium as a dopant on electronic and chemisorption properties of rhodium and the influence of an interaction with the gas molecules on the bimetallic system. Mixed Rh–V layers deposited on polycrystalline γ-Al_2O_3 were studied at first. This bimetallic model catalyst was designed as a step between well defined model catalysts and complex real catalysts. At such model catalyst, electronic, structural and morphological effects as well as an interaction with the substrate influence the overall chemisorption properties. The properties of the bimetallic supported system were compared to the properties of pure rhodium and vanadium supported layers prepared under the same conditions. In order to estimate the role of the electronic effects and eliminate the influence of the substrate and morphology, the study is further focused on three planar Rh–V systems. These systems were prepared by vanadium vapour deposition on polycrystalline flat Rh foil and rhodium single-crystals with surface orientations (111) and (110). The system with the polycrystalline rhodium was chosen as a step between the mixed Rh–V supported layers and the well-defined alloys of V and Rh on the rhodium single-crystal surfaces. Well-defined Rh(111) and Rh(110) surfaces were chosen since they enable studying surface atomic and electronic structure by means of surface physics techniques such as low energy electron diffraction (LEED), x-rays photoelectron diffraction (XPD) and angle-resolved ultraviolet spectroscopy (ARUPS).

The main method used to study the V–Rh bimetallic systems was photoemission spectroscopy. The standard laboratory x-rays photoelectron spectroscopy (XPS) was used to elucidate the electronic structure and chemical composition. Angle-resolved photoemission diffraction, LEED and STM methods were used to observe and analyse the atomic structure of the ordered V–Rh alloys. Photoemission spectroscopy induced by synchrotron radiation was used to study the top-most surface layers, the interaction with gas molecules and to map the electronic structure of metal valence bands. Chemisorption properties were also studied by means of TPD. The activity towards CO and O_2 gas molecules was investigated.

2 SURFACE ANALYSIS METHODS

A brief description of the surface sensitive methods used for the purposes of this work is given in this chapter. Among these methods, photoemission spectroscopy was used most extensively. Some aspects of photoemission spectroscopy techniques, which are not so common, are described in more details.

2.1 Photoelectron Spectroscopy (PES)

Photoelectron or photoemission spectroscopy is an experimental method which provides qualitative and quantitative information about chemical composition and electronic structure of the measured substances. PES is mostly utilized in the investigation of solid phase surfaces. Apart from the chemical composition PES also provide information about the surface atomic structure and morphology. All PES techniques are based on the photoelectric effect. In the photoelectric effect, electrons (called photoelectrons) are emitted from matter due to absorption of energy from electromagnetic radiation of the frequency sufficiently high to overcome the surface energy barrier. In a first approximation, the photoemission of an electron can be considered as a one particle excitation leaving the electronic structure of the atom unchanged. In the so-called three-step model, a PES experiment is separated into three independent processes. In the first step, a photon is absorbed and an electron is excited. In the second step, the excited electron travels through the sample to the surface. In the third step, the electron escapes through the surface energy barrier into the vacuum. In the vacuum, the photoelectrons are detected and their energy distribution is measured. The relation between the energy distribution of the detected photoelectrons and the energy levels in solid sample is schematically shown in Fig. 2.1.

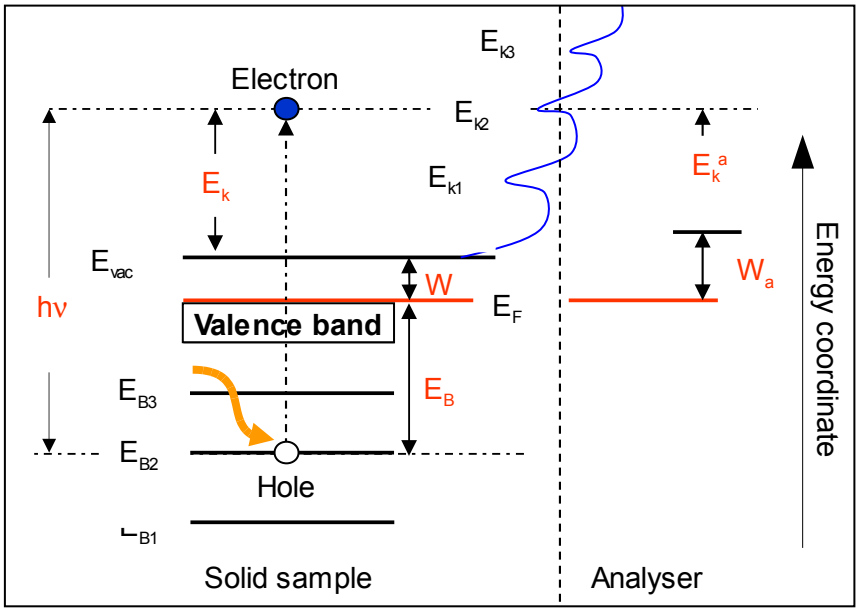

Fig. 2.1: Basic principle of photoemission spectroscopy. Relation between electron energy levels in a solid metal and the kinetic energy distribution of the detected photoemitted electrons. Binding energy E_B in solid metals is referred to the Fermi level E_F.

In the case of a metal sample, the Fermi level E_F is at the top of the valence band, separated from the vacuum level E_{vac} by work function W. If a photon with energy $h\nu$ is absorbed by a core level at binding energy E_B, the photoelectron has kinetic energy: $E_k = h\nu - E_B - W$ in the vacuum over the sample. When the electron energy analyser and the sample are grounded, their Fermi levels are at the same energy. The detected kinetic energy E_k^a is then determined by the analyser work function W_a:

$$E_k^a = h\nu - E_B - W_a \quad . \tag{2}$$

The detected energy distribution is unique to each element and it depends on the chemical state of the element. This is the first important feature of the PES method.

The second important feature of PES, with excitation energies not significantly higher than 1 keV, is the surface sensitivity. In order to detect a photoelectron from the core-level typical for an element, the photoelectron must reach the detector without overcoming any inelastic collision. The inelastic mean free path (IMFP) of photoelectrons with kinetic energy 50–1000 eV is equal to a few Å, which implies the sensitivity to only a few surface layers.

Nowadays, there exists large variety of PES techniques. Their detailed description can be found in several textbooks [18,35]. Here only those used in the present work will be mentioned.

2.2 X-ray Photoelectron Spectroscopy (XPS)

In XPS (also known as ESCA – Electron Spectroscopy for Chemical Analysis), samples are irradiated with soft x-rays. Mg Kα and Al Kα x-rays are usually used. Their energies and the line widths of the non-monochromatic radiation are summarised in Table 2.

Excitation radiation	Energy(eV)	FWHM(eV)
Mg $K\alpha_{1,2}$	1253.6	0.70
Al Kα	1486.6	0.85

Table 2: The most common x-ray radiation used in laboratory XPS [35].

Due to the photo-ionisation cross section, XPS is appropriate for obtaining spectra of core-levels. A typical energy resolution about 0.2 eV allows to identify not only the elements present in the sample but also their chemical state. The surface sensitivity of XPS spans from a few Å to several tens of Å in dependence of the kinetic energy of photoelectron, studied material and overall geometry. Table 3 illustrates the information depth of XPS on the example of some materials used in this work. The information depth can be as deep as 9 nm. On the other hand, in case of molecular adsorption or thin layer deposition, XPS is sensitive to amounts equivalent to fractions of ML.

Core-level/Material	E_{kin}(eV)[a]	IMFP (Å)[b]	$d_{37\%}$ [c](ML)[d]	$d_{95\%}$(Å)[e]	$d_{95\%}$ (ML)
Rh $3d_{5/2}$ / Rh	946	13	6	39	18
O 1s / Al_2O_3	722	20	10	60	30
Al 2p / Al_2O_3	1179	29	15	87	45

Table 3: Surface sensitivity of XPS.

[a] *Kinetic energy of photoelectrons excited by Mg Kα radiation.*

[b] *Inelastic Mean Free Path calculated with the use of TPP-2M formula [36].*

[c] *The depth from which come 37% of the signal in the case of pure flat Rh sample in normal emission geometry.*

[d] *The unit of depth (ML) corresponds to the (111) interlayer distance in Rh single-crystal and (100) interlayer distance in γ-Al_2O_3 single-crystal.*

[e] *The depth from which come 95% of the signal ($d_{95\%}=3d_{37\%}$).*

2.3 X-ray Photoelectron Diffraction (XPD)

XPD is a technique which exploits anisotropy in the intensity of the photoelectrons caused by the scattering of photoelectrons on atoms near the emitting atom, emitter. The scattering results in diffraction patterns (sometimes called holograms), which carry structural information about the surface. The most important characteristics of this technique are following. First, thanks to the photoemission process, the method is element and chemical state sensitive. That allows investigation of the positions of each of the constituent of the studied surface separately. Second, the structural information is local, i.e. diffraction patterns depend on atomic positions near the emitting atom. Third, the technique is surface sensitive in the typical kinetic energy range (100–1400 eV) of the photoelectrons. Therefore, it is often used to analyse crystal surface reconstructions, thin film growth, adsorbate positions and orientation or site determination of doped atoms.

In an XPD experiment, photoelectron angular distribution over a large solid angle is measured. One of the common detection methods is the combination of an angle-resolved energy analyser with a sample manipulator that can sweep emission angles θ and ϕ, as shown in Fig. 2.2(a). This method was used in this work and the obtained diffraction data are projected in the manner showed in Fig. 2.2(b).

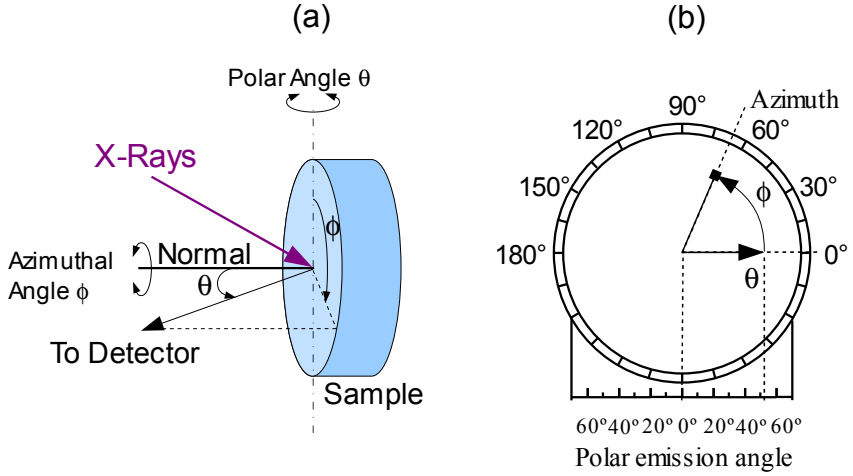

Fig. 2.2: (a) Geometry of the XPD experiment, showing the polar axes around which the samples were rotated. (b) Definition of the emission angles in the XPD diagrams.

The theoretical prediction of XPD patterns is well developed nowadays and it can be used in quantitative analysis of the surface structures by fitting theoretical

calculations to experiment. At high kinetic energies, direct structural information can be derived from a forward-scattering along the directions towards the nearest atom neighbours [37].

The simplest approach describing the photoelectron diffraction is single scattering cluster model schematically illustrated in Fig. 2.3. A photoelectron is emitted from a core level and it is propagating as a spherical wave. In single scattering approach, only one scattering event is considered on the way to the detector.

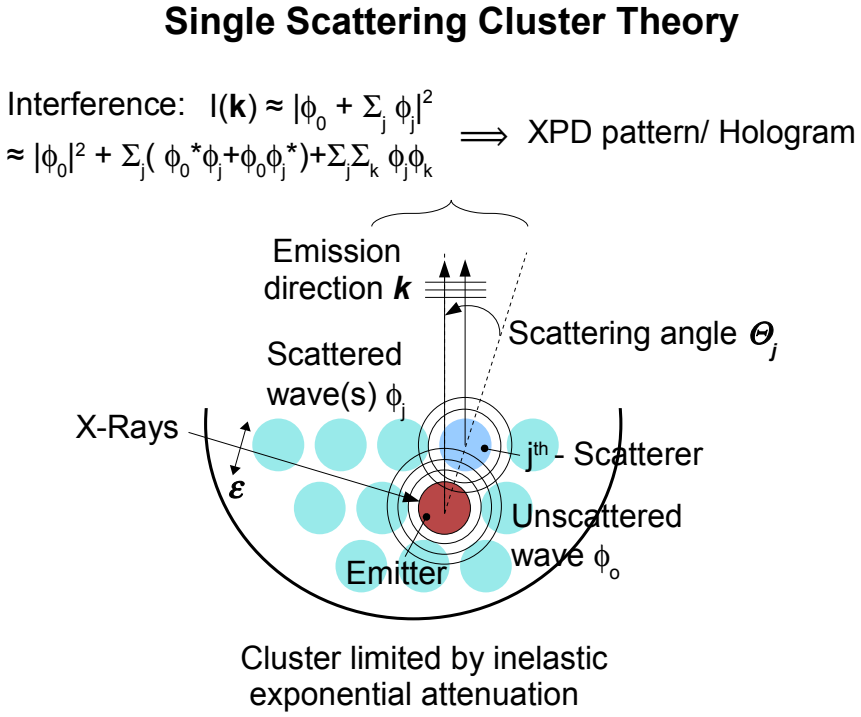

Fig. 2.3: The basic process involved in XPD. Only single scattering is indicated for simplicity. An electron is excited from emitter atom. A part of the excited electron wave ϕ_0 is scattered by surrounding atoms. The unscattered wave ϕ_0 and the scattered waves ϕ_j are interfered. The angular distribution of the electron forms the diffraction pattern.

The unscattered wave ϕ_0 interfere with various scattered-wave components ϕ_j. which results in the anisotropy of the photoelectron intensity:

$$I(\boldsymbol{k}) \approx |\phi_0 + \sum_j \phi_j|^2 \approx (\phi_0)^2 + \sum_j (\phi_0^* \phi_j + \phi_0 \phi_j^*) + \sum_j \sum_k \phi_j \phi_k^* , \qquad (3)$$

where $\boldsymbol{k}$ is the electron wave vector. If we consider photoemission only from an *s*-core level; linearly polarized X-rays; inelastic exponential intensity decay factor $\exp(-L/2\lambda_e)$; vibrational effects expressed by Debye-Waller factor W_j ; the Eq.(3)

can be rewritten as:

$$I(\boldsymbol{k}) \approx |(\boldsymbol{\epsilon}\cdot\boldsymbol{k}) \exp(-L_0/2\lambda_e) + \sum_j (\boldsymbol{\epsilon}\cdot\boldsymbol{r_j}/r_j)|f_j(\theta_j, r_j)|W_j \exp(-L_j/2\lambda_e)\exp(i[kr_j(1-\cos\theta_j)+\psi_j(\theta_j, r_j) \quad (4)$$

where $\boldsymbol{\varepsilon}$ represents polarisation direction; λ_e inelastic attenuation length; L is the total length of some path under the surface; $\boldsymbol{r_j}$ position vector of j atom in the considered cluster; $f_j(\theta_j, r_j)$ is scattering factor with an amplitude $|f_j(\theta_j, r_j)|$ and a phase shift $\psi_j(\theta_j, r_j)$ which are functions of the scattering angle θ_j and distance r_j to scatterer j. The structural information is contained in the last exponential factor, with the path difference between ϕ_0 and ϕ_j being given by $r_j(1\text{-}\cos\theta_j)$.

Equation (4) can be further generalized to include multiple scattering. More detailed theoretical approach to XPD can be found in [38-40].

The photoelectron diffraction patterns can be treated also as electron holograms. The unscattered photoemitted electron wave can be considered as well-defined reference wave and the ensemble of all waves scattered by surrounding atoms as the object wave [40,41]. In holographic analysis of XPD, real-space image (which is in fact the atomic environment of the photo-emitter) is calculated with the use of a reconstruction algorithm. However, most of the reconstruction algorithms are based on multi-energy format which requires energy-tuneable light source. On the other hand, a promising reconstruction algorithm for single-energy hologram has been proposed by T. Matsushita et al.[40] recently.

Apart from the cluster model approach to XPD there exits also dynamical Bloch wave approach to photoelectron diffraction [42,43], sometimes called as Kikuchi-band theory or electron channelling. In an XPD experiment, the outgoing photoelectrons are scattered by the crystal and detected as a plane wave at the detector. By using the reciprocity principle, the diffraction from a point source inside a crystal is equivalent to the problem of electron beam, incoming from the detection direction, that is diffracted by the crystal and results in a certain electron wave probability density at the emitting atoms positions. The higher the density at the atoms positions is, the higher photoelectron intensity is observed. A Bloch wave approach is used to calculate the electron probability density inside the crystal. This approach is suitable for the single crystal substrate emission at high kinetic energies at which surface reconstruction and relaxation is becoming insignificant [44].

Nowadays, the cluster model approach is widely used and several free program

packages are available to simulate experimental XPD patterns (for instance, EDAC [45] or TmCoCa software [46]).

One of the ways how to quantitatively determine geometrical parameters of the surface structure measured by XPD is the comparison of model simulations with an XPD diffraction experiment.

A degree of agreement between the experiment and theory in an electron diffraction experiment is usually quantified by reliability *R*-factors. Geometrical parameters of the chosen model are varied until minimum of the reliability factor is found. Several approaches has been used in *R*-factor analysis of XPD experiments [47-49]. Here we adopted method introduced by Saiki et al. [48]. In this method, prior to *R*-factor analysis, theoretical diffraction curves are normalized to have anisotropy as close as possible to that of experiment before a direct comparison. This normalization reduces influence of several non-ideal surface effects.

The normalization procedure is as follows. Since the anisotropy in XPD is larger for azimuthal scans at larger polar emission angles, data sets in each azimuthal scan are normalized separately. First, experimental diffraction curve I_{exp} in the azimuthal scan is rescaled to have values I^*_{exp} between zero and one:

$$I^*_{\mathrm{exp}}(n)=\frac{I_{\mathrm{exp}}(n)-I^{min}_{\mathrm{exp}}}{I^{max}_{\mathrm{exp}}-I^{min}_{\mathrm{exp}}}, \tag{5}$$

where n stands for the channel in the azimuthal scan; $I_{exp}{}^{max}$ ($I_{exp}{}^{min}$) stands for maximum (minimum) experimental value in the scan.

Next, the average value of the both rescaled experimental and original theoretical azimuthal curve I_{th} is set to zero:

$$I^{**}_{\mathrm{exp}}(n)=I^{*}_{\mathrm{exp}}(n)-\overline{I^{*}_{\mathrm{exp}}}, \tag{6}$$

$$I^{**}_{th}(n)=I_{th}(n)-\overline{I_{th}}, \tag{7}$$

where the mean values are equal to:

$$\overline{I^{*}_{\mathrm{exp}}}=\frac{1}{n}\sum_{n} I^{*}_{\mathrm{exp}}(n), \tag{8}$$

$$\overline{I_{th}}=\frac{1}{n}\sum_{n} I_{th}(n). \tag{9}$$

The rescaled theoretical azimuthal curve is then forced to have the same area as the rescaled experimental curve:

$$I_{th}^{\#} = I_{th}^{**}(n)\,(A_{\exp}^{**}/A_{th}^{**})\,, \tag{10}$$

where

$$A_{\exp}^{**} = \sum_n |I_{\exp}^{**}(n)|\,, \tag{11}$$

$$A_{th}^{**} = \sum_n |I_{th}^{**}(n)|\,. \tag{12}$$

From equations (5) and (6) implies:

$$I_{\exp}(n) = (I_{\exp}^{**}(n) + \overline{I_{\exp}^{*}})(I_{\exp}^{max} - I_{\exp}^{min}) + I_{\exp}^{min}\,. \tag{13}$$

Thus, the final normalized theoretical intensity I_{th}^{N} is given by:

$$I_{th}^{N}(n) = (I_{th}^{\#}(n) + \overline{I_{\exp}^{*}})(I_{\exp}^{max} - I_{\exp}^{min}) + I_{\exp}^{min}\,. \tag{14}$$

The difference between the calculated and normalized theoretical intensities is illustrated in Fig. 2.4.

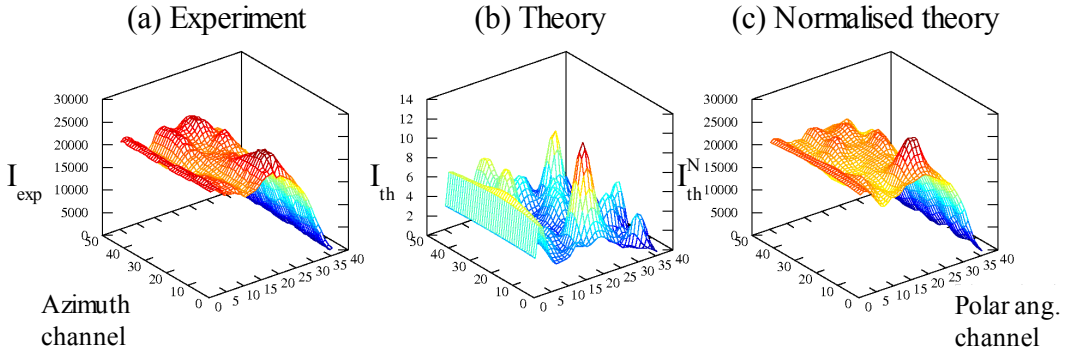

Fig. 2.4 (a) XPD intensities measured as a function of azimuthal and polar angle. (b) Calculated theoretical intensities. (c) Theoretical intensities normalized by the procedure described in the text.

A suitable *R*-factor for such normalized intensities is defined as [48]:

$$R_1(z) = \frac{\sum_n |I_{\exp}(n) - I_{th}^{N}(n,z)|}{\sum_n |I_{\exp}(n)|}\,, \tag{15}$$

where z represents structural parameter(s) used in the chosen theoretical model. The reliability factor R_1 is defined for one azimuthal scan. For a set of azimuthal diffraction data summed reliability factor R_s is defined as:

$$R_S(z) = \frac{1}{m}\sum_m R_1(m,z)\,, \tag{16}$$

where m is the number of azimuthal scans at different polar angles taken for the

measured surface structure. From the definition of the *R*-factor it is clear that the smaller the *R*-factor, the better the agreement between experiment and theory.

2.4 Synchrotron Radiation Photoelectron Spectroscopy (SRPES)

SRPES is a technique in which the photoemission is stimulated by synchrotron radiation. The main advantage of SRPES is the possibility to tune photon energy over a wide range. Another important advantage is high radiation intensity and, in combination with an appropriate monochromator, high energy resolution. The possibility to choose a photon energy allows tuning the information depth, since the IMFP of a photoelectron depends on its kinetic energy, which is determined by the energy of excitation radiation. In most materials, IMFP has minimum at kinetic energies between 50–100 eV. The information depth at such energies is equivalent to a few surface monolayers.

Another phenomenon commonly used in SRPES is the dependence of photoionisation cross section on photon energy ([50-52], Fig. 2.5). The cross section is different for different elements and energy levels, which can be used in suppression of the signal from one of signals in case of an overlap.

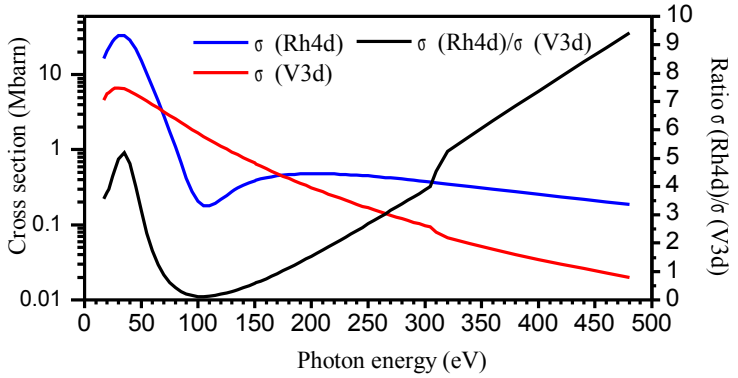

Fig. 2.5: Calculated atomic cross sections for photoionisation of Rh 4d and V 3d energy levels and their ratio. The data are taken from [50][51][52].

In the present work, SRPES technique was employed in the investigation of the surface and subsurface Rh–V alloys, in the mapping of their valence band electronic structure and in the investigation of core and molecular orbitals of adsorbed CO and O_2 molecules.

2.5 Angle Resolved Ultraviolet Photoemission Spectroscopy (ARUPS)

Photoemission with photon energies lower than 100 eV is known as Ultraviolet Photoelectron Spectroscopy (UPS). The valence band photoionisation cross-section for UV radiation can be several orders higher than for x-rays radiation (see, for instance, Fig. 2.5). This makes the UPS method appropriate for detailed valence band measurements. Typical range of the kinetic energies of photoemitted electrons provide sensitivity to a few surface layers and allow studying the valence band structure at surfaces. The valence band structure at surfaces is very sensitive to the processes on surfaces such as adsorption, chemisorption or chemical reactions.

In one-electron approximation, the energy states of electrons in metal single-crystals are characterized by single-electron energies E and wave vectors $\boldsymbol{k}$ (the wave vector of Bloch states in a crystal). Relation $E(\boldsymbol{k})$ is called band structure. In PES, transitions between states in occupied and empty bands are measured. These transitions are vertical in a reduced zone scheme and thus often called as direct transitions. In UPS regime, the spectra are determined by direct transitions. Angle-resolved UPS with high energy and momentum resolution analysers and with tuneable photon energy sources, such as synchrotron, can provide very direct $\boldsymbol{k}$-space images of valence band electronic structure of crystalline materials with considerable details.

The experimental geometry and the method of acquiring ARUPS data can be identical with the XPD method as described in Sec. 2.3 and illustrated in Fig. 2.2(a).

In contrast with XPD, in ARUPS the intensity of outgoing photoelectrons is measured not only as a function of emission angles θ and ϕ, but also as a function of their kinetic energy E_k (for simplicity, other parameters such as light polarisation or electron spin are not considered here). Applying energy and momentum conservation laws, the measured quantities can be transformed to the energy and momentum of the electrons inside the crystal, i.e., to the electronic structure $E(\boldsymbol{k})$.

In a rigorous analysis, an additional information about the final states must be given in order to get the band dispersion relations of the initial electronic states. It is also worthy to notice that in the case of ARUPS we are not dealing with ground state of the studied material.

Fortunately, several approximations which significantly simplify the extraction of

the dispersion relations from ARUPS data have been proofed to work excellently, especially at metal crystal surfaces.

According to the three-step model (Sec. 2.1), only photoelectrons with the energy sufficient to overcome the surface barrier can be detected. Once the work function W is known, the final E_f and initial state E_i energies are obtained from energy conservation law:

$$E_f = E_i + h\nu \,, \tag{17}$$

$$E_f = E_k + W \,. \tag{18}$$

In photoemission, the initial energy is commonly presented as the binding energy E_B with respect to the Fermi level:

$$|E_i| = E_B = h\nu - E_k - W \,. \tag{19}$$

In a typical ARUPS experiment, the momentum of the photons can be neglected. Photoelectron which is propagating to a detector must overcome the interface between the sample and vacuum. Thus, the electron wave is refracted and the surface-perpendicular component of its wave vector is not conserved. However, the transition of the electron through the surface leaves the surface-parallel component of the wave vector conserved:

$$\frac{\boldsymbol{p}_{\parallel}}{\hbar} = \boldsymbol{K}_{\parallel} = \boldsymbol{k}_{\parallel} + \boldsymbol{G}_{\parallel} \,, \tag{20}$$

where $\boldsymbol{p}_{\parallel}$ is the parallel component of the free electron momentum in vacuum; $\boldsymbol{K}_{\parallel}$ and $\boldsymbol{k}_{\parallel}$ are the parallel components of the electron wave vector outside and inside of the crystal, respectively; $\boldsymbol{G}_{\parallel}$ is the parallel component of a reciprocal lattice vector.

The component of the wave vector parallel to the surface $\boldsymbol{K}_{\parallel}$ is equal to:

$$\frac{\boldsymbol{p}_{\parallel}}{\hbar} = \boldsymbol{K}_{\parallel} = \begin{bmatrix} \cos\phi \\ \sin\phi \end{bmatrix} \sin\theta \sqrt{\left(\frac{2\mathrm{m}}{\hbar^2}\right) E_k} \quad , \tag{21}$$

where angles ϕ, θ defines the emission direction relative to the sample surface (see Fig. 2.2).

The surface-perpendicular component $K_{\perp}$ of the electron wave vector remains undetermined because there is no direct relation between crystal momentum $\hbar K_{\perp}$ and measured quantities $\boldsymbol{p}_{\parallel}$ and $p_{\perp}$. Additional knowledge is necessary in order to determine its value.

The transformation given by equations (19) and (21) does not give the true dispersion relation $E(\boldsymbol{k})$, but only $E(\boldsymbol{k}_{\parallel})$. On the other hand, the difference may

disappear when 2D surface structures, such as surface states, are measured.

The detected photoemission intensity I at certain kinetic energy E_k is proportional to:

$$I(E_k, h\nu) \propto \sum_{i,f} |M_{fi}(\boldsymbol{k_i}, \boldsymbol{k_f})|^2 \delta(E_f(\boldsymbol{k_f}) - E_i(\boldsymbol{k_i}) - h\nu) \delta(E_k - (E_f - \phi)) \quad (22)$$

where E_f and E_i are energies of the final and the initial state, respectively; $|M_{fi}(\boldsymbol{k_i}, \boldsymbol{k_f})|^2$ is the transition matrix element of the interaction operator and δ-functions express the energy conservation law.

In case of valence band photoemission from a polycrystalline sample in XPS regime, the momentum information is blurred and constant matrix element $|M_{fi}|^2$ and the density of final states can be assumed. The energy distribution below the Fermi level is then proportional the density of occupied states $DOS(E_i)$:

$$I(E_k, h\nu) \propto |M_{fi}|^2 DOS(E_i) \delta(E_k - E_f + \phi) . \quad (23)$$

The density of states is defined as:

$$DOS(E) = \frac{1}{(2\pi)^3} \int \frac{dS_E}{|\nabla_k E|} , \quad (24)$$

where dS_E is an element on the surface of constant energy and $\nabla_k E$ is the gradient of the energy.

For a particular photon energy $h\nu$, energy distribution of the joint density of states (*EDJDOS*) is defined as [18]:

$$EDJDOS(E_i, h\nu) = \frac{1}{(2\pi)^3} \sum_{i,f} \int \frac{dl_{fi}}{|\nabla_k E_f(\boldsymbol{k}) \times \nabla_k E_i(\boldsymbol{k})|} , \quad (25)$$

where dl_{fi} is an element of the line that is produced by the intersection of the surfaces E_i and $E_f = E_i + h\nu$.

It can be shown [18], that angle-integrated measurements over large solid angle result in energy distribution curve that is proportional to the *EDJDOS* in UPS regime.

Deeper understanding of the electronic structure obtained by ARUPS can be achieved by comparing experimental results with theoretical studies, if they are available. Theoretical studies based on DFT theory are of great importance because they can predict not only dispersion relations of the electronic surface states and the corresponding density of states but also provides charge density distributions of the surface states. DFT calculations allow to resolve the electronic structure of the surface on an atomic level. The charge distribution tells us about the character of the

bond, whether the electrons in surface states have bonding or anti-bonding character and their space distribution together with their binding energy are of immense importance in explaining and predicting interaction with adsorbed gas molecules and chemical reaction on surfaces.

2.6 Temperature Programmed Desorption (TPD)

In TPD, also known as Themal Desorption Spectroscopy (TDS), the sample surface is exposed to a gas or mixture of gases at first. Then, the temperature is ramped in a defined way, while the molecules desorbing from the surface are detected. The dependence of the amount of desorbed molecules on temperature or time is called thermal desorption spectrum. From one or series of thermal desorption spectra it is possible to determine kinetic parameters such as order of desorption, desorption energy or pre-exponential factor. Furthermore, TPD spectra carry information about the adsorption sites, surface coverage by the molecules, chemical reactions on surfaces, etc.

In UHV systems, the desorbing molecules are often detected in the form of partial pressures by a mass spectrometer. At sufficiently slow temperature ramp, large pumping speed S and absence of re-adsorption the desorption rate of a monitored gas is directly proportional to its partial pressure [53]:

$$r(t) = \frac{p_d}{\tau}\frac{VkT}{A}, \tag{26}$$

where p_d is the partial pressure after subtraction of the equilibrium value, V is the UHV chamber volume, A the area of the desorbing surface, k is the Boltzmann constant, T sample temperature and $\tau = V/S$. The number of desorbed molecules n can be obtained from a thermal desorption spectrum by integrating:

$$n_\infty = \int_0^\infty r(t)\,dt = \frac{S}{AkT}\int_0^\infty p_d\,dt\,. \tag{27}$$

In TPD, relative coverage is defined as:

$$\theta_{rel}(t) = \frac{n(t)}{n_\infty} = \frac{\int_t^\infty p_d\,dt}{\int_0^\infty p_d\,dt}\,. \tag{28}$$

The rate of desorption $r(t)$ from one site is well described by Polanyi-Wigner equation [53]:

$$r(t) = -\frac{dn}{dt} = n^h \nu_h(n) \exp\left(-\frac{E_D(n)}{kT}\right), \quad (29)$$

where n represents the number of adsorbed molecules, h is the order of the desorption, ν_h pre-exponential factor, E_D activation energy of the desorption.

Several techniques how to analyse TPD spectra have been developed [54]. In case of first order desorption, linear temperature ramp ($T=\beta t+T_0$) and if the dependence of the kinetic parameters on the surface coverage can be neglected, P.A. Redhead derived a formula to determine desorption energy from the position of peak maximum [55]:

$$E_D = RT_m\left[\ln\left(\frac{\nu}{\beta}T_m\right) - 3.46\right], \quad (30)$$

where T_m is the temperature at which TDS spectrum has its maximum, R is the gas constant. The Redhead formula gives desorption energy in kJ/mol units.

In the present work, TPD and analysis by means of the Redhead formula, with the pre-exponential factor 10^{13}, were used in the investigation of CO desorption from the Rh(111) and V–Rh(111) surfaces.

2.7 Low Energy Electron Diffraction (LEED)

Low energy electron diffraction is a common surface science technique used to study symmetries and atomic arrangement on crystal surfaces. In typical LEED set-up, solid crystal surface is irradiated by electrons with the kinetic energy range 20–500 eV. The de Broglie wavelength of such electrons is lower than typical inter-atomic distances and the attenuation length at a solid surface is near its minimum. That makes the technique surface sensitive. The electrons, elastically backscattered from the surface, form a Fraunhofer diffraction pattern. The LEED pattern is an image of the surface reciprocal mesh. Patterns with sharp spots imply the existence of well-ordered surfaces and provide direct information about the symmetry of the surface. The true surface structure can be of lower symmetry, however. The distance between points in a reciprocal lattice is inversely proportional to the distance between points in true lattice. The larger the periodicity of the surface structure the smaller distances between diffraction spots in the LEED pattern. The true atom arrangement on the surface can not be determined from one LEED pattern. The atomic surface structure can be determined only from the energy dependence of LEED beam intensities, from the so-called *I(V)* curves.

The LEED technique was used in this work to study at the Rh(111) and Rh(110) surfaces, to monitor the quality of the surfaces and surface reconstructions stimulated by the alloying with vanadium.

2.8 Scanning Tunnelling Microscopy (STM)

STM is a surface sensitive technique which, under certain circumstances, enables to see surface topography with atomic resolution. The method is based on the effect of quantum mechanical tunnelling through an energetic barrier. In STM, an atomically sharp metal tip approaches a surface to a distance of a few Ångströms. The space between the tip and surface represents the width of the barrier in vacuum. The height of the barrier is given by the tip and surface work functions. At sufficiently low distances, the equilibrium of the Fermi level between the surface and tip is established due to the tunnelling effect. If a voltage U is applied on tip or sample, electrons from occupied states are tunnelling into unoccupied states of the other surface. The tunnelling current is exponentially decreasing with increasing distance between the tip and surface. Usually the tip scans the surface in a constant current mode, when the tunnelling current is kept constant through a feedback loop by moving the tip position over the surface. In Tersoff and Hamann approximation [56], the tunnelling current is also proportional to the local density of states at the Fermi level of the sample. Thus, the tip follows not only the surface topography during the scanning but also places with a constant density of states on the surface.

3 EXPERIMENTAL SYSTEMS

In this chapter, experimental systems, at which the experiments were carried out, are described briefly and only those parts that were relevant from the point of view of the performed experiemts. Detailed description of procedures for the cleaning and preparation of the samples and other experimental details will be given in the correspondent parts of Chapter 4 .

3.1 XPS/TPD experimental system

The first experimental system XPS/TPD was situated at the Department of Surface and Plasma Science (DSPS) in Prague. The UHV system combined XPS and TPD techniques, which allowed to study surface reactivity and chemical composition *in situ*. The system was employed in the investigation of the properties of thin Rh–V layers supported by γ-Al_2O_3 and V–Rh bimetallic systems prepared by V deposition onto polycrystalline Rh.

The base pressure of the XPS/TPD system was lower than 2×10^{-8} Pa. For the purposes of XPS, the system was equipped with a double anode non-monochromatic x-rays source of Al Kα and Mg Kα radiation and an Omicron EA125 hemispherical analyser with five-channel detector. As far as TPD is concerned, the apparatus was equipped with a Leybold Inficon quadrupole mass spectrometer placed in a differentially pumped chamber. This chamber was connected with the main one by a 3 mm orifice. The samples were being held in front of it at a distance about 3 mm. Samples, of a typical size of 10×10×0.5 mm, were placed on a copper holder which could be heated up to 1000 K. Temperature was monitored by a chromel-alumel thermocouple fixed near the front side of the holder. The feedback loop enabled linear heating in the range of 300–773 K with the rate of 1.2 K/s. The gases were introduced into the chamber through thin stainless tubes terminated with a double diaphragm. The gas flow was regulated by sapphire valves.

The XPS/TPD system was further equipped with Ar^+ ion gun for sample cleaning. The ion gun was able to accelerate the Ar ions up to the energy of 3 keV. At the energy of 1 keV, the ion-current density on the sample surface was about 1 $\mu A/cm^2$.

For metal deposition, two microelectron bombardment evaporation sources (MEBES) [57] were installed. The evaporation rate was measured by a quartz crystal

film thickness monitor. A more detailed description of the apparatus is given in [58].

3.2 XPS/XPD/LEED experimental system

The second UHV experimental system XPS/XPD/LEED, situated at the DSPS in Prague was employed to investigate atomic structure of the V–Rh(111)–(2×2) subsurface alloy by means of XPD. The system, with base pressure 2×10^{-8} Pa, was equipped with a hemispherical electron energy analyser Specs Phoibos 150, an Al X-ray source; an Ar^+ ion gun; a movable manipulator controlled by stepping motors; and LEED optics. The angle-resolved XPS spectra were recorded by rotating the sample manipulator around two axes. The angle between the x-rays incidence and analyser axis was 68°. The sample holder could by heated up to 1200 K. For V deposition, the MEBES evaporation source from the XPS/TDS system was installed. More details about the system as well as about the data acquisition and processing for the purposes of XPD are given in [59].

3.3 STM experimental system

STM measurements on Rh(110) substrate were performed at the DSPS in an UHV system which was equipped with a home-built STM microscope, LEED optics and a preparation chamber with facilities for *in-situ* sample cleaning and preparation. The base pressure was better than 2×10^{-8} Pa. The preparation chamber contained Ar^+ ion gun, which could produce ion current with the density of about 1 $\mu A/cm^2$ at the sample position and a Tectra electron beam evaporator for V deposition from wire. The sample could be heated by heat conduction up to 1200 K from a small oven on which it was placed. The thermocouple fixed near the sample back-side. Over the sample holder, a quartz crystal microbalance for film thickness monitoring was placed. More detailed description of the system can be found in [60].

3.4 XPS/LEED/TPD experimental sytem

TPD measurements on Rh(111) and V–Rh(111)–(2×2) were performed at XPS/LEED/TPD apparatus at the Department of Chemical Engineering, University Patras, Greece. For sample treatment and preparation, the system was equipped with a Ribere/Cameca argon ion gun and a manipulator with sample stage allowing programmed sample heating and cooling in temperature range 150–1120 K. For V deposition, the MEBES evaporation source was installed. For the implementation of

XPS, a Leybold EA-11 hemispherical electron energy analyser in combination with a Specs/XR-30 dual anode, non-monochromatic X-ray source (Mg Kα and Al Kα) were used. For TPD, a Balzers quadrupole mass spectrometer was mounted in a differentially-pumped, internally fitted cell, which ended up in a 1.5mm diameter nozzle facing the sample to which the the whole assembly could be brought to a desired distance. The system was further equipped with a reverse view LEED facility.

3.5 Materials Science Beamline (MSB)

The MSB is an experimental facility situated at Elettra synchrotron in Trieste, Italy. The system was used to perform high-resolution core-level photoemission spectroscopy and valence band mapping by means of ARUPS at V–Rh(111) and V–Rh(110) bimetallic systems.

The beamline uses radiation from a bending magnet at the Elettra storage ring. The bending magnet radiation is mostly linearly polarised in the horizontal direction. A plane grating monochromator, based on SX-700 design concept [61], allowed to tune the photon energy in a range of 22-1000 eV with the resolving power typically higher than 1000. The resolving power is naturally better at lower photon energies in the case of the used monochromator. During the experiments presented in this work an UHV chamber optimised for several PES techniques was situated at the end of the beamline. In front of the UHV chamber, a golden mesh, through which the monochromatic radiation entered into the chamber, was placed. The photoemission current measured on the mesh was used to normalise the recorded photoemission spectra to the intensity of the incident photon flux. Apart from SRPES, XPS excited by a dual anode x-rays source (Al Kα and Mg Kα) was available at the beamline station. For the detection of photoelectrons, a Specs Phoibos 150 hemispherical electron energy analyser was utilized. Its axis was inclined 60° from the beamline axis. The samples were mounted on a holder allowing rotation of samples around two axis. Furthermore, the sample holder allowed heating and cooling of the samples. The Rh crystals used in the present work were heated by heat conduction from tantalum wires between which they were mounted. Temperature of the single-crystals was measured by a thermocouple attached to the back side of the crystals. In addition, the chamber was equipped with a rear view LEED optics; MEBES

evaporators for metal deposition; Ar^+ sputtering gun and gas-inlet lines with precision leak valves. Some more details about the beamline and end station can be found elsewhere [62].

4 RESULTS AND DISCUSSION

Results presented in Sections 4.1 , 4.2 and some results in Sec. 4.3 are based on the following original publications:

1. Pis, I, Nehasil, V, Ladas, S and Symianakis, E. Adsorption of CO on V-Rh(111)(2×2) surface. In *WDS'08 Proceedings of Contributed Papers: Part III - Physics* (eds. J. Safrankova and J. Pavlu). Prague: Matfyzpress, 2008, 634-637. ISBN 978-80-7378-025-8.
2. Píš, I, Matolín, V and Nehasil, V. XPS and TPD investigation of CO adsorption on mixed Rh–V layers supported by gamma-alumina. *Applied Surface Science*. 2011, **258**, 908-913.
3. Píš, I, Skála, T, Cabala, M, Šutara, F, Libra, J, Škoda, M, Matolín V and Nehasil, V. Structural, electronic and adsorption properties of V–Rh(111) subsurface alloy. *Journal of Alloys and Compounds*. 2012, **543**, 189-196.

4.1 Rh–V layers supported by γ-Al_2O_3

4.1.1 Introduction

Real heterogeneous catalysts with precious metals have typically shapes of nano-particles, which are deposited on high surface ceramic supports. Vapour deposited thin mixed metal films on a flat oxide substrate can be considered as a step between will defined model catalysts and complex real catalysts. The goal of the experiments with Rh–V layers supported by γ-Al_2O_3 was to investigate the influence of vanadium on CO adsorption and desorption properties of the supported Rh thin film and an influence of CO molecules on the bimetallic system.

Electronic and chemisorption properties of the mixed Rh–V layers deposited on polycrystalline γ-Al_2O_3 were investigated by means of XPS and TPD spectroscopy of CO molecules. The CO desorption from the mixed film was compared with the CO desorption from pure Rh layer prepared under the same conditions as the mixed films. In addition, the growth and electronic properties of pure vanadium layer on γ-Al_2O_3 was measured by means of XPS, so that the role of an interaction between the support and vanadium atoms could be estimated. The overall thickness was chosen to be sub-monolayer in order to assure the preparation of non-continuous thin layers. The evaporated amount of Rh and V was 0.6 and 0.2 ML, respectively. The chosen

ratio between the evaporated metals was based on the diploma thesis [63] of the author. It was observed, that if the atomic concentration ratio between Rh and V in the non-continuous supported thin films is equal or lower than one, then vanadium carbides and oxides are formed rapidly and the overall bimetallic system is deactivated towards the interaction with CO molecules. In order to observe the bimetallic interaction, two samples, equal in the composition, were prepared. The difference was in the order of the metal deposition.

4.1.2 Experimental

The experiment was performed at the XPS/TPD facility at the Department of Surface and Plasma Science in Prague. Samples were prepared by vapour deposition of Rh and V metals onto the polycrystalline γ–Al_2O_3 surface at room temperature. The metals were evaporated from two MEBES sources. The purity of the metals was 99.9% and 99.8%, respectively. The evaporation rate for both metals, estimated by a quartz crystal film thickness monitor, was 0.2 ML/min (1 ML is meant as an equivalent to the number of Rh atoms in one monolayer of Rh(111), i.e. 1.597×10^{19} at./m^2).

The polycrystalline γ–Al_2O_3 substrates were prepared from GFM 99.999 % Al cut into a plate 10×10 mm^2, 0.5 mm thick. The Al plates were mechanically and chemically polished and oxidized in air at a temperature of 873 K for 24 hours. This procedure forms 50–100 nm thick polycrystalline γ–Al_2O_3 film with an average micro-crystal size of 0.1 μm and lattice constant 0.79 nm [64]. After the introduction into the UHV chamber, the alumina substrates were cleaned by heating at 800 K for 5 minutes and Ar^+ sputtering at room temperature for a few minutes.

Two samples with mixed Rh–V thin layer were prepared by vacuum vapour deposition at room temperature of the substrate. The evaporated amount of Rh and V was 0.6 ML and 0.2 ML, respectively. After the deposition of the both metals, annealing at a temperature of 795 K for 5 minutes followed. After that, the experiments with CO adsorption and desorption were performed. The pure Rh layer on γ-Al_2O_3 was prepared in the same way as the mixed layers. The evaporated amount of Rh was again 0.6 ML.

To study the growth of pure vanadium on γ–Al_2O_3, gradual deposition of 0.1, 0.3, 0.6, 1.0, 1.5, 3.0, and 6.0 ML of V on a clean γ-Al_2O_3 substrate was performed. The

growth and chemical state was monitored by XPS.

XPS measurements were performed with Mg K_α line. To compensate charging effects during the XPS measurements, photoelectron binding energies were referred to Al $2p_{3/2}$ peak, which BE was set to be at 75 eV. Al $2p_{3/2}$, O 1s, C 1s, Rh 3d and V 2p core level peaks were measured.

Exposures to CO gas in TPD experiments were performed by a CO molecular beam directed to the samples at partial pressure of 1.2×10^{-6} Pa and at room temperature.

4.1.3 Growth of V on polycrystalline γ-Al_2O_3

There have been several studies devoted to the growth of V on alumina surfaces [65-67]. In order to compare the behaviour of vanadium on the gamma-alumina used in this work with previous studies, the growth of vanadium on the γ–Al_2O_3 substrates without Rh was measured.

The vanadium was evaporated gradually on a clean γ–Al_2O_3 support at room temperature as described above.

Many experiments with V on alumina films showed strong V substrate interaction. There have been studies investigating the interaction of vanadium atoms with α–Al_2O_3 (0001) surface [66] and with thin (5Å) film of alumina grown on NiAl(110) [65]. STM images of V metal deposits on Al_2O_3/NiAl(110) at room temperature showed the growth of V layer in Vollmer-Weber (3D islands) mode and the XPS measurements indicated the V grows in simultaneous multilayer mode on α–Al_2O_3 (0001). The V clusters/particles were thermally stable up to 800 K due to a considerable interaction with the alumina substrate. Similar temperature stability of V clusters was also observed by Wiltner *et al*. [68] on vanadium film grown on Al_2O_3/NiAl(111). The growth and chemical state of V deposited on the polycrystalline γ–Al_2O_3 in this work was investigated by means of XPS, measuring the spectra of V 2p, O 1s, and Al $2p_{3/2}$ core levels. The evolution of V 2p and O 1s spectra with increasing evaporated amount of vanadium are shown in Fig. 4.1.

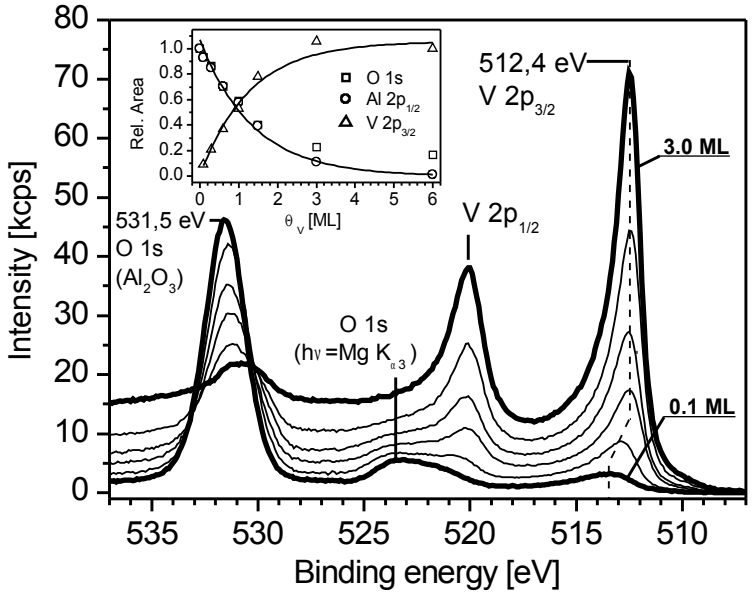

Fig. 4.1: V 2p and O 1s spectra from vanadium grown on γ–Al_2O_3. The correspondent amount of deposited vanadium was (from bottom to top): 0.1, 0.3, 0.6, 1.0, 1.5, and 3.0 ML. The inset shows the intensities of the photoemission peaks as a function of the deposited amount of vanadium. The intensities are related to the maximum values in the sequence.

The inset in Fig. 4.1 displays the dependence of photoelectron intensities on the evaporated amount of vanadium. The Al $2p_{3/2}$ signal was decreasing with the deposited amount of V until it was near to the detection limit. Simultaneously, the V 2p signal was increasing until the saturation of the signal was observed. The dependence of the intensities on the deposited amount of V can be approximated by exponentials rather well. That indicates a 3D islands growth mode, which is in accordance with the vanadium growth mode on α–Al_2O_3 [66] and on Al_2O_3/NiAl(110) [65]. The different decrease of the intensity of O 1s and Al 2p peaks was caused by the adsorption of oxygen on V from the ambient atmosphere. With increasing amount of deposited V, a new state at the energy of 530 eV in O 1s spectrum appeared. This state was attributed to the vanadium oxides [69]. Owing to the high reactivity of vanadium toward oxygen molecules and the rather low deposition rate of vanadium, an oxygen contamination is to be expected [70], even though the pressure during the vanadium evaporation was below 2×10^{-9} mbar.

The increasing V 2p intensity in Fig. 4.1 is accompanied with a simultaneous shift of the peak toward lower binding energies. The energy 512.4 eV at high coverages

corresponds to metallic overlayer of vanadium [69]. The reason of the higher binding energies at lower coverages can be two-fold. The previous studies showed that vanadium grows on alumina surfaces in form of small isolated particles in the initial stage of deposition under the conditions similar to this experiment. Our XPS measurements indicate the same growth mode. In such case, final state effects must be considered. They are interpreted as Coulomb energy shifts due to particle size effects. The second reason of the energy shift to higher values can be a formation of vanadium oxides and suboxides at low coverages as it was observed on the other alumina surfaces. A submonolayer coverage of vanadium on 5 Å thick alumina grown on NiAl(111) [65] was accompanied with formation of V^{x+} cations with $1<x<2$ and NEXAFS measurements [66] showed formation of V_2O_3 on α-Al_2O_3 at submonolayer coverage regime.

4.1.4 Thin Rh layer supported by polycrystalline γ-Al_2O_3

As a reference to the mixed Rh–V layers, a pure rhodium thin film was studied at first. The submonolayer amount of Rh (0.6 ML) was evaporated onto the γ-alumina surface at room temperature. The sample was heated at 795 K for 5 minutes subsequently. Such sample treatment leads to a creation of Rh particles by coalescence [11,12]. After the sample preparation, 3 cycles of CO adsorption and TPD were performed. The samples were exposed to a 3L dose of CO at room temperature in each cycle, which corresponded to a saturation exposure. The corresponding TPD peaks are displayed in Fig. 4.2(a). The differences between the TPD spectra of each cycle are a result of a stabilization of the Rh layer by annealing and exposure to CO. Two pronounced CO desorption peaks at 480 and 400 K were detected. The TPD spectra are also in good agreement with previous studies of CO desorption from Rh particles [13,71,72]. The previous studies showed how the relative ratio between the low and high temperature peak depends on the size of Rh particles. The relative proportion of CO in each desorption state was only weakly dependent on particle size larger than 3nm, while particles with the average size lower then 3 nm exhibited higher relative intensity of the desorption peak at the lower temperature. Thus, it can be assumed that the average size of the Rh particles prepared here was higher than 3 nm. The change in the TPD profiles with number of the TPD cycle indicates further changes in the size or structure of the Rh supported

particles. The decrease of the desorption energy of CO, i.e. shift of the desorption maximum to lower temperature, can be assigned to thermally induced ordering of the particles and reduction of the defects on them. A small desorption peak was detected at temperatures around 690 K. It corresponds to the recombination of adsorbed C and O atoms into CO molecules.

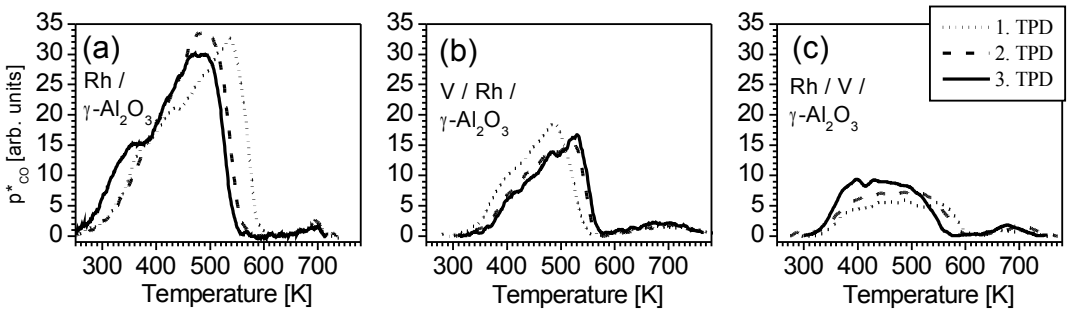

Fig. 4.2:Temperature-programmed CO desorption spectra from (a) Rh layer, (b) mixed V-Rh layer, where Rh was deposited at first, and (c) mixed Rh-V layer, where V was deposited at first. At each sample, three subsequent TPD measurements were performed after dosing 3L CO. The dotted, dashed, and solid line correspond to the first, second, and third cycle, respectively.

4.1.5 Mixed thin Rh-V layers supported by polycrystalline γ-Al_2O_3

Two samples of the same metal composition but with different order of the metal deposition were prepared. In one case, the rhodium was evaporated at first and vanadium afterwards (sample marked as V/Rh/γ–Al_2O_3). In the second case, the order of the deposition was reversed (Rh/V/γ–Al_2O_3). The evaporated amount of Rh and V was the same in both cases (0.2 ML of V and 0.6 ML of Rh). After the XPS characterization of the room temperature deposits, the samples were annealed at a temperature of 795 K for 5 minutes, in the same way as it had been done with the reference Rh thin film. Then TPD measurements followed.

The samples were annealed prior to TPD measurements because of two reasons. First, the temperature was raised up to 795 K during the TPD, which is in case of the Rh on alumina surface connected with structural changes of possible Rh clusters. Second, according to the previous research on Rh–V systems [21,34] the annealing should stimulate the formation of a V–Rh alloy which is more stable against the deactivation caused by the formation of vanadium oxides and carbides.

Both samples were exposed to 3L of CO at room temperature before each TPD.

The CO adsorption-desorption cycle was repeated three times. TPD spectra of CO desorption are plotted in Fig. 4.2. Interestingly, the two bimetallic samples, with the same composition but different way of preparation, showed very different TPD spectra. While the bimetallic sample V/Rh/γ–Al_2O_3 (Fig. 4.2(b)) showed TPD profile similar in shape to the profile from Rh/γ–Al_2O_3 sample (Fig. 4.2(a)), the sample Rh/V/γ–Al_2O_3 revealed a pronounced relative increase of the low-temperature desorption states. The differences can be a consequence of the electronic changes induced by alloying or/and in the different morphology of the bimetallic layers. On the other hand, the TPD spectrum of the former sample (Fig. 4.2(b)) which is slightly shifted to higher temperatures in comparison to Rh/γ–Al_2O_3, indicates that the morphology effect could prevail in this case. The lower amount of the CO molecules desorbed from the mixed layers could be also related to the different morphology. However, a partial deactivation of the bimetallic systems (as indicates XPS shown further) can explain the decreased desorption peak intensity, too. The differences between the first and the subsequent TPD spectra are the evidence of a stabilization of the deposited layers, most probably due to the increased temperature during the TPD measurement. CO adsorption stimulated changes, however, can not be excluded, as well.

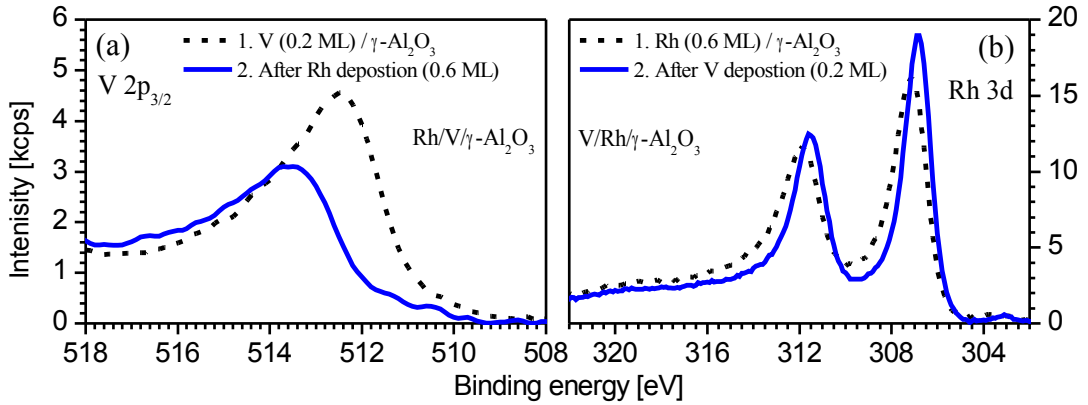

Fig. 4.3: XPS spectra of V and Rh from mixed Rh-V layers on γ-Al_2O_3. (a): V $2p_{3/2}$ spectra from the sample, where 0.2 ML of V was evaporated at first and 0.6 ML of Rh afterwards. (b): Rh 3d spectra from the sample where 0.6 ML of Rh was evaporated at first and 0.2 ML of V after.

The photoemission spectra revealed a pronounced electronic interaction between the deposited metals. The influence of the deposition of one metal on the

photoemission spectrum of the second metal is demonstrated in Fig. 4.3. Fig. 4.3(a) displays V $2p_{3/2}$ spectrum of the Rh/V/γ–Al_2O_3 sample before and after the deposition of Rh and Fig. 4.3(b) displays Rh 3d spectrum of the V/Rh/γ–Al_2O_3 sample before and after the deposition of V. The Rh 3d spectrum is shifted about -0.3 eV by the interaction with V and V $2p_{3/2}$ spectrum is shifted about +1 eV by the interaction with Rh. The lower intensity of the V $2p_{3/2}$ peak after the deposition of Rh is the result of the attenuation of the V $2p_{3/2}$ signal by the Rh layer. The Rh 3d peak area in Fig. 4.3(b) decreased only slightly after the vanadium deposition. Although the amplitude of the Rh peak increased, the peak became narrower and the overall area of the peak is lower. The rather small decrease of the Rh 3d area indicates that some of the vanadium was not deposited directly on the rhodium layer but also on alumina substrate between the Rh clusters. The decrease of the Rh 3d peak width and the energy shifts in XPS spectra of both elements are indications of an alloying with a charge transfer from the vanadium to the rhodium.

The photoemission spectra of the mixed Rh-V layers after the metal deposition and after the post-annealing are compared in Fig. 4.4. By comparing the V $2p_{3/2}$ spectrum of the Rh/V/γ–Al_2O_3 sample in Fig. 4.3(a) and Fig. 4.4(a) one can see that the annealing resulted in additional energy shift of the vanadium peak to higher binding energies from 513.6 eV to 514.0 eV. That might be the consequence of temperature stimulated mixing and further alloying of the Rh–V layer. Due to the possible Rh coalescence at the used temperature range [11,12], it is likely that the mixed thin films formed bimetallic particles. This assumption is supported also by a decrease of both Rh 3d and V $2p_{3/2}$ peak areas after the annealing, which is typical for temperature stimulated coalescence. The decrease can be seen when comparing the spectra of V/Rh//γ–Al_2O_3 in Fig. 4.3 with those in Fig. 4.4. V $2p_{3/2}$ spectra from both samples, just after the V deposition, were almost identical. Rather different V $2p_{3/2}$ intensities between the bimetallic layers (Fig. 4.4(a)) imply a different depth distribution of V atoms, which might be also connected with the different morphology of the two Rh-V layers. Nevertheless, the different photoemission spectra of the bimetallic samples after the metal deposition and annealing can be correlated with the different CO adsorption properties.

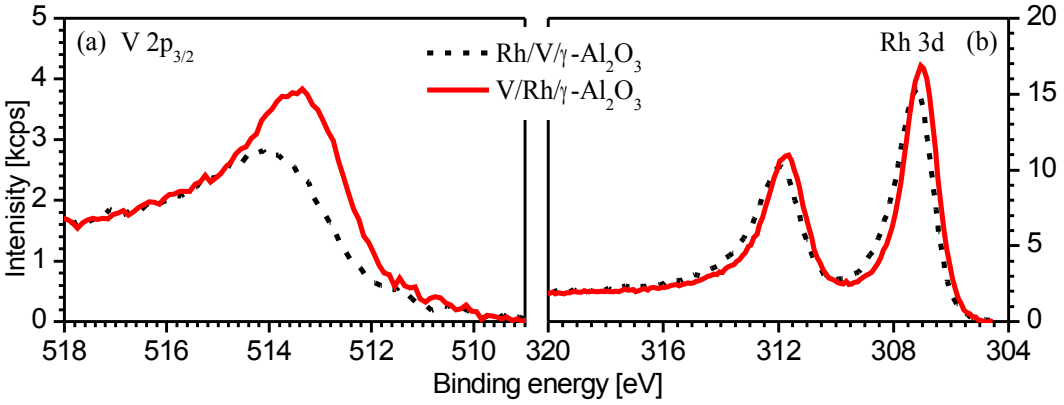

Fig. 4.4:A comparison of V $2p_{3/2}$ (a) and Rh 3d (b) XPS spectra from the two mixed Rh-V layers, which differed in the order of the metal deposition. The spectra were taken after the annealing at the temperature of 795 K for 5 minutes.

The lower amount of desorbed CO molecules from the bimetallic layers can be understood by V $2p_{3/2}$ XPS spectra taken before and after the TPD measurements. Both samples exhibited very similar changes in the spectra, thus Fig. 4.5 displays spectra only from one of the two samples. The peak is broadened at binding energies higher than 515 eV, which is an indication of the presence of vanadium oxides (515.7 eV for V_2O_5, 517.4 eV for V_2O_3 [73]). Further annealing of the samples at elevated temperatures led to a reduction of the high-energy states. The vanadium oxides had to be formed soon after the first exposure to CO by reaction of adsorbed CO with vanadium atoms that remained on the surface. The formation of the surface vanadium oxides deactivated the surface as far as CO adsorption at room temperature is concerned.

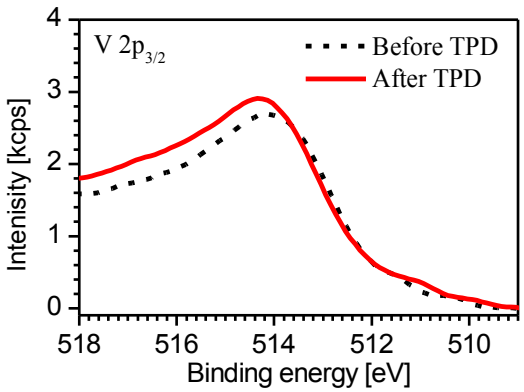

Fig. 4.5: V $2p_{3/2}$ spectrum of the V/Rh/γ-Al_2O_3 sample taken before and after the experiments with CO adsorption and temperature-programmed desorption.

Another notable feature in the TPD from the mixed films (Fig. 4.2) is the presence of relatively intensive β-peak (about 2-times more intensive in comparison with pure Rh layer). The increased extent of the CO dissociation can be a consequence of the electronic interaction between the two metals, but it could be also a consequence of a different morphology of possible bimetallic particles. It is known, that in case of supported pure Rh clusters, the amount of dissociated CO molecules depends on the cluster size [74]. Nevertheless, the presence and relatively high extent of CO dissociation on the mixed Rh–V layers might play an important role in catalytic reactions on a real catalyst.

4.1.6 Conclusions

Gamma-alumina supported mixed bimetallic Rh–V thin films, with the overall thickness of 0.8 ML, were prepared under ultra-high vacuum conditions. Their electronic and chemisorption properties were compared with pure Rh and V thin films.

XPS measurements showed that the vanadium deposited on the polycrystalline γ-Al_2O_3 substrate grows in 3D islands growth mode. There are indications of a notable interaction between the substrate and vanadium at the interface.

The pure Rh thin film without vanadium exhibited behaviour typical for supported Rh nano-particles. If vanadium is added, an alloy is forming and the CO desorption properties of the thin metal layer are different in comparison with pure Rh layer. The influence of the vanadium strongly depends on its distribution within the bimetallic layer. Relative increase of desorption from weaker bounded CO molecules on the bimetallic film and pronounced increase of CO dissociation was observed. The altered chemisorption properties could be the result of electronic as well as morphological effects.

4.2 V on polycrystalline Rh foil

4.2.1 Introduction

The study of V–Rh bimetallic system prepared by V vapour deposition on the clean polycrystalline Rh surface was chosen as a step between the quite complex V–Rh non-continuous layers supported on γ–Al_2O_3 and well defined V–Rh(111) and V–Rh(110) systems. The main purpose of this experiment with polycrystalline Rh

substrate was to probe the electronic influence of the vanadium on the chemisorption properties of rhodium and find experimental conditions appropriate for alloying. Electronic structure of the bimetallic system was studied by means of XPS, CO chemisorption properties by TPD spectroscopy.

4.2.2 Experimental

The experiment was performed at the XPS/TPD experimental system. The vanadium was deposited onto the surface of a high purity Rh foil (99,99 %) by evaporation from V wire (purity 99.8%) placed in MEBES. The surface of the Rh foil was cleaned by 0.5 keV Ar^+-ion sputtering followed by annealing up to 975 K. Two samples were prepared. In both cases, 1 ML of V was evaporated with the evaporation rate of 0.2 ML/min. The samples differed in the substrate temperature during the deposition. The temperature of the Rh foil was held to be 295 K and 795 K, respectively. After the vanadium evaporation, the sample prepared at a temperature of 795 K was held at the elevated temperature for another 5 minutes and the sample prepared at 295 K was post-annealed to 795 K for 5 minutes. The samples were characterized by means of XPS employing Al K_α X-rays source. The exposure to CO was done at the partial pressure of 1.2×10^{-6} Pa at room temperature.

4.2.3 XPS characterization

The V 2p XPS spectra recorded after the V deposition and annealing are displayed in Fig. 4.6. Although the deposited amount of V was the same in both cases, the intensity of V 2p peak is lower in the case of deposition at a temperature of 795 K. It is because of diffusion of V atoms to the subsurface region of Rh and formation of a stable subsurface alloy at elevated temperatures, as was reported in [6,23]. CO chemisorption behaviour also confirmed the difference in the V presence on the surfaces of the two samples, as it will be shown further. The spectra in Fig. 4.6 were fitted by Doniach-Sunjic functions [35,75] convoluted with Gauss function and the fitting parameters except the peak amplitude were kept at the same values for both samples. The binding energy of 513.3 eV of the main V $2p_{3/2}$ core level peak is about 1 eV shifted to higher values in comparison with pure vanadium, which is most probably the consequence of the alloying with the rhodium. On the sample prepared at RT a small V $2p_{3/2}$ peak at a binding energy of 514.6 eV appeared. Its presence is most probably related to formation of surface suboxides and carbides during or

shortly after the V deposition.

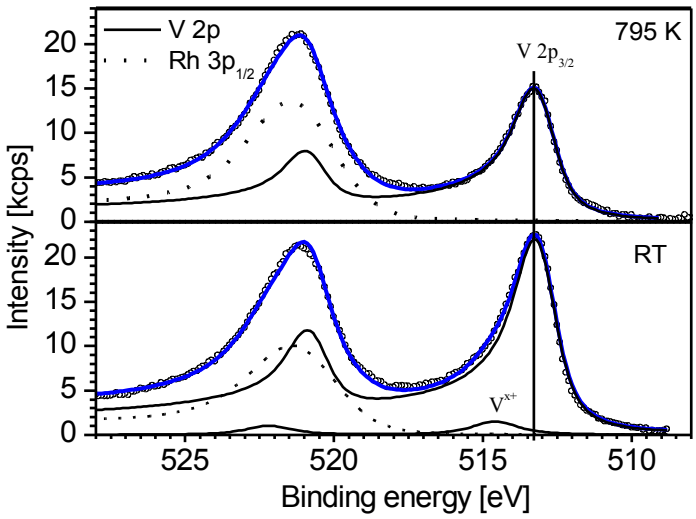

Fig. 4.6: V 2p photoemission spectrum after the deposition of 1 ML of vanadium on the surface of the polycrystalline Rh foil at room temperature (bottom) and at the Rh foil annealed at 795 K (top). Solid lines correspond to V 2p doublets (see the text), the dashed line to Rh $3p_{1/2}$ core level.

The electronic interaction between the vanadium and rhodium can be observed at valence band spectra, which are shown in Fig. 4.7. In the figure, valence band spectra measured by Al Kα x-rays excitation are displayed. Thanks to the polycrystalline nature of the sample and high excitation energy (Sec. 2.5), the photoemission profile of the valence is proportional to the density of occupied electron states. According to theoretical calculations [76], pronounced local maxima in the bulk density of states are predicted at 5.3, 2.6, and 1.2 eV binding energy. In addiction, an increased density of states at the Fermi level at topmost layer is predicted. These theoretical assumptions are in good agreement with the valence band spectrum measured at clean polycrystalline Rh surface. The intensity of the valence band decreased after the deposition of vanadium due to the decreased average concentration of the rhodium within the XPS information depth. Nonetheless, what matters more is the change of the shape of the valence band. The deposition of the vanadium at the room temperature changed the valence band profile only slightly, while a pronounced change of the valence band shape appeared after the V deposition at the elevated substrate temperature. This supports the assumption that the vanadium deposited at the high temperature diffused into the rhodium bulk and formed the subsurface alloy.

The electronic interaction between the vanadium and rhodium atoms caused the changes in the valence band structure. In both cases, the vanadium shifted the valence band centre of mass by 0.06 eV to higher binding energies. The shift of the valence band centroid towards higher BE is typically correlated with the weakening of the CO-metal surface bond (see Introduction). The weakening of the bond confirmed TPD spectroscopy of CO molecules, as described in the following chapter.

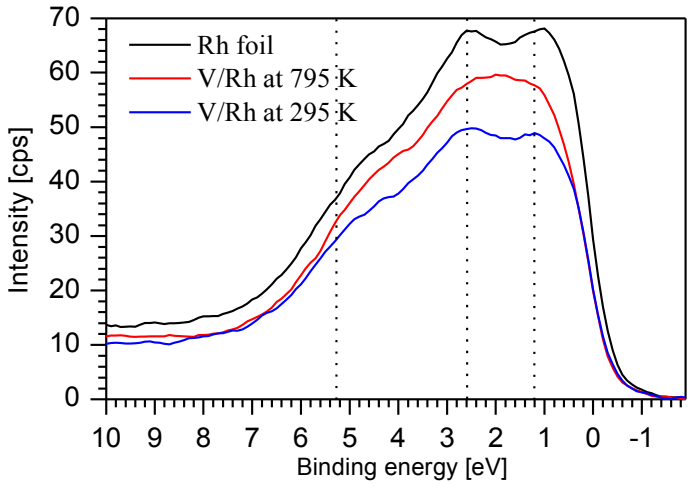

Fig. 4.7: Valence band spectra measured with Al K_α X-ray source. Black curve: spectrum recorded from the clean polycrystalline Rh foil; red curve: after the V deposition (1 ML) at the substrate temperature of 795 K; blue curve: after the V deposition (1 ML) at the substrate temperature of 295 K. The straight lines mark positions of the local maxima in the calculated bulk density of states of rhodium (according to [76]).

4.2.4 Interaction with CO

CO molecule thermal desorption experiments were performed on the clean Rh surface at first. All TPD measurements on the foil were repeated several times to demonstrate the reproducibility. Since the plain Rh foil was annealed at a temperature of 975 K before the experiment, the surface can be considered as plain with low defect density. The obtained TPD spectrum (Fig. 4.8), which followed after dosing 3L CO, was in a good agreement with previous studies on the plain Rh foil [13]. According to single crystal studies, the two TPD states at 480 K and 400 K have been identified as being due to CO molecules desorbing from on-top and hollow/bridge sites, respectively [71,77].

While CO molecules adsorbed very well on the clean Rh surface at room

temperature, there was observed no adsorption, nor desorption of CO on the sample with V evaporated at room temperature. The reason was a fast deactivation of the superficial vanadium deposit. The superficial vanadium atoms reacted with molecules from the ambient vacuum and the surface was covered by vanadium oxides and carbide soon, which was accompanied by a significant increase of O 1s and C 1s photoemission spectra. Such surface became deactivated as far as adsorption of CO at room temperature was concerned. On the other hand, the surface of the second sample, with vanadium deposited at elevated temperature, contained much less oxides and carbides and a significant CO adsorption and desorption was observed (Fig. 4.8). That proved the presence of V mainly under the surface.

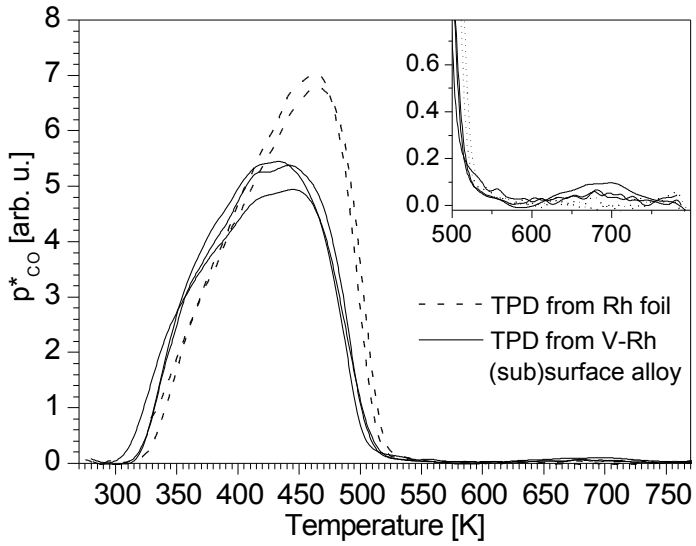

Fig. 4.8: TPD spectra of CO from the clean polycrystalline Rh foil (dashed curve) and from the Rh-V subsurface alloy (solid curve). Both surfaces were exposed to 3L of CO before the desorption measurements and the adsorption/desorption cycles were repeated in order to show the quality of the reproducibility. The inset displays the high-temperature part of the TPD spectra, where recombination peak at 690 K appeared.

The TPD peak of CO desorption was shifted to lower temperatures by about 18 K due to the V doping (Fig. 4.8). This shift in the temperature of the maximum corresponds to the lowering of the desorption energy by about 5 kJ/mol, using the Redhead formula (Eq.(30), Sec. 2.6). The shape of the TPD spectrum was changed, as well. The higher extent of the desorption around a temperature of 400 K indicates a relative increase of the desorption from hollow and bridge sites.

Another difference between CO desorption profiles from rhodium and rhodium

modified by V appeared at higher temperature, shown in the inset in Fig. 4.8. The peak around 690 K corresponds to the so-called recombination or β-peak, which results from the recombination of C and O atoms on the surface to CO molecules. The appearance of the β-peak is the evidence of partial dissociation of the adsorbed CO molecules. The origin of the dissociation could be related to a presence of small vanadium clusters which could be left on the surface. Such case is, however, unlikely as they would be deactivated soon, while the β-peak was observed repeatedly. A surface roughening and increased concentration of surface defects on the alloy surface can be the reason of the here observed CO dissociation

4.2.5 Conclusions

This experiment with V deposited onto polycrystalline Rh showed that the influence of the vanadium on the CO adsorption and desorption properties of the bimetallic system strongly depends on the sample treatment. The surface is soon deactivated if V remains on the top of the surface. On the other hand, the subsurface vanadium influences the chemisorption properties of the superficial rhodium atoms. The strength of the CO bond with the rhodium is lowered on the alloy. The photoemission spectroscopy indicates that the nature of the change is in the electronic changes in the metal surface valence band.

4.3 V on Rh(111)

4.3.1 Introduction

Among all the V–Rh bimetallic systems studied in this work, the greatest attention was given to the V–Rh(111) model system. The goal was to prepare an ordered surface or subsurface alloy and to study the electronic influence of the vanadium on the rhodium and its interaction with gas molecules. This model system enabled us to focus on the electronic effects, while the possible morphological effects could be practically excluded. Experimental conditions which lead to formation of a V–Rh(111)–(2×2) subsurface alloy with long range ordering were found and attention was further focused on this alloy. The homogeneity of the ordered alloy at large scale allowed to use standard far field photoemission techniques to analyse the structure at atomic level and to measure the valence band electron energy dispersion relations. That allowed estimating the atomic structure on the atomic scale level and applying ARUPS method to study the valence band electronic structure in detail.

The first section of this chapter is devoted the characterisation of the V–Rh(111) subsurface alloy by means of SRPES from core levels. In the next two sections, the interaction with CO and O_2 molecules is studied by means of SRPES. In case of CO, TPD measurements were performed, as well. The subsequent section is devoted to the surface atomic structure determination by means of XPD. The last section is focused on the valence band electronic structure investigated by means of ARUPS.

4.3.2 Experimental

The first experiments were carried out at the Materials Science Beamline at Elettra synchrotron in Italy. During this experiment, the conditions which lead to the formation of V–Rh(111)–(2×2) subsurface alloy were found. Later, the experiments with the V–Rh(111)–(2×2) alloy were carried out at XPS/XPD/LEED and XPS/LEED/TPD experimental facilities. At the former facility, atomic structure by means of XPD was investigated and at the latter facility, CO adsorption properties by means of TPD were studied. In each UHV system, more or less the same procedures were followed to prepare the V–Rh(111)–(2×2) subsurface alloy. Each experimental apparatus was equipped with XPS and LEED. These techniques were used to ensure the same V–Rh(111)–(2×2) alloy was prepared as far as the structure and surface

composition was concerned.

The clean Rh(111) surface was prepared by 2 keV Ar^+–ion sputtering, followed by annealing at 1173 K for several minutes, and by heating in O_2 at 973 K for 5 minutes. Then the crystal was flash-heated to 1273 K. This procedure was repeated until the Rh(111) surface was clean. The cleanliness of the Rh(111) surface was checked by Al Kα XPS in combination with LEED.

V–Rh alloys were prepared by vanadium evaporation in vacuum onto clean Rh(111) at 823 K. The residual gas pressure during the evaporation was about 2×10^{-7} Pa. Vanadium metal was evaporated from a vanadium wire placed in a MEBES cell. The evaporation rate was approximately 0.1 ML/min. Here, 1 ML of V is meant to be equal to 1 ML of Rh(111), i.e. 1.597×10^{19} atoms/m^2. In most of the experiments, the same evaporation source was used. Its evaporation rate was calibrated in the XPS/TPD system by means of a quartz crystal microbalance.

The V–Rh(111)–(2×2) subsurface alloy was prepared by the deposition of 2.5 ML of V at a substrate temperature of 823 K and by annealing in steps up to 1023 K when a sharp (2×2) LEED pattern occurred. Another bimetallic sample was prepared by the deposition of 0.4 ML of V at a substrate temperature of 823 K. No LEED surface structure different from (1×1) was observed on this sample.

The first SRPES measurements were carried out at the MSB beamline. The photoelectrons excited by synchrotron radiation were collected in normal emission geometry at 300 K. A photon energy of 382 eV was employed for exciting Rh 3d and C 1s core levels and a photon energy of 640 eV was used to excite the V 2p and O 1s core levels. Valence band spectra were measured at photon energy 50 eV. The total energy resolution (analyser and monochromator) was 0.08, 0.4 and 0.7 eV at 50, 382 and 640 eV, respectively. Adsorptions of CO and O_2 were performed at the partial pressure of 2.7×10^{-6} Pa at 300 K. The samples were exposed to 10 L of CO, which was sufficient to achieve a saturation coverage at the clean Rh(111) surface. The adsorbed CO molecules were removed from the surfaces by a flash-heating to 673 K. Then, exposure to 11 L of O_2 at 300 K followed.

The CO TPD measurements were carried out at the XPS/LEED/TPD facility at the Department of Chemical Engineering, University of Patras. The exposure to was performed at the partial pressure of 7×10^{-6} Pa at a temperature of 193 K. The TPD spectra were obtained with linear heating rate 1 K/s.

X-ray photoelectron diffraction measurements were carried out at the XPS/XPD/LEED apparatus in Prague, utilizing Al Kα (hν = 1486.6 eV) x-rays source. The angle-resolved XPS spectra were recorded by rotating the sample manipulator. The polar angle between the surface normal and the direction of outgoing (detected) electrons was changed from 0 to 70°. Azimuthal angle range was 84°. Three-fold and mirror crystal surface symmetry was applied in order to get full azimuth XPD patterns.

Valence band maps measured by means of ARUPS were obtained at the MSB beamline. Photon energies 35 and 55 eV were used. The energy resolution was determined by measuring the width of the Fermi level at room temperature. The width was measured to be 225 meV. Since the intrinsic width of the Fermi level at RT is 100 meV, the instrument resolution was about 200 meV. Angle-resolved UPS spectra were obtained by rotating the sample manipulator. The polar angle between the surface normal and the direction of detected photoelectrons was changed from 0 to 70°. The azimuthal angle rotation was done in the range of 80°. The acceptance angle of the analyser was 4°.

4.3.3 SRPES characterization

Photoemission spectra from vanadium after the deposition of 0.4 ML and 2.5 ML of V at 823 K are displayed in Fig. 4.9(a and b) together with the LEED patterns obtained after the deposition. Shortly after the deposition of 2.5 ML of V, the sample was annealed at 1023 K and the corresponding spectrum and LEED pattern are displayed in Fig. 4.9(c). After the deposition of 0.4 ML of V, LEED pattern was identical with LEED from clean Rh(111) (not shown), no long-range surface reconstruction was observed. On the other hand, a weak (2×2) LEED superstructure appeared after the deposition of 2.5 ML of V and this pattern became sharp after the annealing. In the experiment with V on polycrystalline Rh as well as in studies [23,34] it was observed that the deposition of V at elevated temperature leads to diffusion of vanadium into Rh. The higher V 2p intensity after the deposition of 2.5 ML V corresponds to a higher vanadium concentration on the surface. The annealing at 1023 K stimulated further diffusion of vanadium into the bulk and resulted in V 2p peak almost identical with the one at the sample with 0.4 ML V. The binding energy of the V $2p_{3/2}$ peak was 512.7 eV, which is about 0.5 eV higher value in comparison with metallic vanadium.

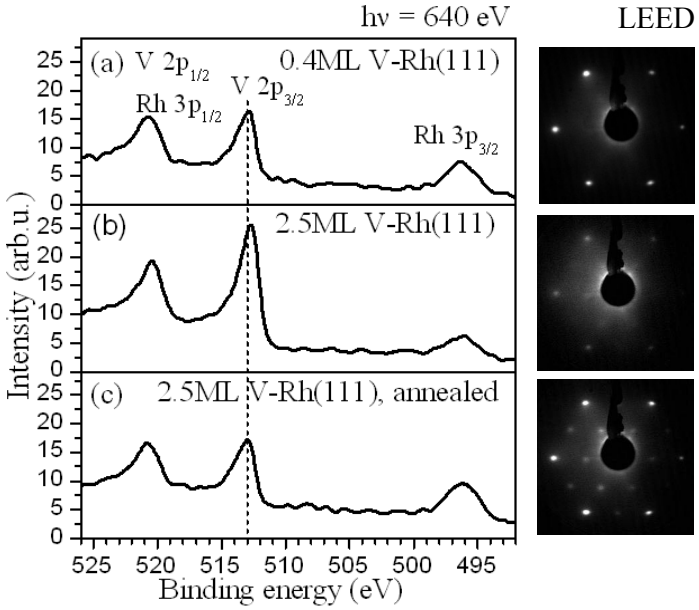

Fig. 4.9: V 2p photoemission spectra (measured using a photon energy of 640 eV) from the V–Rh(111) surface after the evaporation of (a) 0.4 ML of V, (b) 2.5 ML of V and (c) after the annealing the latter one at 1023 K. LEED patterns from the surfaces are shown on the right.

In Fig. 4.10, Rh $3d_{5/2}$ core-level spectra from the clean Rh(111) and V–Rh(111) alloy surfaces are compared. Photoemission at 382 eV photon energy is extremely surface sensitive due to the low kinetic energy of Rh $3d_{5/2}$ electrons (about 76 eV). Thus, the component from the topmost surface layer can be distinguished readily. The Rh $3d_{5/2}$ spectra of the pure surfaces, as well as those ones after the exposure to a saturation dose of CO, were decomposed into the bulk (denoted as *B*) and surface (denoted as *S* and S_a) components iteratively. The CO adsorption influenced only the Rh atoms of the topmost layer which helped to identify the surface components as it will be shown further. For the decomposition of the measured spectra, Shirley-type background [35] and Doniach-Šunjić line shapes [35,75] convoluted with Gaussian profiles were used. Binding energy values are accurate within 0.05 eV. Energy positions of the peaks in Fig. 4.10 and their relative areas are listed in Table 4, where the relative areas of the bulk (*B*) and surface (*S* and S_a) components are referred to the bulk and surface component of the clean Rh(111) crystal. The binding energies of the bulk (307.15 eV) and surface (306.67 eV) component on Rh(111) are in good agreement with values reported, for instance, in [78].

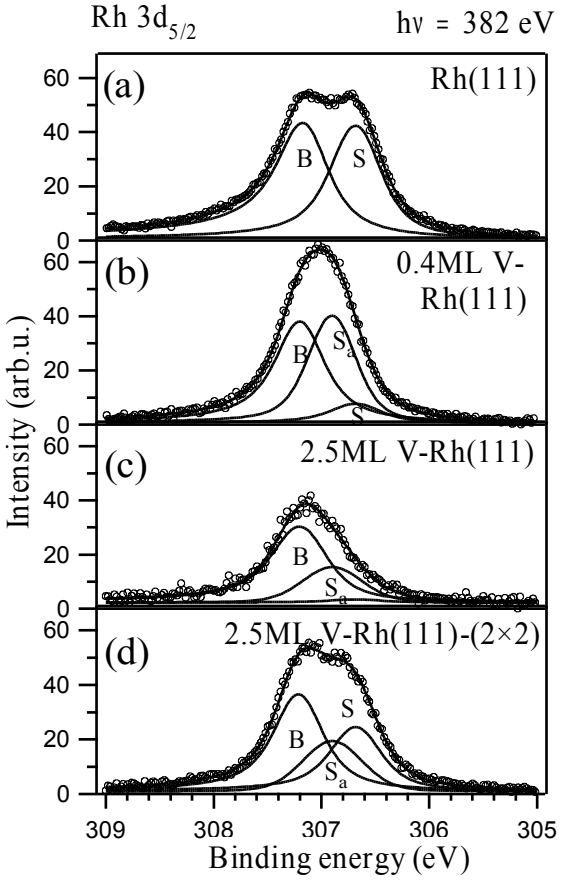

Fig. 4.10: Rh $3d_{5/2}$ core-level photoemission spectra of (a) the clean Rh(111) and (b–d) V–Rh(111) alloy surfaces. The spectra were decomposed into bulk component (B), surface component (S) and surface component correspondent to Rh atoms with a bond with vanadium (S_a).

After the deposition of 0.4 ML of V at the elevated temperature a new surface component (denoted as S_a) at 306.89 eV appeared. A small clean rhodium surface component *S* was present, too. Table 4 shows that the sum of the relative intensities of the surface components *S* and S_a on the alloy equalled 96% of the intensity of the clean Rh surface component. That indicates the topmost layer practically vanadium free. Therefore, the S_a component was ascribed to Rh in the first layer directly influenced by the subsurface vanadium. The same surface component S_a was identified also on the Rh surface after the deposition of 2.5 ML of V (Fig. 4.10(c)). The overall low intensity of Rh $3d_{5/2}$ spectrum just after the 2.5 ML V deposition was caused by the attenuation by vanadium presented on the surface as was already indicated by V 2p photoemission. Further annealing, which stimulated the V diffusion and (2×2) LEED appearance, caused the increase of the Rh $3d_{5/2}$ peak

intensity to the value obtained after the deposition of 0.4 ML V. The same surface component S_a was present and in addition, relatively intense clean surface component *S* appeared. This probably reflects some heterogeneity on the surface and presence of clean surface areas. The sum of the relative areas of both surface components corresponded to 97% of the clean Rh(111) (see Table 4) surface component, which again indicates almost vanadium free topmost layer.

Sample	Peak	Peak position (eV)	Rel. peak area (%)
Rh(111)	B	307.15	100
	S	306.67	100
0.4 ML V–Rh(111)	B	307.19	78
	S	306.67	17
	S_a	306.89	79
2.5 ML V–Rh(111)	B	307.19	62
	S	306.67	3
	S_a	306.89	29
V–Rh(111)–(2×2)	B	307.20	72
	S	306.67	56
	S_a	306.89	41

Table 4: Binding energies and relative intensities of the Rh $3d_{5/2}$ components at Rh(111) and V–Rh(111) subsurface alloys measured at a photon energy of 382 eV and displayed in Fig. 4.10. Peaks denoted by B are bulk components and their intensity is related to the intensity of the bulk component on clean Rh(111). Similarly, peaks denoted by S and S_a correspond to surface components with intensities related to the surface component of clean Rh(111).

The valence bands of clean Rh(111) and the V–Rh(111) subsurface alloys obtained at a photon energy of 50 eV are presented in Fig. 4.11. The spectra are dominated by the contribution from rhodium valence band states due to the high Rh 4d photoionisation cross-section at the used photon energy. The modifications of the valence band photoemission profile upon alloying were similar on both alloy surfaces. A shift of the valence band centre-of-mass toward higher binding energy was expected as it is common for late-transition metals [9] and as it has been observed on the polycrystalline rhodium substrate (Fig. 4.7) and on a similar V–Pd(111) subsurface alloy [24]. However, no shift of the centroid to higher binding energy was observed in this case. On the other hand, a considerable reduction of

valence states in low energy (0–1.5 eV) valence band region occurred. The valence band electronic structure of the V–Rh(111)–(2×2) will be studied in detail by means of ARUPS in a a next chapter.

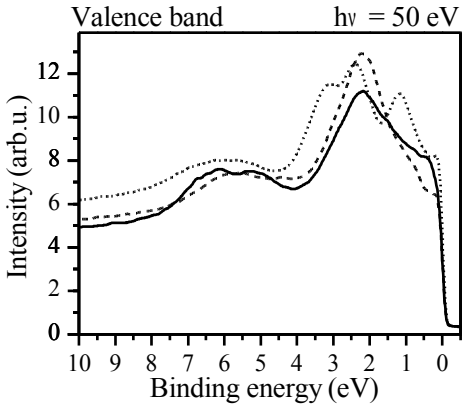

Fig. 4.11: Valence band photoemission spectra measured at a photon energy of 50 eV. Dotted curve corresponds to clean Rh(111), dashed curve to the 0.4 ML V–Rh(111) subsurface alloy and the full curve corresponds to the 2.5 ML V–Rh(111)–(2×2) subsurface alloy.

4.3.4 Interaction with CO

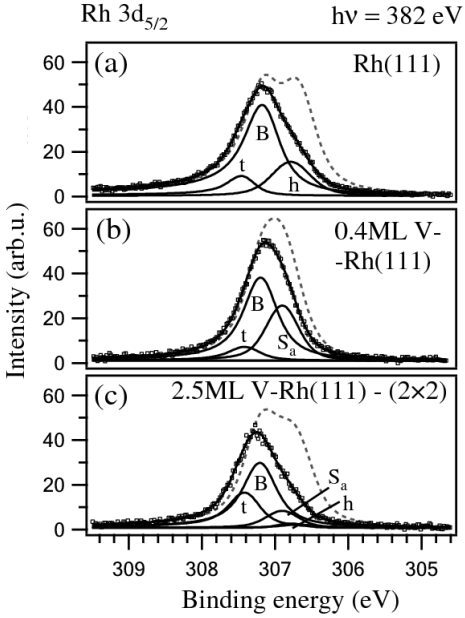

Fig. 4.12: Rh $3d_{5/2}$ photoemission spectra before (circles and solid lines) and after the exposure to 10 L of CO (squares and dashed lines). The components corresponding to the emission from bulk (B) and surface (S, S_a) atoms are displayed together with the components induced by the CO adsorption. The component t is due to the emission from the surface Rh atoms with CO in on-top sites and the component h is due to the emission from the atoms with CO molecules in three-fold hollow sites.

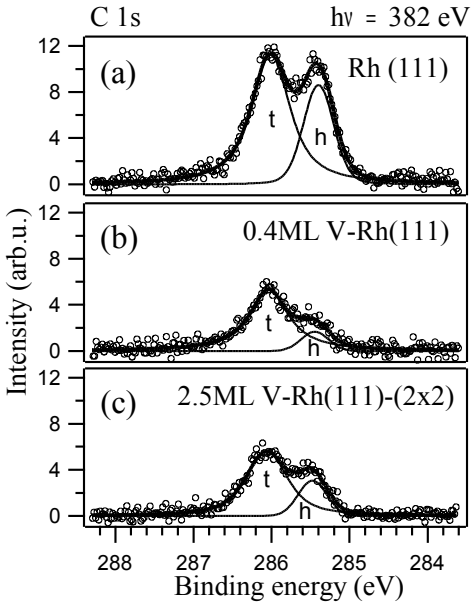

Fig. 4.13: C 1s photoemission spectra of (a) Rh(111) and (b, c) V–Rh(111) alloy surfaces after the dose of 10 L of CO at 300 K. The component t corresponds to CO molecules adsorbed in on-top sites and the component h to CO molecules in three-fold hollow sites on the (111) surface.

After the preparation of clean Rh(111) and the V–Rh subsurface alloys, the surfaces were exposed to 10 L of CO. After such exposure, the CO adsorption on clean Rh(111) is saturated at 300 K [79]. The influence of the adsorbed CO molecules on the Rh $3d_{5/2}$ core-level spectra is demonstrated in Fig. 4.12. On the Rh(111) surface, with the adsorbed CO, a good fit was obtained with bulk component and two components at 307.43 eV (*t*) and 306.78 eV (*h*). These CO-induced components have been assigned [78] to Rh atoms underneath single on-top CO molecule (component *t*) and to Rh atoms underneath the CO molecules adsorbed in three-fold hollow sites (component *h*). The same components were also used to decompose the spectra of the V–Rh subsurface alloys after the exposure to CO.

Because of the lack of energy resolution for such high number of components, the decomposition is less reliable, especially because of the overlap between S_a and *h* components. Nevertheless, the trend in the intensity ratio between *t* and *h* components is in good agreement with C 1s spectra displayed in Fig. 4.13. The C 1s spectra consisted of two components which corresponded to CO in on-top sites (286.03 eV) and in hollow sites (285.44 eV) [78]. The total area of C 1s spectrum is proportional to the CO surface coverage. Taking this into account, the CO coverage on the alloy surfaces decreased to 33% (Fig. 4.13(b)) and 42% (Fig. 4.13(c)) of the value on clean Rh(111) (Fig. 4.13(a)). Moreover, the adsorption in three-fold hollow sites was suppressed more than the adsorption in on-top sites. No significant changes have been observed in the V 2p signal apart from a small decrease of the intensity after the CO adsorption. That indicated an interaction of the adsorbed CO molecules solely with rhodium.

The influence of the subsurface vanadium on Rh–CO bond strength can be deduced from the energy difference between 4σ and 5σ/1π CO molecular levels. They are presented in Fig. 4.14. According to studies [80-82] 4σ and 5σ/1π energy difference is correlated with CO bond strength and it is inversely proportional to the CO–metal bonding interaction. It has been found that the 4σ– 5σ/1π energy difference increases with the decreasing CO adsorption energy. An increase of the energy difference by 0.1–0.2 eV on the alloy surfaces, as compared with the clean Rh(111), can be seen in the figure. The increase in the molecular orbital energy separation indicates a weakening of the CO-Rh bond at the V–Rh(111) alloy surface.

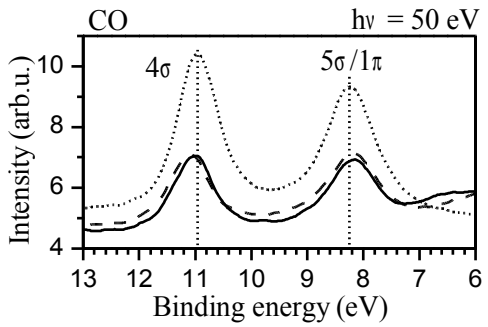

Fig. 4.14: Photoemission spectra of 4σ and 5σ/1π orbitals of CO molecules adsorbed on the clean Rh(111) and V–Rh(111) subsurface alloys. The spectra were recorded after exposure to 10L of CO at 300 K.

The weakening of the CO–Rh bond was confirmed by the TPD spectroscopy, summarized in Fig. 4.15. In the figure, TPD spectra of CO desorption from the clean Rh(111) and V–Rh(111)–(2×2) subsurface alloy are compared. The series of TPD curves correspond to different initial CO doses. All the exposures to CO were performed at a substrate temperature of 193 K. The CO desorption peaks between 510 K and 480 K were observed at lower exposures on both surfaces. A peak around 420 K was formed at higher CO coverages. The high-temperature peak is assigned to CO molecules in on top sites and the molecules desorbing at lower temperatures are assigned to CO in hollow and bridge adsorption sites on the clean Rh(111) surface [77].

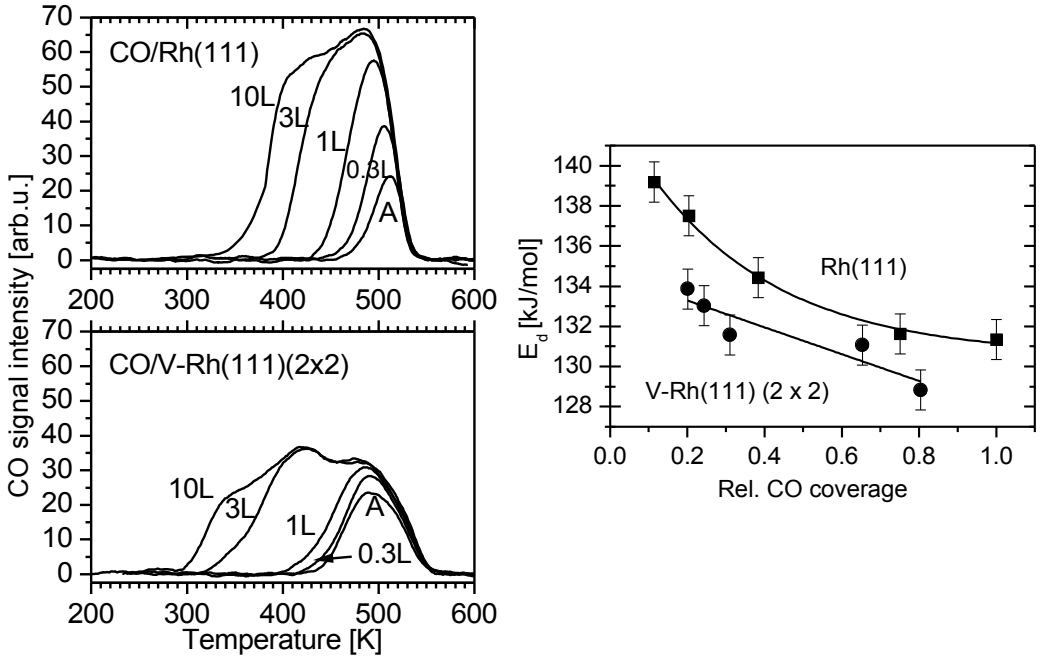

Fig. 4.15
Left: TPD spectra of CO measured at clean Rh(111) (upper left) and V–Rh(111)–(2×2) alloy (lower left). The spectra were obtained after the dose of 0.3, 1, 3 and 10 Langmuirs of CO at the substrate temperature of 193 K. The character A is assigned to the adsorption from the ambient atmosphere.
Right: Plotted desorption energies of the high-temperature desorption peak as a function of relative CO coverage. The coverage is evaluated with respect to the saturation coverage at the clean Rh(111) surface.

The high-temperature peak was shifted to lower temperatures by about 15 K on the V doped surface. The desorption activation energies of the high temperature TPD peak are plotted as a function of relative CO coverage on the right of Fig. 4.15. The energies are calculated by the Redhead analysis (Eq.(30), Sec. 2.6) and the relative

coverage is evaluated with respect to the saturation coverage at the clean Rh(111) surface after the exposure to 10 L dose of CO. The desorption energy E_d was lowered by about 4 kJ/mol on the V doped surface. The relative intensity of the desorption peak around 420 K, which has been assigned to the desorption from hollow and bridge sites, significantly increased in reference to the desorption peak from on-top sites. The same change was observed in TPD spectra on polycrystalline Rh doped with V as well as on the mixed Rh–V layers γ-Al_2O_3. Since the C 1s spectra from CO adsorbed at RT showed that adsorption in on-top sites on the subsurface alloy is more preferable than in hollow sites, the increased desorption from hollow sites must be the result of changed CO intermolecular interaction and diffusion barriers between the different adsorption sites. In addition, presence of a new type of low-energy CO adsorption sites on the subsurface alloy is indicated by the CO desorption between 300 and 350 K after the exposure to 10 L of CO. The new desorption peak could be from the adsorption positions directly affected by the subsurface vanadium or from new positions that could arise from the (2×2) surface reconstruction.

4.3.5 Interaction with O_2

The both V–Rh alloy surfaces with 0.4 and 2.5 ML of V were exposed to 11 L dose of O_2 at 300 K. After that the samples were flash heated to 673 K. Interaction of the surfaces with oxygen was observed by measuring O 1s, V 2p and valence band spectra, which are displayed in Fig. 4.16.

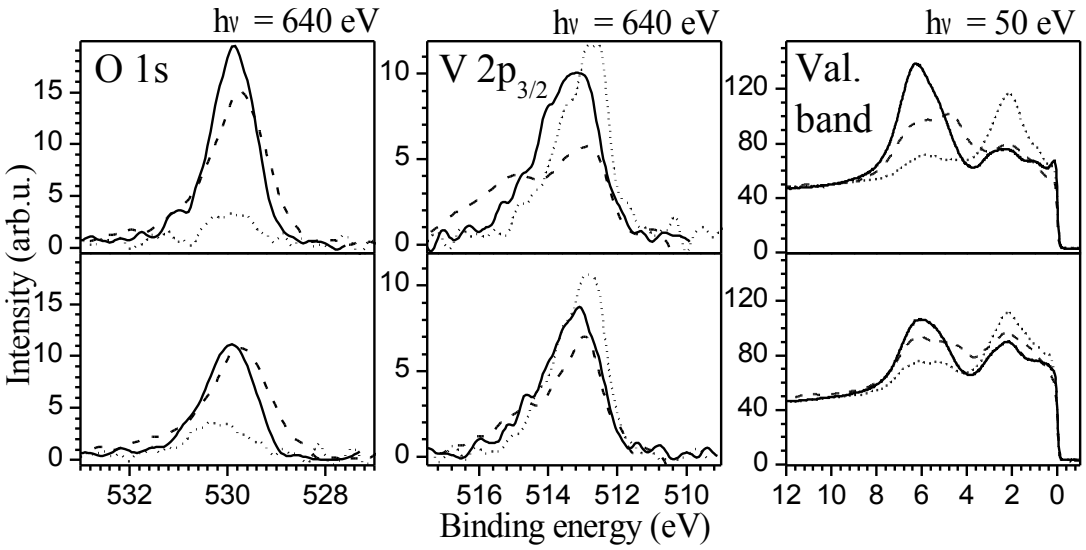

Fig. 4.16: O 1s, V 2p$_{3/2}$ and valence band photoemission spectra of the 0.4 ML V–Rh(111) (top) and 2.5 ML V–Rh(111)–(2×2) (bottom) alloy. Dotted curves correspond to the surfaces before the O_2 dose, dashed curves to the surfaces after the 11 L O_2 dose and solid curves after the heating at 673 K.

Spectra on the top and bottom of the Fig. 4.16 correspond to the alloy formed after the deposition of 0.4 ML of V and the alloy with (2×2) reconstruction, respectively. The spectra showed that the interaction between the adsorbed oxygen and the V–Rh alloy surface was very similar on both samples. The O 1s spectra showed that there were some traces of oxygen even before the exposure to O_2. After the exposure to 11 L of O_2, an asymmetric O 1s peak with its maximum at 529.7 eV appeared. This BE corresponds to dissociated oxygen atoms adsorbed on Rh surface in threefold fcc hollow sites [79,83]. The asymmetric shape of the peak is related to an interaction of some adsorbed oxygen with the subsurface vanadium as indicated V 2p$_{3/2}$ spectra after the exposure. A new state around 515 eV appeared in the V 2p$_{3/2}$ spectra. The new state can be assigned to a vanadium oxide [83], which indicates vanadium surface segregation induced by adsorbed oxygen already at the low temperature of 300 K. Finally, the samples were shortly heated to 673 K after the 11 L O_2 dose. The O 1s peak became narrower and it was shifted to 529.9 eV BE after the flash. Its total area remained unchanged. The V 2p$_{3/2}$ spectrum was narrowed as well, shifted to a BE of 513.5 eV and its area increased by about 60%. Obviously, the higher temperature stimulated interaction between the adsorbed oxygen and the subsurface vanadium which caused back-diffusion of the subsurface vanadium to the surface

and creation of a vanadium sub-oxide. Simultaneously with the changes in the O 1s and V $2p_{3/2}$ core level spectra, a prominent feature around 6 eV in the valence band appeared. The position of the feature is in coincidence with O 2p states of adsorbed oxygen. However, at the photon energy of 50 eV, valence states of rhodium dominate [52] and the O 2p signal is low on pure rhodium. The increase of the intensity of the states at 6 eV BE after the heating is assigned to O 2p–V 3d hybridization and resonant photoemission close to the photon energy of 50 eV [84]. The estimation of the exact oxidation state of an ultra-thin vanadium oxide layers is difficult due to the influence of the interfacial bonding and the proximity of the underlying metal surface. It modifies both the initial and final state in the photoemission process [85]. The V $2p_{3/2}$ measured at a BE around 515 eV could indicate formation of a (2×2)–V_2O_3/Rh(111) structure with corresponding V $2p_{3/2}$ at a BE of 514.6 eV [86]. However, other stable vanadium oxide phases with V $2p_{3/2}$ between 514 and 515.4 eV BE have been observed. Temperature reduction of highly oxidized $(\sqrt{7}\times\sqrt{7})R19.1°$–$VO_3$ monolayer on Rh(111) [87] results in oxide phases with VO_3, $V_{11}O_{23}$, $V_{11}O_{21}$, and V_2O_3 stoichiometry. Any of these vanadium oxides or a multiple phase vanadium oxide could be formed. Annealing of the alloy with the adsorbed oxygen stimulates further vanadium surface segregation and formation of a surface vanadium oxide under the given experimental conditions. The binding energy of the V$2p_{3/2}$ peak was shifted to a value of 513.2 eV and could be assigned to the "wagon wheel"–VO/Rh(111) structure with V^{2+} oxidation state [87].

Some other changes in the valence band spectra appeared during the oxidation of vanadium. The states localized around 2.2 eV significantly decreased and the intensity of the states near the Fermi level relatively increased. The shape of the low energy region of the valence band became more comparable with the clean Rh(111) surface. The reaction between the oxygen and vanadium caused a degradation of the Rh–V heteroatomic bond. A strong bonding of the adsorbed oxygen with the bimetallic surface was confirmed by exposure to 10 L CO at temperatures 300, 363 and 423 K. No reduction was observed in contrast to the total clean-off reaction of the adsorbed oxygen with CO under the same conditions on the clean Rh(111) surface.

The sample with the (2×2) reconstruction and after the oxidation was heated up to 1173 K in steps. The sample was cooled down to 300 K after each step and

intensities of V $2p_{3/2}$, O 1s and Rh $3d_{5/2}$ core-levels were monitored by XPS stimulated by Al Kα radiation (Fig. 4.17). The oxygen was reduced systematically with increasing temperature, while the intensity of vanadium remained practically constant up to a temperature of 1023 K. A significant decrease of vanadium signal was observed at 1073 K, and it continued at higher temperatures. This decrease was caused by dissolution into the rhodium substrate.

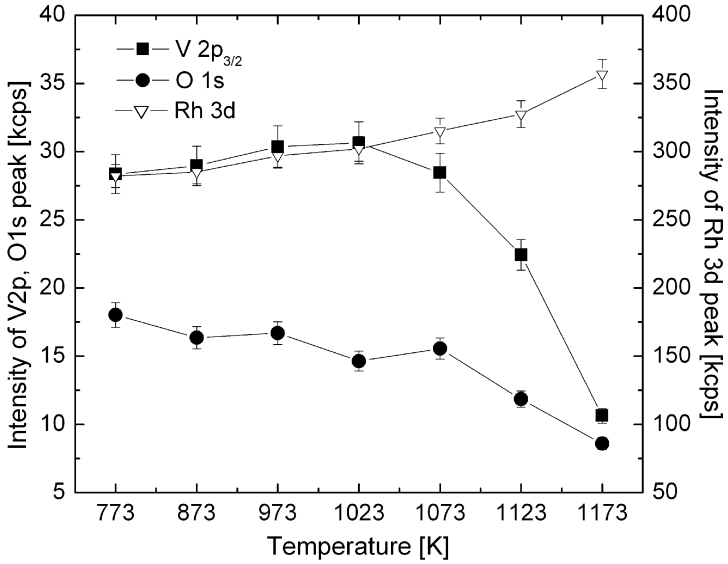

Fig. 4.17: The development of the integrated intensities of the V $2p_{3/2}$, O 1s and Rh 3d XPS peaks during the heating of the V–Rh(111)–(2×2) alloy up to 1173 K.

4.3.6 Atomic structure of V–Rh(111)–(2x2) alloy

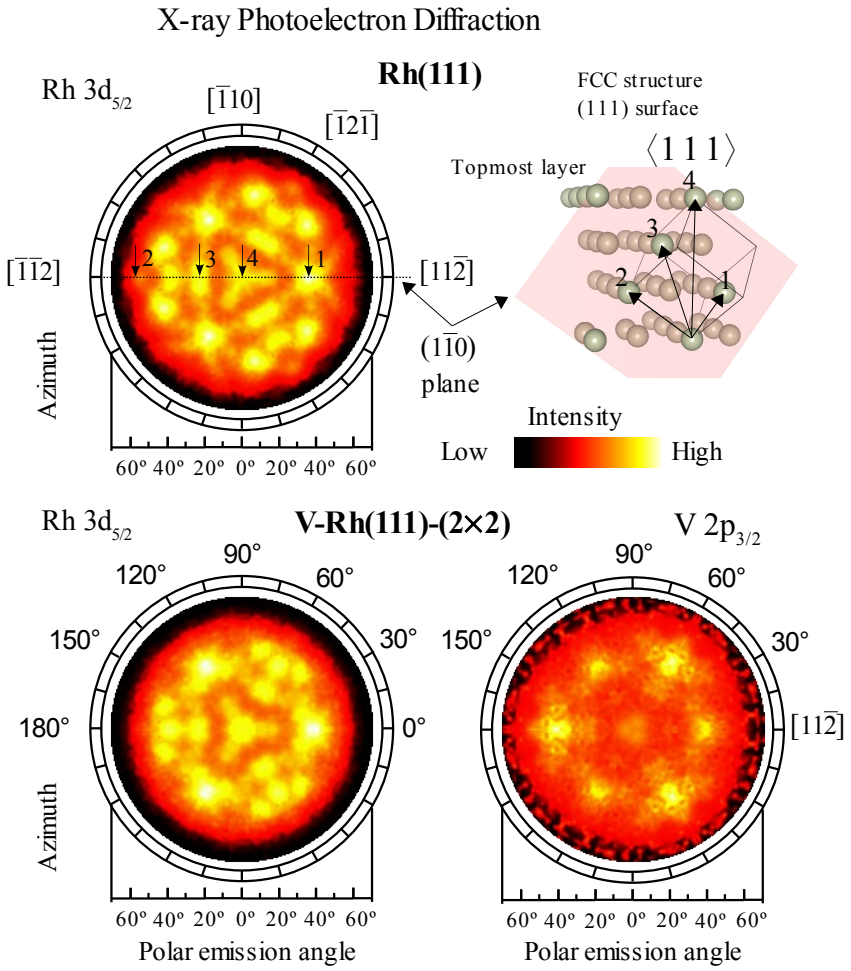

Fig. 4.18: . X-ray photoelectron diffraction (XPD) patterns of pristine Rh(111) (top) and V–Rh(111)–(2×2) subsurface alloy (bottom). The patterns were obtained by plotting emission angle dependence of Rh $3d_{5/2}$ and V $2p_{3/2}$ integrated intensities. Main FS peaks in $(1\bar{1}0)$ plane are indicated by numbers 1–4 in the XPD from clean Rh(111) and the corresponding emitter–scatterer geometry is sketched on the right. The photoemission spectra were measured using Al Kα X-ray radiation.

In order to get an insight into the local atomic structure of the alloy which revealed the (2×2) LEED pattern, an XPD experiment was performed. Rh $3d_{5/2}$ and V $2p_{3/2}$ peak areas were measured as a function of emission angle using Al Kα X-ray radiation. The correspondent diffraction patterns are displayed in Fig. 4.18. The pattern on the top, recorded on the clean Rh(111) crystal, is a typical XPD pattern of an fcc(111) surface. Scattering of photoelectrons on the nearest neighbours of an emitting atom is responsible for the so-called forward-scattering (FS) peaks denoted by numbers in the $(1\bar{1}0)$ plane in Fig. 4.18. The atomic arrangement of the emitter

and the scatterers in the FS peaks is sketched on the right of the pattern. After the V–Rh(111)–(2×2) alloy was formed, the XPD of Rh $3d_{5/2}$ showed a pattern very similar to the one from the clean Rh(111). Despite it was more blurred, the main features such as FS peaks were preserved. The FS peaks were also apparent in the V $2p_{3/2}$ XPD pattern which was a clear evidence of the Rh–V alloy with V atoms in substitutional positions in the Rh crystal lattice. The presence of FS peak in normal direction (denoted by number 4) in the vanadium pattern also indicated that the vanadium atoms were located in substitution positions at least down to the fourth layer from the surface.

While there was clear evidence of V atoms in substitutional positions in Rh single crystal lattice, it was not so obvious which of the possible substitutional V–Rh alloys was formed. Previously a (2×2) and $(\sqrt{3}\times\sqrt{3})R30°$ structures (but only with small domain sizes of several Å) have been reported [30,31] and the $(\sqrt{3}\times\sqrt{3})R30°$ structure have been considered as the most stable [21]. However, our electron diffraction measurements show that the formation of the (2×2) structure is favoured under the used experimental conditions. As far as the bulk Rh–V alloys is concerned, three ground state fcc structures were derived: an $L1_0$ of RhV stoichiometry and two $L1_2$ structures of Rh_3V, as was summarised in Sec. 1.4 . The structure of the (111) plane of Rh_3V alloy has hexagonal configuration with a V–(2×2) superstructure (Fig. 1.4), which corresponds to the (2×2) pattern observed by LEED. In addition, the decrease of the Rh $3d_{5/2}$ core-level intensity by about 25% (see Table 4) is also in good agreement with the suggested stoichiometry. Calculations of Wolverton *et al.* [29] indicate that the RhV structure is thermodynamically the most stable. However, the calculations have been done for bulk and the situation is often different at surfaces. Indeed, the minimum of the energy of formation of a V impurity in the layers close to the Rh(111) surface at the total V-concentration of 0.25 was predicted by *ab-initio* calculations [30]. All these indications are pointing to Rh_3V compound alloy of $L1_2$ structure with the vanadium free topmost (111) surface layer.

The experiment with CO adsorption as well as XPS from surface states strongly indicates that the topmost layer of the V-Rh alloy was vanadium free. Therefore, the (2×2) structure observed by LEED must be a result of a reconstruction of the surface Rh atoms. Previously, Konvicka *et al.* have studied V–Rh(111) subsurface alloy with submonolayer amount of V by STM [30]. Triangle-like features ordered in (2×2)

structures of small domain sizes were observed. A model of the surface atom reconstruction has been proposed Fig. 1.5. According to this model, V atoms in the second layer induced a strong lateral contraction of the Rh atoms above the subsurface vanadium atoms forming the triangles in the topmost layer.

However, our XPD measurements did not confirm the proposed lateral contraction on the surface. The atoms in the triangles correspond to the first neighbours to V sites in the second layer of fcc structure. Any strong lateral contraction would shift the corresponding FS peaks (labelled as number 1 in Fig. 4.18) to lower polar angles. The polar-angle dependence of Rh $3d_{5/2}$ and V $2p_{3/2}$ peak areas in $[11\bar{2}]$ azimuth is displayed in Fig. 4.19. One can see that the FS peak in [110] direction from both Rh and V in the alloy was shifted by about 2 degrees to a higher polar angle in comparison to the clean Rh(111) substrate.

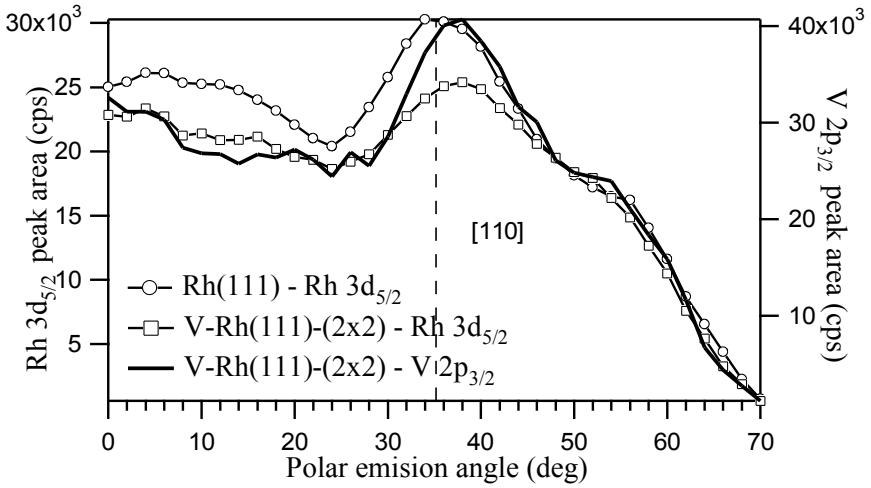

Fig. 4.19 Polar emission angle dependence of Rh $3d_{5/2}$ and V $2p_{3/2}$ integrated intensities in $[11\bar{2}]$ azimuth. The vertical line at 35.3° corresponds to the FS on the nearest neighbour in the [110] *direction at an ideal fcc(111) surface.*

In order to quantitatively analyse the surface reconstruction of the V–Rh(111)–(2×2) alloy, the experimental XPD data were compared with theoretical calculations and analysed by means of reliability factors described in Sec. 2.3 . The XPD data were simulated by EDAC code (Electron Diffraction on Atomic Clusters) [38] for core level photoelectron diffraction simulations. Multiple scattering cluster model approach was used considering a hemispherical cluster. At first, several parameters of the cluster model had to be estimated. The parameters can be categorized into two main groups. The first group contains structural parameters which characterize

positions of the atoms in the studied crystal structure. The second group consists of inner code parameters such as geometry of the beam and analyser, energy and angle scanning parameters, initial core-state quantum numbers and multiple-scattering parameters. In the here presented *R*-factor analysis, only structural parameters were varied. Before that, all the inner parameters had to be determined. The geometry of the beam and analyser as well as the energy and scanning parameters were set to be the same as in the experiment. Parameters such as IMFP, inner potential, and Debye temperature were estimated from literature.

Inelastic mean free path IMFP for photoelectrons from Rh $3d_{5/2}$ and V $2p_{3/2}$ core levels was calculated (using TPP-2M formula [36]) to be 15 Å and 13.7 Å, respectively. Debye temperature was set to be 197 K [88]. The inner potential was estimated to be 11 eV. This value was estimated from theoretical study of the Rh(111) surface valence band electronic structure [76,89]. It have been found out that a deviation of 4 eV from the inner potential and 70 K in Debye temperature did not have effect on the values of the structural parameters which led to the best match between experimental and theoretical XPD data.

Other parameters such as the cluster size, number of emitters, order of the multiple-scattering and maximum orbital quantum number l_{max} were optimised concerning the CPU calculation time. At the same time, their effect on the structural parameters was checked as well.

The effect of the cluster size is illustrated in Fig. 4.20. The figure shows Rh $3d_{5/2}$ XPD from the clean Rh(111) surface. On the left, experimental pattern (Fig. 4.20(a)) is displayed. The other patterns are calculated by EDAC code for two different sizes of the cluster. The pattern (b) was calculated using cluster of 1000 atoms, the pattern (c) is the result obtained at 200 atoms cluster. It is clear that the larger cluster simulation match the experimental pattern better than the smaller cluster simulation. In fact, cluster of the size of about 2000 atoms should be considered according to the calculated IMFP of the electrons with the kinetic energy of 1179 eV. However, CPU time needed to calculate XPD for such large cluster was several hours, while the calculation for 200 atoms cluster took less than one hour. Moreover, all the main XPD features remained. The reason is in the relatively high kinetic energy (about 1 keV) of the emitted photoelectrons. At high kinetic energies, the diffraction patterns are dominated by forward scattering spots at low-index directions as a result

of scattering on the nearest and next-nearest neighbour atoms [37]. Therefore, the geometrical reconstruction of the surface atoms have a significant influence on the XPD patterns and clusters of the size of 200 atoms, which correspond to 6 atomic layers, turned out to be sufficient to find structural parameters with the best fit to the experiment.

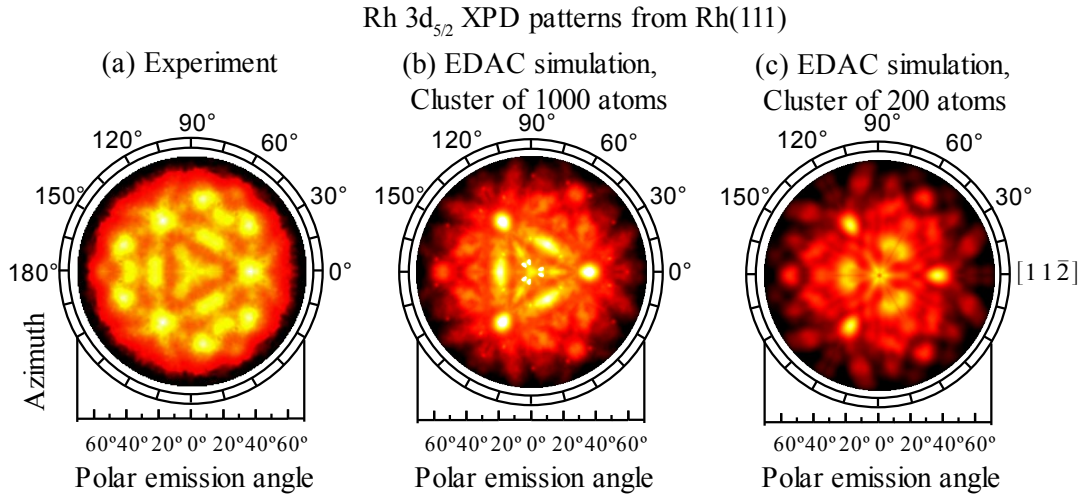

Fig. 4.20: Measured (a) and simulated (b,c) XPD patterns obtained at Rh(111) surface.

As far as the other inner parameters is concerned, it was found that multiple-scattering of the order of 5 and the maximum orbital quantum number l_{max} = 12 were sufficient to find the best structural parameters. On the account of emitters, emitters in the second, third and fourth layer were considered. The effect of emitters from the top surface layer was negligible due to the reduced back-scattering at the kinetic energy of 1 keV.

The model of the atomic cluster used to refine the structural parameters is illustrated in Fig. 4.21. The hemispherical cluster consists of 200 atoms arranged in 6 layers. The arrangement of the V atoms corresponds to Rh_3V alloy with $L1_2$ ordering. The structural parameters were varied until the best fit between the theory and experiment was found by means of the *R*-factor analysis (Sec. 2.3). The varied structural parameters are depicted in Fig. 4.22. The parameters correspond to the inward (parameter z_j) and lateral (parameter d_j) contraction of the op layer Rh atoms over the second layer V atoms; the relaxation of the rest of the Rh top layer atoms (parameter z_1); and relaxation of the V atoms in the second layer (parameter z_v).

(a) (b)

Fig. 4.21 Ball model of the hemispherical cluster of atoms used in the EDAC code simulations of the measured XPD diffraction patterns. (a) Side view, (b) top view. Red balls represent V atoms, blue Rh atoms. The cluster consists of 200 atoms in 6 layers. Yellow ball corresponds to the V emitter in the second layer.

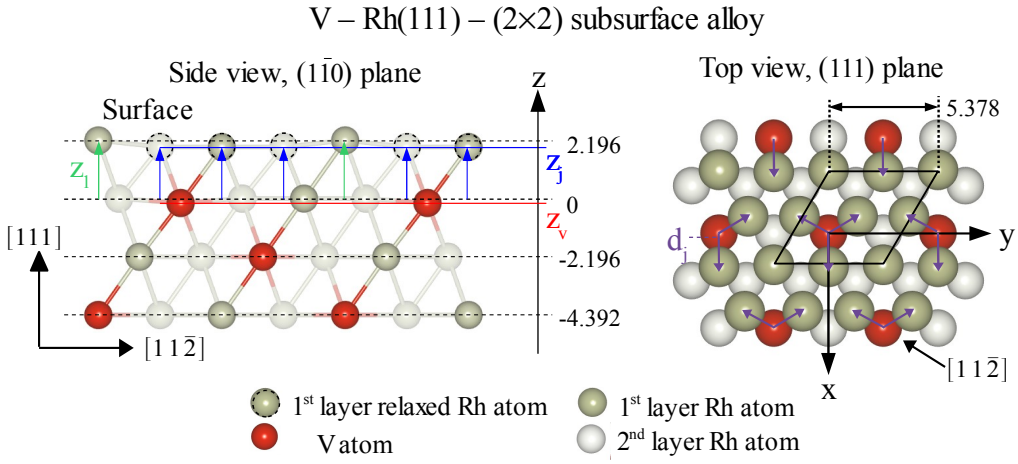

Fig. 4.22: Illustration depicting structural parameters (z_j, z_v, z_1, and d_j) varied in the proposed model of the (2×2) surface reconstruction of the V-Rh(111) subsurface alloy. All lengths are given in Å. The length 2.196 Å corresponds to the inter-planar distance in bulk Rh crystal.

The values of the R_S-factor were the most sensitive to the parameters z_j and d_j (see Fig. 4.22). The dependence of the R_S-factor on these two parameters while keeping the others (z_1, z_v) constant, is shown in Fig. 4.23 and Fig. 4.24. The R_S-factor values were calculated using Eq.(16) given in Sec. 2.3 . Figure 4.23 displays R_S-factor values for the XPD results for the emission from the Rh atoms while keeping parameters z_1 and z_v at values 2.2 Å and 0 Å, respectively. The minimum is at

z_j =1.75 Å and d_j =1.65 Å. Values of d_j, which are lower than 1.55 Å (this value corresponds to an unreconstructed surface), represents the lateral inward contraction of the Rh atoms over the subsurface vanadium atoms, the larger values mean shift in the opposite direction. In case of parameter z_j, values lower than 2.196 Å mean inward shift of the atom positions.

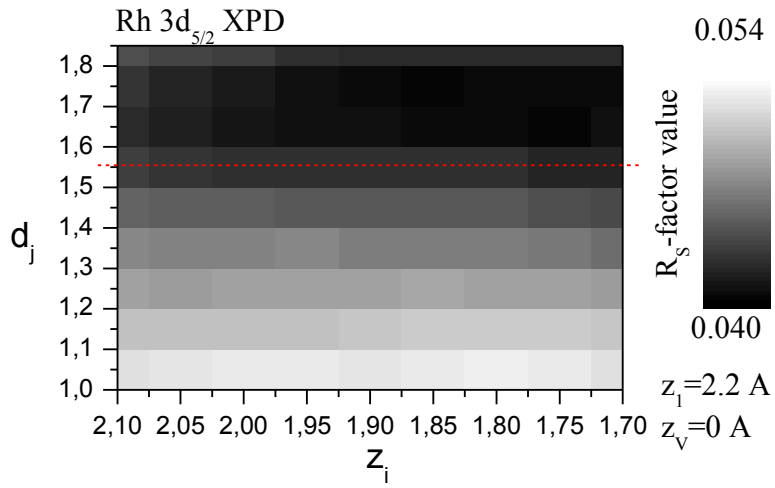

Fig. 4.23: R_S-factor values as a measure of the agreement between experimental and theoretical XPD pattern for Rh $3d_{5/2}$ photoemission from the V–Rh(111)–(2×2) surface. Two structural parameters zj and d_j were varied in the theoretical model, while the other two z_1 and z_v were kept constant. The dashed red line corresponds to the d_j of unreconstructed Rh(111) surface.

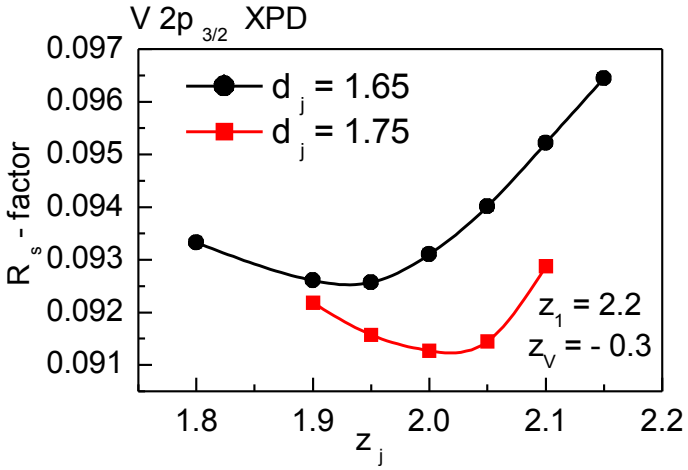

Fig. 4.24: R_S-factor values as a measure of the agreement between experimental and theoretical XPD pattern for V $2p_{3/2}$ photoemission from the V–Rh(111)–(2×2) surface. Two structural parameters z_j and d_j were varied in the theoretical model, while the other two z_1 and z_v were kept constant.

Figure 4.24 shows the same as Fig. 4.23 but the values correspond to XPD from

vanadium atoms. The values of R_S-factor in this graph were calculated while keeping parameters z_1 and z_v kept at values 2.2 Å and -0.3 Å, respectively. In case of XPD from vanadium, the minimum of the R_S-factor correspond to z_f=2.0 Å and d_f=1.75 Å. The both graphs with *R*-factor values indicate that the *R*-factor analysis of the XPD patterns from rhodium and vanadium give different values of the structural parameters. On the other hand, they agree in the directions of the shift of the new positions of the surface Rh atoms. The same trend was also found in the case of the other two parameters z_1 and z_v. The discrepancies in the exact values of the structural parameters were included into the values of uncertainty.

The inward relaxation of the Rh atoms over the subsurface vanadium was found to be 0.3 ± 0.2 Å. As far as the lateral contraction is concerned, the simulations indicate that the contraction is not above the subsurface vanadium atoms but in the opposite direction, as indicated in Fig. 4.22. The simulations further indicate inward relaxation of the second layer vanadium atoms by 0.2 ± 0.1 Å.

The proposed model of the V–Rh(111) subsurface alloy with (2×2) surface reconstruction is drawn in Fig. 4.25. Some experimental and calculated intensities are compared in Fig. 4.26.

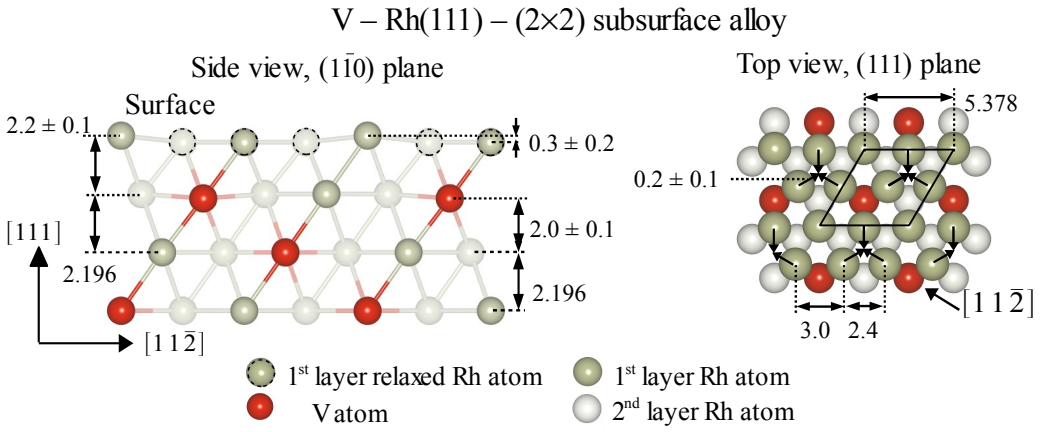

Fig. 4.25: Ball model of the V–Rh(111) subsurface alloy with the (2×2) surface reconstruction. The small arrows in the picture on the right indicate the direction of lateral displacement of the Rh surface atoms. The rhombus indicates surface unit cell. All lengths are given in Å.

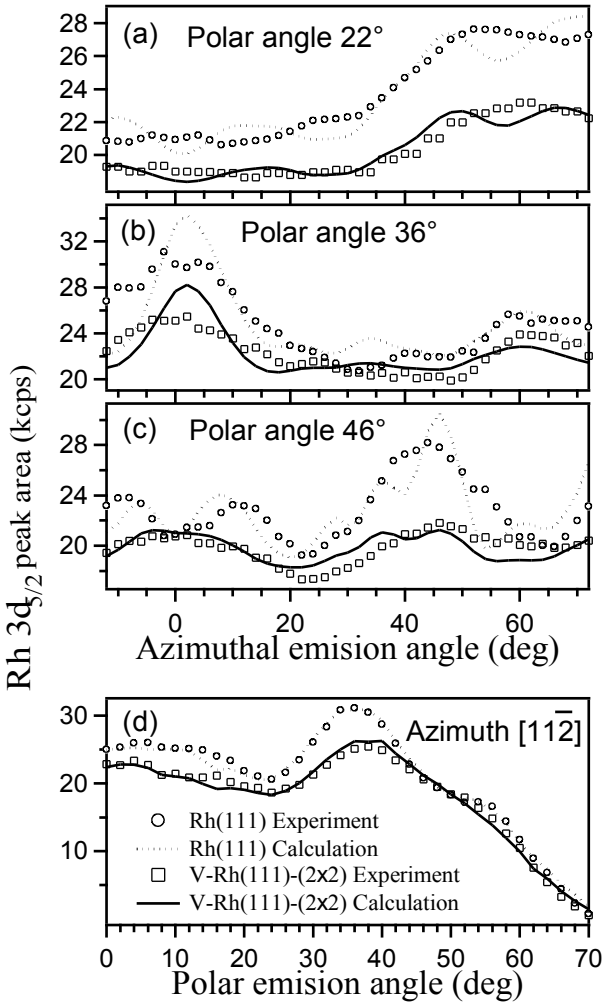

Fig. 4.26: Comparison of multiple-scattering cluster model simulations with experimental photoelectron diffraction in some azimuthal (a, b, c) and polar (d) angle emission scans of Rh $3d_{5/2}$ photoemission. Circles and squares represent raw experimental data from Rh(111) and V–Rh(111)–(2×2), respectively. Dotted lines are theoretical calculations for non-reconstructed Rh(111) surface and the solid lines are theoretical simulations for the V–Rh(111)–(2×2) structural model described in the text and in Fig. 4.25.

4.3.7 Valence band structure of V–Rh(111)–(2x2) subsurface alloy

The TPD spectroscopy at the V–Rh subsurface alloys showed a shift of the desorption peak maximum toward lower temperature by about 15–18 K as compared with the desorption peak from the clean Rh surface (see Sec. 4.3.4 , Fig. 4.15 and Sec. 4.2.4 , Fig. 4.8.) The high-resolution SRPES measurements of Rh 3d core level showed a shift in the surface component binding energy by +0.22 eV upon alloying with V (Sec. 4.3.3 , Table 4). These changes are in excellent agreement with the correlations noticed by Rodriguez and Goodman (See Introduction). On the other hand, no or only a small *d*-band shift to higher binding energies was observed in the valence band spectra. This observation indicates that the model proposed by Hammer et al. probably can not fully describe the mechanism of the CO adsorption on the V–Rh alloy. In order to get more insight into the bonding between CO molecules and the V–Rh alloy surface atoms, the valence band electronic structure was measured by means of angle-resolved UPS spectroscopy.

The ARUPS experiment was performed at the MSB beamline at Elettra synchrotron using photon energies of 35 and 55 eV. The valence band of pure Rh(111) was mapped and the influence of the CO adsorption on the valence band was measured as well. Then the V–Rh(111)–(2×2) subsurface alloy was prepared by the procedure described before. Again, the valence band structure of the surface was measured and the influence of CO adsorption was recorded.

At the used experimental parameters, the valence bands measured at the alloy were dominated by the photoemission from rhodium. On one hand, it was due to the no presence of the vanadium in the top most layer and the $L1_2$ structure of the Rh_3V alloy with the vanadium concentration of 25 at.% in subsurface layers. In addition, the relative photoemission cross-section for the valence Rh 4d is approximately 5-times higher than for the valence V 3d at 35 eV photon energy and more than twice at 55 eV photon energy (Fig. 2.5, Sec. 2.4).

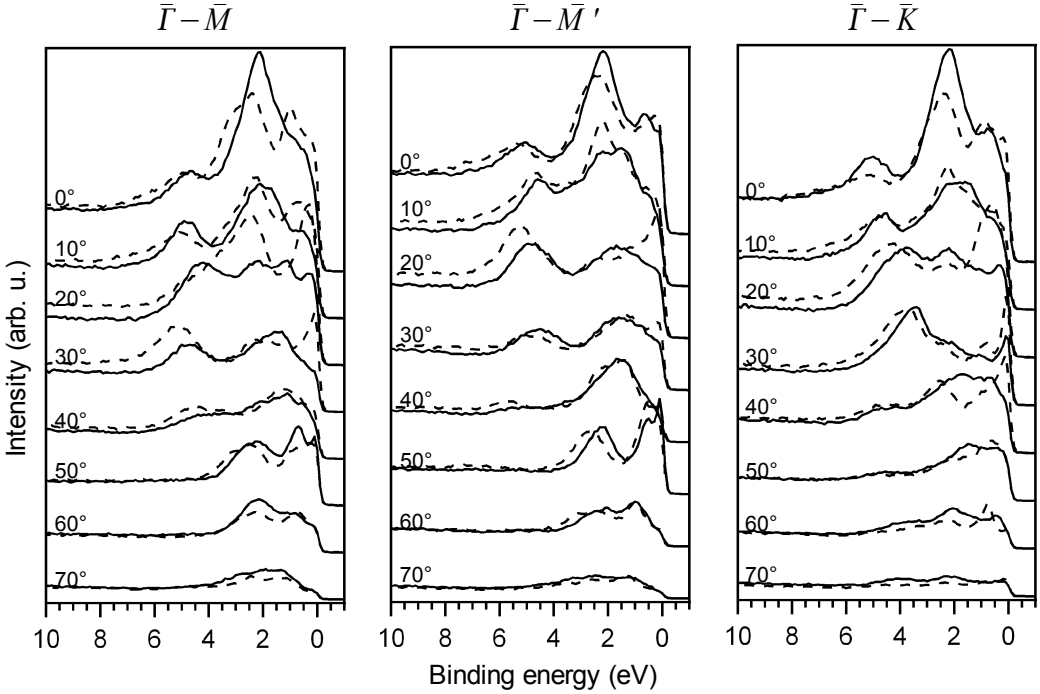

Fig. 4.27: Valence band spectra of the clean Rh(111) (dashed curves) and the V-Rh(111)-(2×2) alloy (solid lines) taken at different polar emission angles along directions $\bar{\Gamma}-\bar{M}$, $\bar{\Gamma}-\bar{M}'$, $\bar{\Gamma}-\bar{K}$ in SBZ (see Attachment). Spectra were obtained at a photon energy of 55 eV.

In Fig. 4.27 valence band spectra from Rh(111) and V–Rh(111)–(2×2), taken at several different emission angles, are compared. The alloying induced three general changes. The valence band became narrower, the intensities of peaks close to the Fermi level were significantly reduced and the peaks in the region 2-5 eV were shifted to lower binding energies.

By summing up the valence band spectra from sufficiently large solid angle, one gets the valence band spectrum averaged through a significant part of the Brillouin zone and the measured energy distribution is proportional to the joint density of states (Sec. 2.5). In Fig. 4.28, measured angle-integrated valence band (VB) spectra are shown together with theoretically calculated electron densities of states according to [76]. The theoretical calculations show *DOS* in the bulk and in the first four surface layers. Any direct comparison between the measured spectrum and theoretical *DOS* must be made with caution. The measured VB spectrum is proportional not only to the *DOS* of occupied states but also to the *DOS* of unoccupied states. Moreover, it depends on the matrix transition elements which affect the measured valence band intensity profile. This effect is clearly demonstrated by the different profiles of the

valence band measured at the two different photon energies (Fig. 4.28(a,b)). In addition, the IMFP of the photoelectrons from the valence band (~3-4 Å according to the TPP 2M formula [36]) is equivalent to the depth shorter than twice the Rh(111) interlayer distance (d_{111}^{Rh} = 2.2Å). It means that the measured valence band profile is the result of a weighted average from about 6 surface layers with the most significant contribution from the first two. This relatively high surface sensitivity can explain why the shape of the valence band of Rh(111) is rather similar to the theory. For instance, the maxima at 4.8 and 2.5 eV BE are in good agreement with the maxima predicted on the top-most layer. Moreover, the relatively high intensity near the Fermi level is also in good agreement with the theory, which shows increased density of states at the top layers in comparison with the bulk.

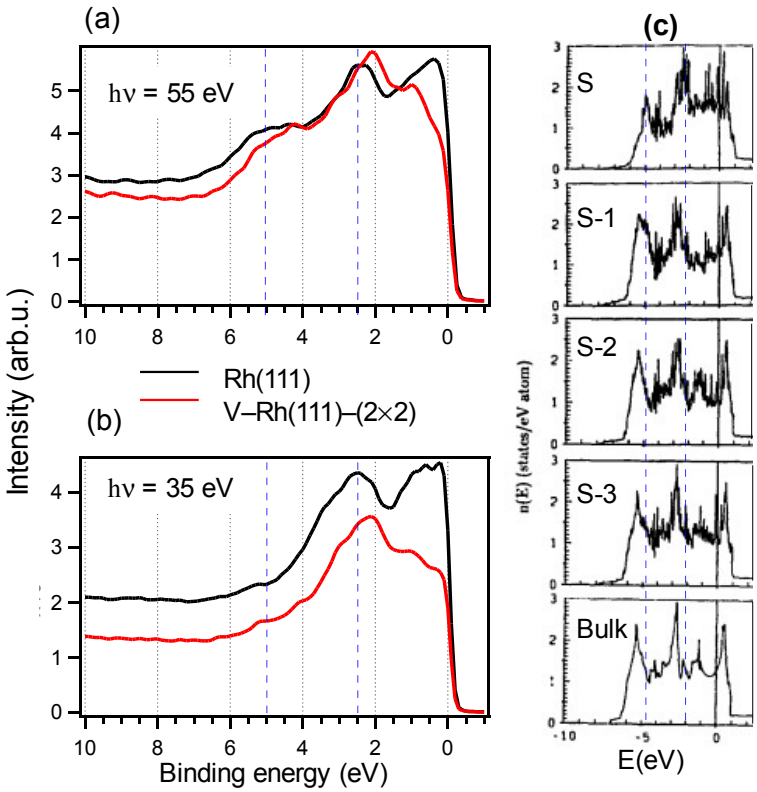

Fig. 4.28: Angle-integrated valence band spectra of clean Rh(111) and V-Rh(111)-(2×2) surface measured at a photon energy of (a) 55 eV and (b) 35 eV. (c) Calculated layer-resolved electronic densities of states in the first four top layers of Rh(111) and in the bulk. Taken from [76]. *The blue lines are guidelines for the comparison between measured valence bands and theoretical densities of occupied electronic states.*

What matters is the difference in the integrated valence band spectra between the clean Rh(111) and V–Rh(111)–(2×2) alloy. The same changes appeared on both spectra measured at two different photon energies. That indicates that the changes are related more likely to the change of the density of states than to matrix transition elements. The alloying induced a shift of the central peak maximum by about 0.3 eV to lower binding energy and simultaneously the density of states at the Fermi level was reduced noticeably. The centroids of the valence bands (between -1 and 6.5 eV) were slightly shifted to higher binding energy by about 0.01 eV and 0.02 eV, respectively. The shift of the centroids was rather small. According to the theory, which explains correlations between CO adsorption energy and valence band structure (see Introduction), the lower the CO adsorption energy, the larger the shift of the centroid to higher binding energy. The case of the V–Rh surface alloy is apparently different and further analysis is necessary to understand its somehow peculiar behaviour.

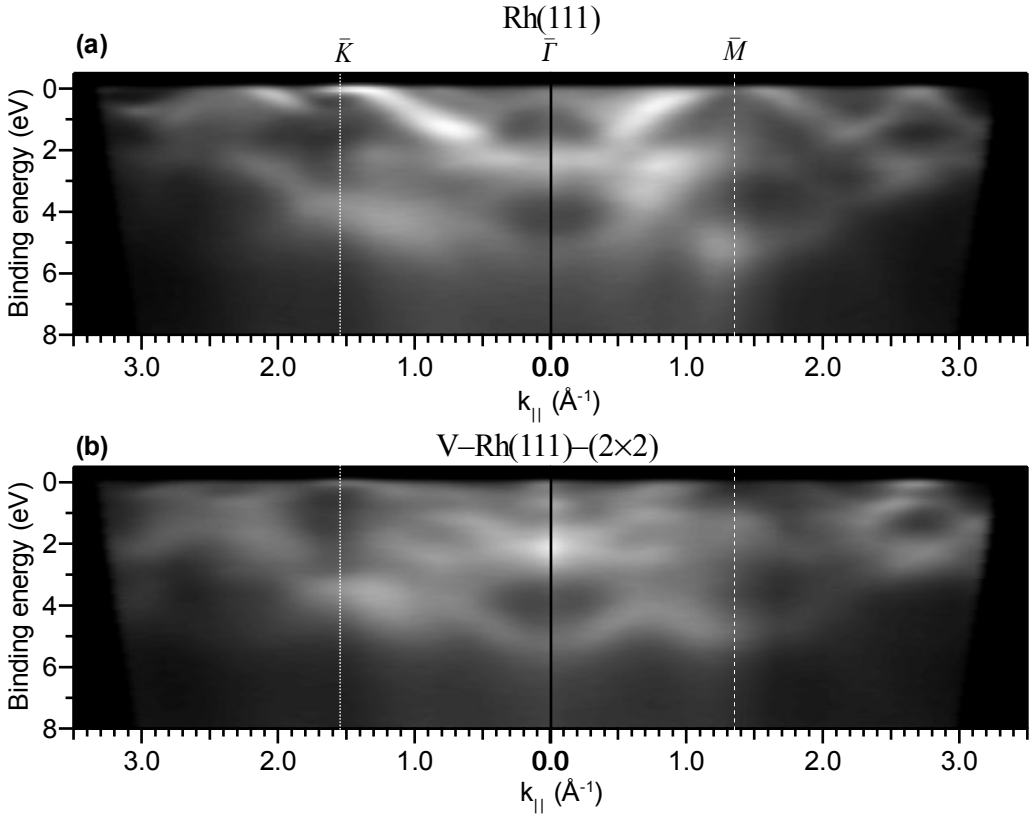

Fig. 4.29: Valence band maps of the (a) Rh(111) and (b) V–Rh(111)–(2×2) surfaces measured at a photon energy of 55 eV along the high-symmetry $\bar{\Gamma}-\bar{K}$ and $\bar{\Gamma}-\bar{M}$ directions.

From the measured EDC curves, valence band maps were created with the use of the transformation described in Sec. 2.5 . The valence band maps of the Rh(111) and V–Rh(111)–(2×2), measured at 55eV photon energy, are compared in Fig. 4.29. The valence bands measured under the given conditions are a mixture of surface and bulk states and detailed analysis is necessary to understand the electronic changes stimulated by subsurface alloy formation. Further understanding can be achieved by comparing them with theoretically calculated dispersion relations. According to the author's knowledge, the theoretical calculations for V–Rh(111) have not been reported yet. On the other hand, theoretical calculations of the ground state electronic structure of Rh(111) surface are available. There have been several theoretical approaches used to calculate and predict surface electronic structure of Rh single-crystal surfaces [76,89-92]. The most precise calculations are those of Eichler et al. [76,89], shown in Fig. 4.30. In the theoretical study, the structural and electronic properties of the Rh(111) surface were investigated by self-consistent *ab-initio* local-density-functional calculations. As for the electronic structure, authors calculated the electronic density of states, surface dispersion relations and charge-density distributions of some ground state surface states.

It is worthy to note, that the calculations have been done for the ground state, while the experimental electronic structure is influenced by final states of the photo-excited multi-electron system and selection rules of the photoemission process. Some surface states can be missing due to zero matrix element of the photoemission transition. On the contrary, some surface states can be missing in the theoretical prediction in consequence of the criterion chosen to distinguish surface states from bulk states. Any comparison between an ARUPS experiment and theoretical prediction of the ground-state electronic structure must be made cautiously and the both approaches should be considered as complementary.

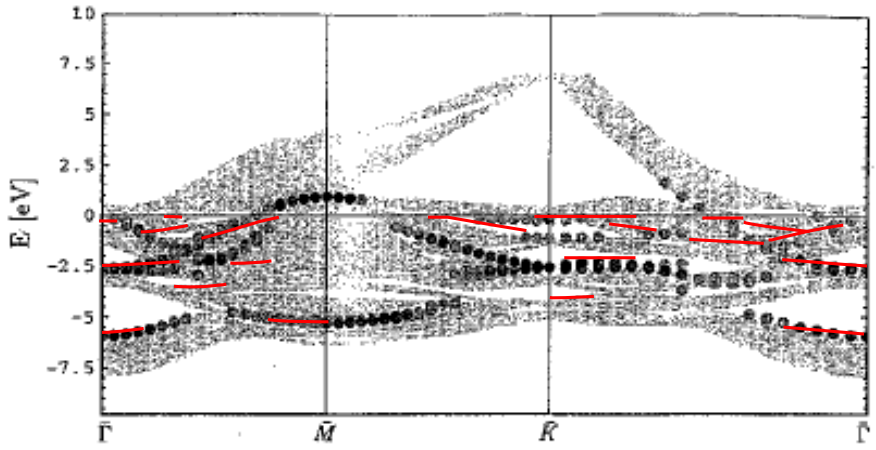

Fig. 4.30: Theoretical and experimental dispersion relations of electronic surface states on Rh(111). Surface states, calculated by A. Eichler et al. [89], are represented by black dots. Red dashed lines corresponds to surface states determined in this work. The projected band-structure of the bulk is shown by grey shaded areas.

The surface states or resonances presented in this work were identified by doing two experimental tests. First, the valence band spectra of the clean surfaces were measured at two different excitation photon energies (35 and 55 eV). Second, the surfaces were exposed to 10 L of CO gas dose, which results in a CO saturation adsorption at 300 K on a clean Rh(111) surface. After the CO saturation adsorption, the valence band spectra were measured again.

Due to the nature of surface states, photoemission from them is generally very sensitive to a modification of surface. Adsorption of gas molecules on surface often quench the surface photoemission features or shift them in binding energy. Carbon monoxide molecules strongly quench the Rh(111) surface features as it was already observed on the Rh $3d_{5/2}$ spectrum surface component shown in Fig. 4.12, in Sec. 4.3.4 .

Thus, the valence band maps measured before and after the exposure to CO were compared and a significant decrease in the intensity after the CO adsorption indicated surface character of the corresponding valence band peaks. However, some bulk features can also exhibit sensitivity to surface modification. Therefore, another test to identify the surface states was done.

The other test was based on a comparison between the valence band measured at the two different photon energies. Dependence of the binding energy of the electronic bands on the momentum normal to the surface was checked. Due to the two-

dimensional character of surface features they should display none or just a little dispersion with $k_{\perp}$. In other words, the peak positions of surface states in the valence band maps projected to the surface Brillouin zone (SBZ) should be the same at the both photon energies.

This method used to identify surface states has, however, limitations. In some cases, surface states are not distinguished in this way. There might be low matrix element of the transition or strong overlap between surface and bulk states.

The valence band maps of Rh(111) and V–Rh(111)–(2×2) along the $\bar{\Gamma}-\bar{M}$ and $\bar{\Gamma}-\bar{K}$ directions are compared in Figures 4.31 and 4.32. In each of the figures, the first row corresponds to the valence bands measured at 55 eV photon energy. As far as the grey colour scale is concerned, it is the same for both surfaces and dark colours correspond to low intensities, while bright colours to high intensities. The same applies for the third row, where valence band maps obtained at 35 eV photon energy are displayed. The images in the second and fourth row are result of the subtraction of the VB maps measured after the CO adsorption from those before the adsorption. The bright colours in these images indicate states which were quenched by the CO adsorption. The brighter the colour is the stronger decrease in the intensity after the CO adsorption appeared. The dashed lines in the figures highlight bands of surface states determined as outlined above.

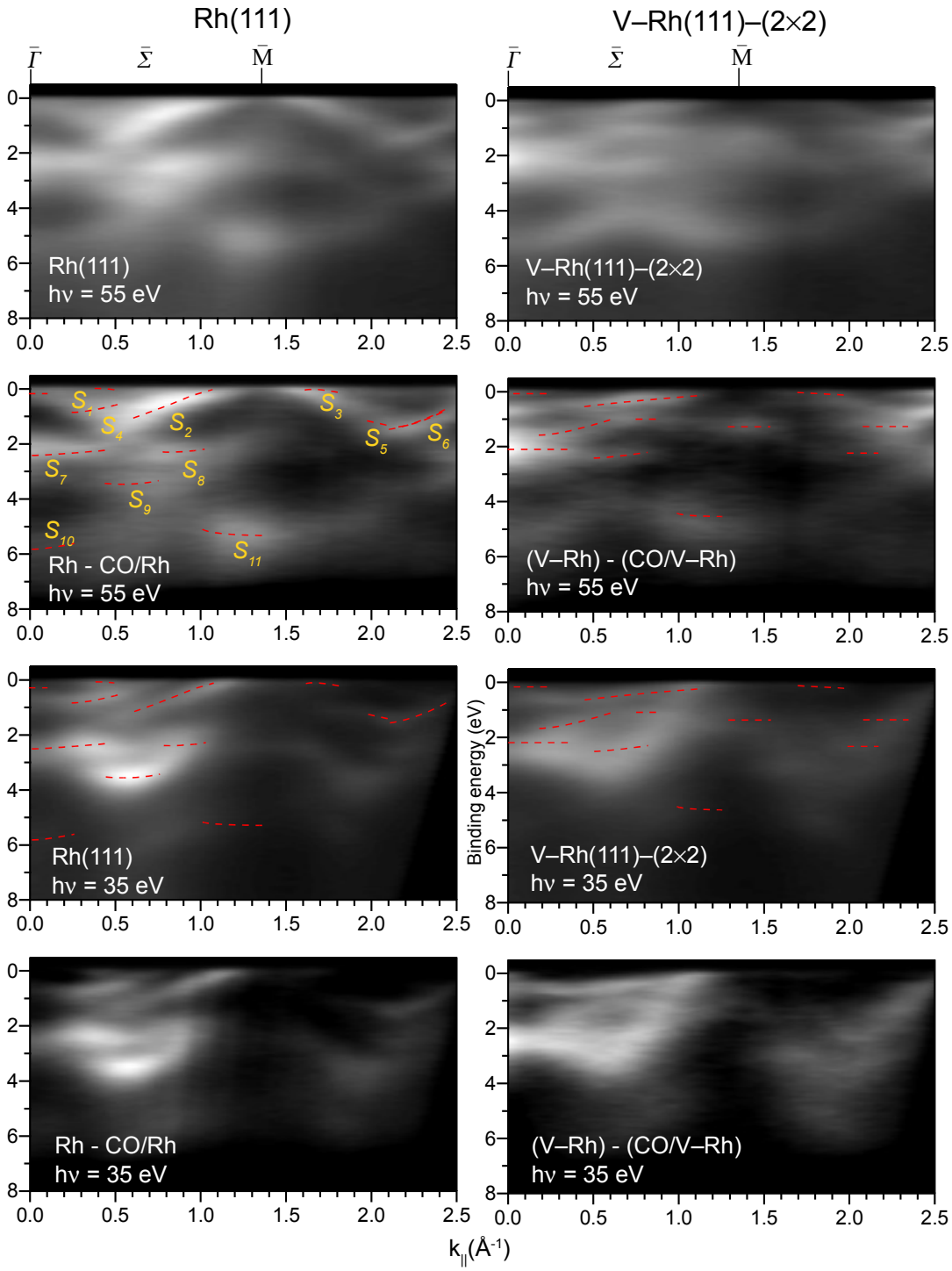

Fig. 4.31: Valence band maps of the Rh(111) and V–Rh(111)–(2×2) surface as a function of $\boldsymbol{k}_{||}$ in $\bar{\Gamma}-\bar{M}$ direction. The images in the second and fourth row were obtained by subtraction of the VB maps after the CO adsorption from those before the adsorption. The red lines mark surface states.

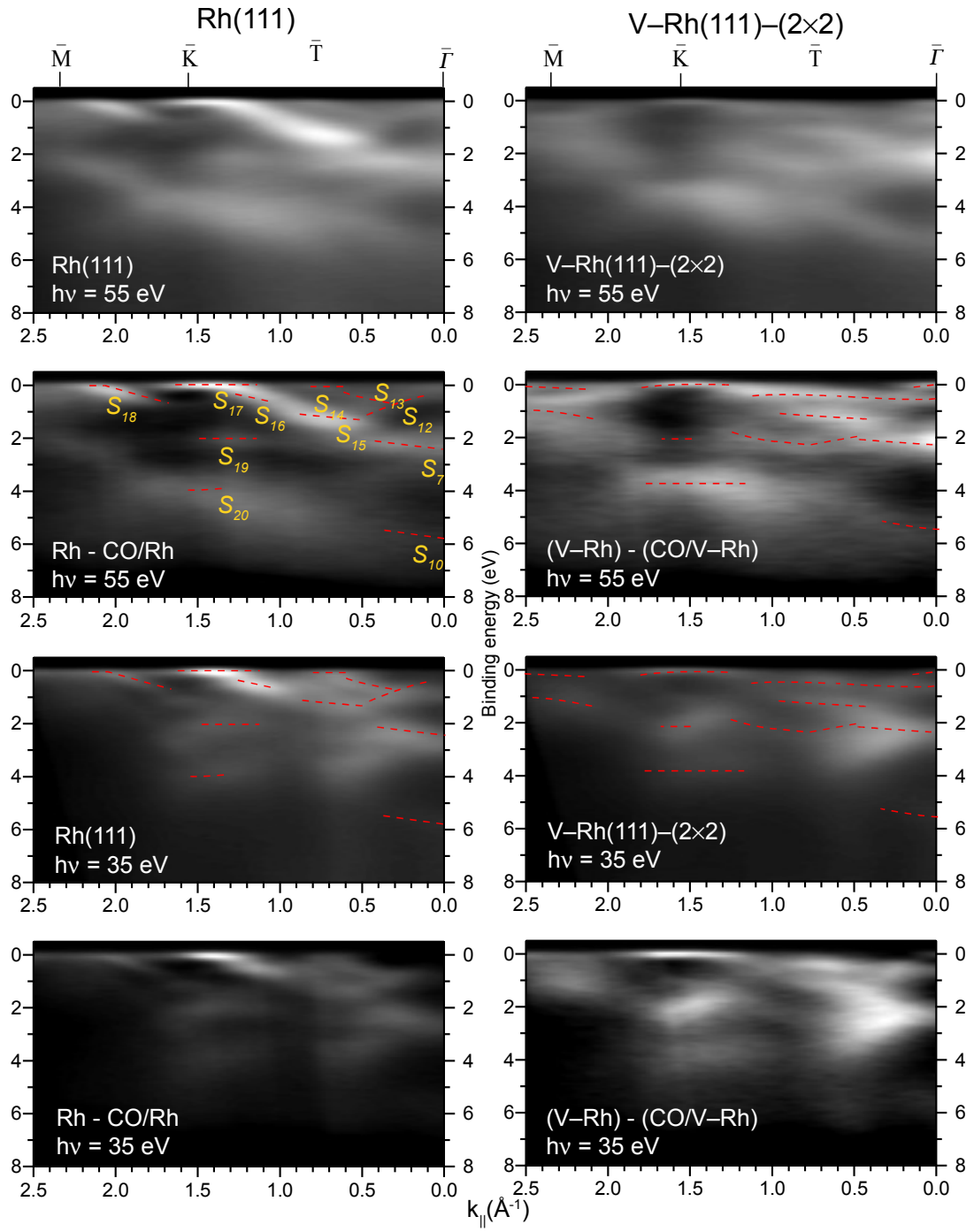

Fig. 4.32: Valence band maps of the Rh(111) and V–Rh(111)–(2×2) surface as a function of $\boldsymbol{k}_{||}$ in $\bar{\Gamma}-\bar{M}$ direction. The images in the second and fourth row were obtained by subtraction of the VB maps after the CO adsorption from those before the adsorption. The red lines mark surface states.

The surface state bands identified on Rh(111) in this work are in rather good agreement with the previous experimental measurements published in [93], as shown in Fig. 4.33. The origin of the differences between the two experimentally determined surface dispersion relations are, most probably, due to the different

photon energies and adsorbing molecules. While Wei et al [93] used photon energies 24, 32, 42 and 60 eV and H_2 adsorption, energies 35 and 50 eV and CO adsorption were employed in this work. Another difference was in the energy and angular resolution (120 meV, 1° in [93], 200 meV, 2° in this work).

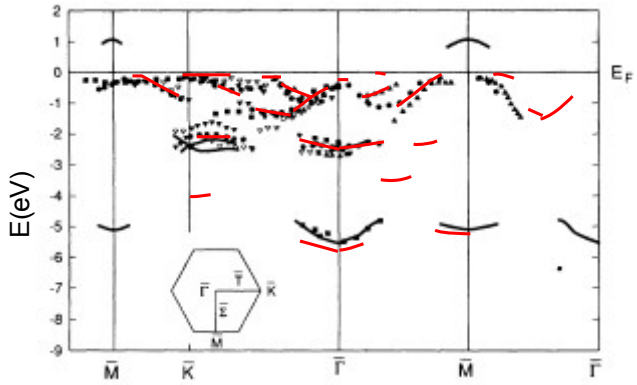

Fig. 4.33: Surface states on Rh(111) determined experimentally by Wei et al. [93] (dots) compared to the theoretical results of J. Feibelman [90] (solid curves). The red curves correspond to the dispersion relations determined in this work.

Quite a good agreement was found also between the measured surface state bands and the theoretical predictions of Eichler et al. [89], as already shown in Fig. 4.30. Three filled states at $\bar{\Gamma}$ point at binding energies 5.9, 3.2, and 2.6 eV were predicted by the theory. An evidence of a surface state at a BE of 5.8±0.2 eV was found in this work. The dispersion relation of the correspondent surface band is marked as band S_{10} in Fig. 4.31. Similarly, the band S_7 corresponds to the surface state band predicted at a BE of 2.6 eV at $\bar{\Gamma}$ point. Our measurements gave a value of 2.5±0.2 eV. There are also signs of surface states at 3.2 eV BE but the experimental evidence is not unambiguous in this case. Other strong surface states were predicted at $\bar{M}$ point. An empty surface state at 0.9 eV above the Fermi level and a filled surface state at 4.8 eV BE were predicted by the theory. Despite the fact that empty states are not accessible to ARUPS technique, the empty state at the $\bar{M}$ point can be extrapolated from the band S_2, which intersects the Fermi level before the $\bar{M}$ point. According to the *ab-initio* calculations [89], the empty states around the $\bar{M}$ point show anti-bonding character. The spacial charge-density distribution of the anti-bonding states is sticking out the surface plane and therefore they are expected to play an important role in surface reactions. Indeed, they are strongly quenched after the CO adsorption,

which is the result of charge donation from the *d*-band to the empty $2\pi^*$ molecular orbital, the lowest unoccupied molecular orbital (LUMO) of the CO molecule. As far as the states at the lower BE at the $\bar{M}$ point is concerned, there is a noticeable quenching by CO adsorption observed at 5.3±0.5 eV BE in the VB measured at 55 eV photon energy (band S_{11}). The quenching of the states at the same BE, measured also at 35 eV photon energy (Fig. 4.34), confirms the surface character of these states.

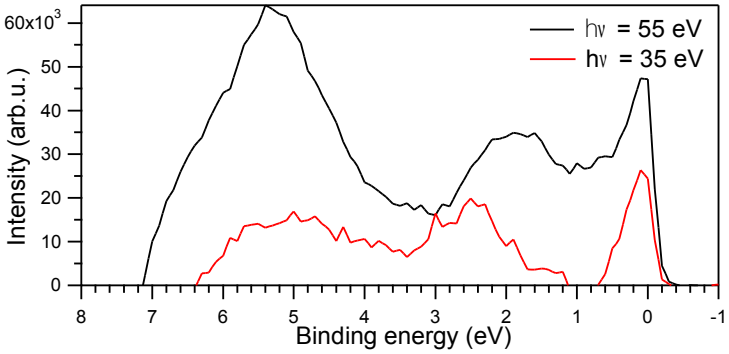

Fig. 4.34: Difference VB spectra at Rh(111) at $\bar{M}$ point measured in the $\bar{\Sigma}$ azimuth in the SBZ. The difference spectra were obtained by subtracting the VB spectra measured after the CO adsorption from those before the adsorption.

At the $\bar{K}$-point, four occupied surface states at 4.1, 2.6, 1.1 and 0.2 eV binding energy have been predicted [76]. Clear experimental evidence of surfaces states was found at 0.05 ± 0.05 eV, 2.1 ± 0.2 eV and 4.0 ± 0.3 eV binding energies (Fig. 4.35). Surface character also exhibited the states in bands S_{14}–S_{17} in the $\bar{\Gamma}-\bar{K}$ direction (Fig. 4.32). Strong decrease of their intensity after the CO adsorption indicates their contribution to the CO 2π* backbonding.

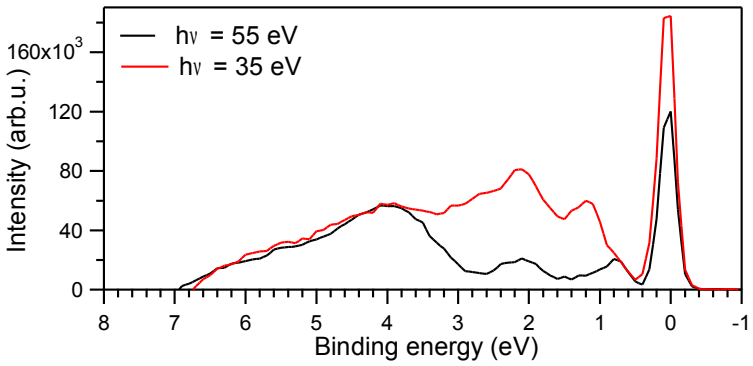

Fig. 4.35: Difference VB spectra at Rh(111) at the $\bar{K}$ point measured in the $\bar{\Gamma}$ azimuth in the SBZ. The difference spectra were obtained by subtracting the VB spectra measured after the CO adsorption from those before the adsorption.

Despite the calculated dispersion relations generally provide a good match to the experimental results of this work, some experimental bands do not span as far as predicted. One of the reasons might be the dependence of the matrix transition elements on the sample position orientation (the sample was rotated during the ARUPS measurements and the incident radiation was linearly polarised), which can hinder the photoemission transition from surface states. On the other hand, a few surface bands, determined experimentally, were not marked in the calculated dispersion relations. The reason might be simply in the criteria which were applied to distinguish surface bands.

The formation of the V–Rh(111)–(2×2) subsurface alloy induced significant changes in the valence band electronic structure as can be seen in figures 4.31 and 4.32. When comparing the surface bands of the Rh(111) with the V–Rh(111)–(2×2) surface, one can see that some of them disappeared or were significantly quenched (such as band S_9 in $\bar{\Gamma}-\bar{M}$ direction or $S_{15}-S_{18}$ in $\bar{\Gamma}-\bar{K}$ direction), some of them noticeably changed their dispersion relations (S_2 in $\bar{\Gamma}-\bar{M}$ direction), others were slightly shifted in binding energy (S_7, S_{11}) and some new surface states appeared. The most pronounced changes concern bands S_7 ($\bar{\Gamma}$), S_2 ($\bar{\Gamma}-\bar{M}$) and $S_{15}-S_{18}$ ($\bar{\Gamma}-\bar{K}$). While the bands S_2, $S_{14}-S_{17}$ were dominant features at the clean Rh(111) surface, they almost disappeared at the alloy surface. On the contrary, the intensity of the band S_7 increased at the alloy surface and the whole band was slightly shifted to lower binding energies ((Fig. 4.36(a), Table 5). The largest changes in the $\bar{\Gamma}-\bar{M}$

direction overcame S_2 band. The strong quenching of the states of the S_2 band upon CO adsorption (Fig. 4.36(b)) indicates the donation of the electric charge into the LUMO of CO, exactly is it was observed at the clear Rh(111) surface. Therefore, it is likely that it is the same surface state band but with different dispersion relation and most probably with significantly decreased density of states at the alloy surface. This decrease of the charge available for the hybridisation and mixing with the CO $2\pi^*$ orbital might be the reason of the observed weaker CO molecular bond with Rh surface atoms. The same can be assumed in the case of some others surface states, for instance, in bands S_3,, $S_{15} - S_{18}$ which intensity was significantly reduced upon the alloying with vanadium and which apparently contributed to the π backdonation. The interaction of these states with CO molecules as well as the influence of vanadium is demonstrated in (Fig. 4.36(c)) on the band below the Fermi level at the $\bar{K}$ point.

The estimated binding energies of the surface states at the high symmetry points of the SBZ are summarized in Table 5 and compared with theoretically predicted values for clean Rh(111).

$\bar{\Gamma}$			$\bar{M}$			$\bar{K}$		
Theory	Rh(111)	V–Rh	Theory	Rh(111)	V–Rh	Theory	Rh(111)	V–Rh
–	–	0.05±0.05	–	0.05±0.05	0.05±0.05	0.2	0.05±0.05	0.05±0.05
–	–	0.6±0.1	–	–	1.2 ± 0.2	1.1	–	–
2.6	2.5± 0.2	2.3±0.2	4.8	5.3± 0.5	–	2.6	2.1±0.2	2.1±0.2
3.2	–	–				4.1	4.0±0.2	3.7±0.3
5.9	5.8 ± 0.2	5.6 ±0.4						

Table 5: Binding energies of the surface states at high symmetry points of the Rh(111) SBZ. The theoretical values, taken from [76]*, concerns pure Rh(111) surface. The binding energies are given in eV units.*

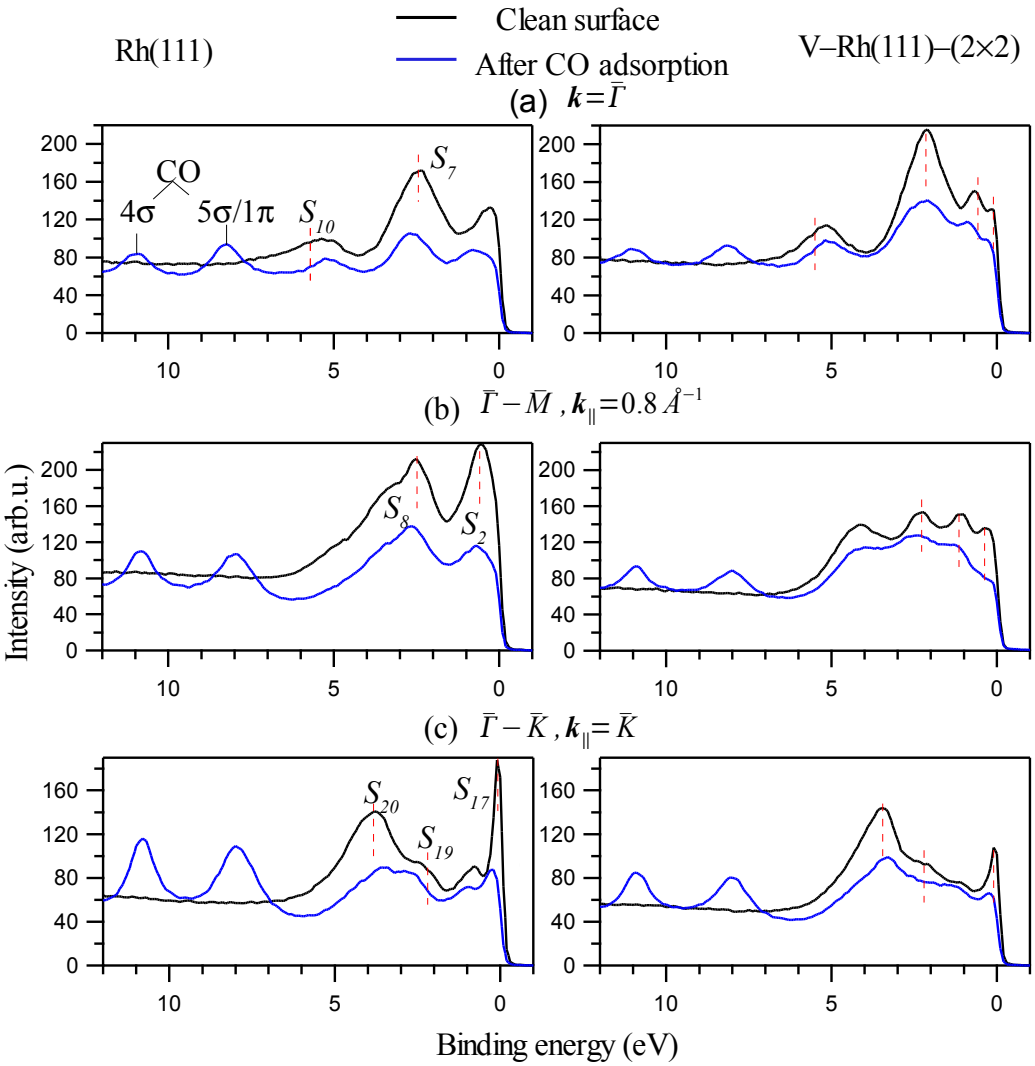

Fig. 4.36: Comparison between VB spectra of the pure Rh(111) (on the left) and V–Rh(111)–(2×2) subsurface alloy (on the right) at some k-points of the SBZ before (black curves) and after the CO adsorption (blue curves). The red dashed lines mark surface states. Spectra were measured at 55 eV photon energy.

In summary, the high-resolution ARUPS measurement at the clean and CO covered Rh(111) surface proofed to be very sensitive to surface states within the chosen experimental parameters. The dispersion relations of the surface states measured at Rh(111) are in good agreement with theoretical predictions. The pronounced decrease of their intensity after the CO adsorption indicates charge transfer from the surface states to the hybridized and mixed bonds with LUMO orbital of adsorbed CO molecules. The surface states, most influenced by CO adsorption, were those close to the Fermi level in a BE range of 0-2 eV. That indicates that their hybridization with CO LUMO orbital represents an important

contribution to the CO-metal bond strength. The DFT study of Eichler et al. gave evidence of anti-bonding character of those states and charge-density distribution spanning out of the surface plane. That rationalizes the interaction with CO molecules observed at valence band spectra. It also indicates that the depletion of their density and alternation of their dispersion relations upon alloying with vanadium is the main reason of the decreased adsorption energy of the CO molecules on the metal surface. Despite the overall centre-of-mass of the valence band was not shifted to higher binding energies, the density of states close to the Fermi level was reduced significantly and hence the CO-metal surface bond was reduced. The V–Rh(111) subsurface alloy is an example of the bimetallic system where the shift of the valence band centre is not correlated with the CO adsorption energy.

A similar correlations between CO adsorption and the electronic structure, which can not be described by standard model of Hammer, were predicted also for V-Pd(111) surface and subsurface alloys, i.e. for a system which is, by its composition and structure, very close to here studied V–Rh(111) alloy. A detailed theoretical study of the V–Pd(111) alloys have been done by Hirschl and Hafner [25,26]. The theoretical study confirmed the poisoning effect of the vanadium impurity on the CO adsorption, which was confirmed also experimentally on V–Pd(111)–$(\sqrt{3}\times\sqrt{3})R30°$ subsurface alloy [24]. Moreover, it also showed that the model of Hammer is not fully applicable for the Pd–V alloys due to the strong local influence of the vanadium dopant. The influence of a vanadium impurity decreased rapidly with distance. The formation of the V–Pd surface and subsurface alloys caused shifts in the *d*-band of neighbouring Pd atoms towards higher BE, which is qualitatively in agreement with the model of Hammer. However, it turned out that the *d*-band position alone allows no predictions of the CO adsorption energy. Orbital-resolved analysis of the *d*-band density of states lead to a conclusion that vanadium dopant affects mainly those *d*-orbitals which are pointing in its direction. We can assume a similar *d*-*d* hybridization between the subsurface vanadium and surface Rh atoms. The hybridisation is accompanied by a localization of the Rh valence *d*-band electrons to the bimetallic bond with V in the second layer which resulted in the reduction of the density of states at the surface.

On the other hand, some surface states remained on the V–Rh(111) subsurface alloy, they were shifted to lower binding energies and their intensity even increased.

In the frame of the theoretical model of Hammer, such changes yield to a stronger CO-metal bond. This might explain why the decrease of the CO-Rh surface bond strength is no so high as that of CO-Pd surface modified by subsurface vanadium.

Apart from the reduced interaction with CO molecules, the reduction of states observed at the top of the *d*-band is also in a correlation with the surface atomic reconstruction. The detailed theoretical study of the Rh (111), (100), and (110) surfaces [76] showed that the inward relaxation of the top layer (-1.7±0.2, -3.8±0.2, and 9.8±0.6 %) is caused by the de-population of the anti-bonding states at the top of the *d*-band. The formation of the V–Rh(111)–(2×2) subsurface alloy was accompanied by a pronounced depopulation of the anti-bonding states at the Rh(111) surface which explains the inward relaxation of the top layer by 14 ± 9 % determined from the XPD measurements.

4.3.8 Conclusions

The photoemission from the V 2p and Rh $3d_{5/2}$ core levels showed that the deposition of 0.4 ML of V at 823 K results in the formation of V–Rh subsurface alloy. This result was expected, since diffusion of V into Rh subsurface region was observed on the polycrystalline Rh (Sec. 4.2) under similar experimental conditions. The formation of a subsurface alloy on Rh(111) crystal was already observed at 0.3 ML of V [21,30,31] deposited at a substrate temperature of 823 K. In the present work, it was showed that the deposition of a higher amount of V (2.5 ML) at the same temperature and further annealing also lead to the formation of the subsurface alloy. Our observations indicate that both alloys with 0.4 and 2.5 ML of V exhibit very similar electronic structure and CO and O_2 adsorption properties. Decrease of the Rh $3d_{5/2}$ intensity indicates the atomic concentration of V in the subsurface region was 22– 28%. Electron diffraction measurements showed that the formation of the (2×2) structure is favoured under the used experimental conditions. The obtained results indicate formation of alloy with Rh_3V composition and $L1_2$-type structure ordering. Since RhV ordered bulk alloy is predicted as the most stable phase, Rh_3V subsurface alloy is an example of the influence of the presence of surface on metal mixing.

CO adsorption on the subsurface alloy surfaces confirmed that there was no vanadium on the surface, otherwise formation of vanadium oxides and carbides

would be observed after the exposure to CO gas [6,31]. The subsurface vanadium influences CO adsorption indirectly, however, through the interaction with rhodium. The adsorption capacity of the surface decreased and the adsorption in three-fold hollow sites was suppressed more than in on-top sites. The CO-metal surface bond was weakened. Carbon monoxide desorption peak profile was changed, as well. Thermo-desorption of CO indicates changed intermolecular interaction, surface diffusion barriers and appearance of new adsorption positions for weakly bounded CO molecules. The new adsorption site is probably connected with the surface reconstruction. According to the reconstruction derived from the photoemission diffraction (Fig. 4.25), there are two different on-top sites and several hollow and bridge sites, with or without V as the next-nearest neighbour.

Detailed valence band measurements, which were very sensitive to surface states, showed that the valence electrons in the states near the Fermi level are participating in the bond between the metal surface and adsorbed CO molecules. A strong depletion of these states was observed upon the alloying, which can explain the weakening of the CO-metal surface bond and lower CO adsorption capacity of the V–Rh alloy surface.

When comparing TPD from the V–Rh(111) model system (Fig. 4.15) and from the Rh/V/γ-Al_2O_3 sample (Fig. 4.2(c)), one can see, in a temperature range up to 550 K, very similar changes at the bimetallic surfaces as compared with pure Rh surfaces. Thus, it can be assumed that the same electronic effects are responsible for the altered chemisorption properties on both V–Rh(111) alloy and mixed Rh/V supported layer. On the other hand, no evidence for CO dissociation on the studied V–Rh(111) subsurface alloy was found under the used experimental conditions. The CO dissociation would be manifested in C 1s signal at lower binding energies. This indicates that the increased CO dissociation, which was observed on the non-continuous thin Rh–V layers supported by γ-Al_2O_3, was not a result of an electronic effect but more likely due to an altered morphology or amount of step and kink sites on the bimetallic particles as compared with pure Rh layer on the same substrate.

While no direct interaction between the adsorbed CO molecules and subsurface vanadium was observed, a considerable interaction between the vanadium and adsorbed oxygen occurred. The second vanadium state observed at ~515 eV BE indicates formation of an ultra-thin vanadium oxide on the alloy surface. That means

vanadium surface segregation induced by adsorbed oxygen already at a low temperature of 300 K.

4.4 V on Rh(110)

4.4.1 Introduction

It has been outlined in Sec. 1.1 that real heterogeneous catalysts have typically a shape of small nanoparticles terminated by low-index planes. Therefore, properties of V–Rh(110) bimetallic system were investigated.

The second well defined model bimetallic system was prepared by V vacuum vapour deposition on Rh(110) single-crystal substrate. Similarly as in the case of Rh(111) substrate it was desirable to obtain an ordered alloy in order to apply integral methods such as ARUPS.

Among the low index surfaces at fcc structure, the (110) surface belongs to the most opened surfaces with coordination number 7 (compare with 9 on (111) surface). The presence of surface brings conditions which might lead to unexpected alloy structures, such as Rh_3V $L1_2$ structure observed on the Rh(111) surface. Different conditions at the Rh(110) surface might lead to new structures and reconstructions. Indeed, such unexpected reconstruction was observed as will be shown further.

Based on the experience with V–Rh(111) system, 2 ML of V were evaporated onto Rh(110) at a substrate temperature of 823 K. The sample was further annealed until a (2×1) reconstruction appeared. Annealing at even higher temperature induced (1×2) missing-row reconstruction. In the following chapters, the atomic structure is investigated by means of LEES, XPD and STM. Tentative models of the alloys and surface reconstructions are given. Study of the electronic structure by means of SRPES is following. Valence band structure of the alloy with (1×2) missing-row reconstruction was mapped. In the end, adsorption of CO on the surface with the missing-row reconstruction was investigated by means of SRPES.

4.4.2 Experimental

Photoemission measurements were performed at the MSB beamline at Elettra synchrotron and STM measurements on the home-built STM facility at the Department of Surface and Plasma Science in Prague.

The Rh(110) substrate from MaTecK, GmbH (99.9% purity) was cleaned by 1–2

keV Ar^+–ion sputtering, followed by annealing and heating in O_2 at 973 K for several minutes. The procedure was followed by annealing in vacuum at 1123–1273 K. The cleaning cycle was repeated several times. The cleanliness and quality of the Rh(110) surface was checked by Al Kα x-ray photoemission and LEED.

Two monolayers of vanadium were evaporated onto the clean Rh(110) surface while keeping the substrate at a constant temperature of 823 K during the deposition. Vanadium metal was evaporated from a cell using a principle of high energy electrons bombardment of a vanadium wire of a 99.8% purity. The residual gas pressure during the evaporation was about 3×10^{-7} Pa. After the V deposition, the sample was annealed at 973 K for 20 minutes and later at 1073 K for 10 minutes. In order to reduce the adsorption from the residual atmosphere, the sample was being flashed to 873 K if necessary. The same sample preparation procedure was performed in the both experimental UHV systems. The STM system was equipped with a quartz crystal microbalance to calibrate the V evaporation rate. The rate was determined to be 0.36 ML/min, where 1 ML of V contains the same number of atoms as one the Rh(110) plane, i.e. 0.979×10^{19} atoms/m^2.

The core-level photoemission spectra, measured at the MSB, were collected in normal emission geometry. Photon energies 380 and 651 eV were employed to excite Rh 3d, C 1s and V 2p, O 1s core levels, respectively.

Valence bands were mapped by means of angle-resolved UPS spectroscopy at the MSB with the same experimental setup as was used for Rh(111) single crystal (Sec. 4.3.2) by rotating the sample holder around two axes. The polar angle θ between the surface normal and the direction of detected photoelectrons was changed from 0 to 70° in the plane determined by the beamline and analyser axis. The azimuthal angle rotation was done in the range over 90°. Photon energies 35 and 55 eV were used. The acceptance angle of the analyser was 4° and the instrument energy resolution was about 200 meV. The obtained ARUPS curves were transformed into the valence band maps $I(E_i, \boldsymbol{k}_{\|})$ with the photoemission intensity I as a function of the initial state energy E_i and the surface parallel wave vector of the initial state $\boldsymbol{k}_{\|}$. The initial state energy E_i of an electron in the valence band was determined using Eq.(19), the correspondent surface parallel wave vector of the initial state from Eq.(21).The kinetic energy of the electrons outgoing from the Rh(110) surface was calculated using a sample work function W=4.96 eV [94].

XPD measurements performed at the MSB beamline were done with Al Kα x-rays source.

At the MSB, the samples were exposed to CO at a partial pressure of 2.7×10^{-6} Pa and a substrate temperature of 300 K. The CO dose was 10 L, what is sufficient to achieve a saturation coverage at clean Rh(110) [95,96].

4.4.3 Atomic structure and composition

Vanadium was evaporated onto the clean Rh(110) substrate in the same manner as it was done on the Rh(111) substrate when the V–Rh(111)–(2×2) subsurface alloy was formed. Two monolayers of V were evaporated onto Rh(110) while keeping the substrate temperature at 823 K. Subsequent vacuum annealing at elevated temperatures resulted in surface structures with LEED patterns shown in Fig. 4.37.

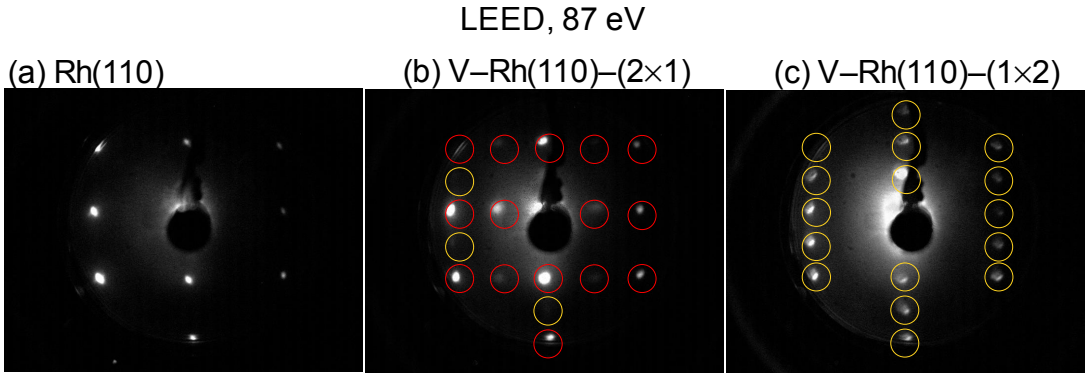

Fig. 4.37: LEED patterns observed on (a) the clean Rh(110) surface; (b) after the V depostion onto the Rh substrate at 823 K and annealing at 973 K; (c) after annealing at 1073 K. Red circles mark diffraction spots corresponding to (2×1), yellow to (1×2) surface reconstructions. The LEED patterns were obtained by electrons with a kinetic energy of 87 eV.

The annealing at a temperature of 973 K resulted in a LEED pattern with strong (2×1) and faint (1×2) diffraction spots (Fig. 4.37(b)). Further annealing at 1073 K created a LEED pattern correspondent to (1×2) surface superlattice only (Fig. 4.37(c)). It was proofed in previous chapters that under the used experimental conditions, vanadium is diffusing into rhodium and forms a subsurface alloy with V located in subsurface layers. Deposition of 2.5 ML on Rh(111) substrate at an elevated temperature of 823 K and subsequent annealing at 973 K leads to the formation of V–Rh(111)–(2×2) subsurface alloy with Rh_3V composition and $L1_2$ structure (Sec. 4.3.6). The similar ordered alloy formation could be expected also on

the Rh(110) surface. Such alloy would explain the (2×1) surface structure observed by LEED. Every second (110) plane in Rh_3V alloy contains 50% of vanadium atoms ordered in (2×1) superlattice with [001] rows of vanadium atoms separated by [001] rows of Rh atoms (see Fig. 4.38).

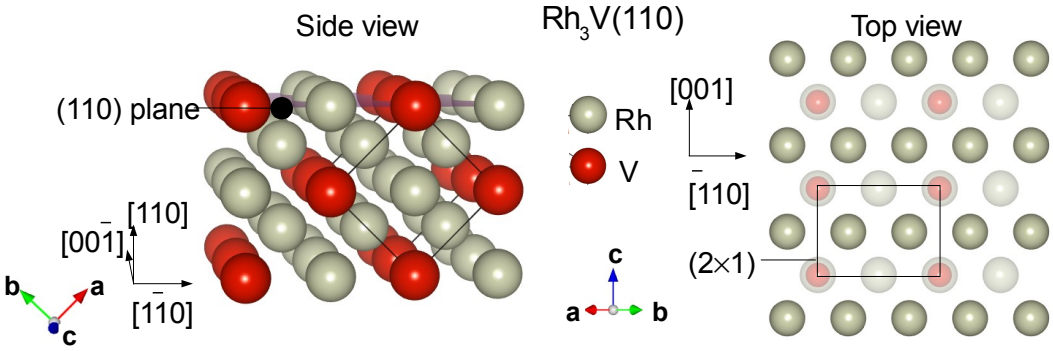

Fig. 4.38: Ball model of Rh_3V alloy with $L1_2$ structure and (110) surface termination.

The formation of a substitutional V–Rh(110) alloy was confirmed by X-ray photoelectron diffraction. After the formation of the V–Rh(110)–(1×2) alloy, XPD in azimuths $[\bar{1}10]$, $[\bar{1}12]$ was measured. Employing Al Kα radiation the electrons emitted from Rh $3d_{5/2}$ and V $2p_{3/2}$ core levels have the kinetic energy of 1179 and 974 eV, respectively. At such high kinetic energies, a forward-scattering on nearest and next-nearest neighbours is significant [42,97], which enables to obtain some information about the local atomic structure directly. The XPD curves from the V–Rh(110)–(1×2) taken along azimuth $[\bar{1}10]$ and $[\bar{1}12]$ are displayed in Fig. 4.39. The integrated intensities of the Rh $3d_{5/2}$ and V $2p_{3/2}$ peaks are displayed as a function of polar emission angle. In both rhodium and vanadium XPD curves, strong diffraction maxima were observed near the [010] (Fig. 4.39(a)) and [011] (Fig. 4.39(b)) direction. The diffraction maxima along this directions are expected for ideal undistorted fcc structure with the (110) surface plane as is depicted in Fig. 4.39(c,d). The small discrepancies between the positions of the observed and expected diffraction peaks could have the origin in surface relaxation and reconstruction. Nevertheless, the similarity between the XPD curves from rhodium and vanadium is a clear evidence of a V–Rh(110) alloy with V atoms in substitutional positions in the Rh fcc crystal lattice.

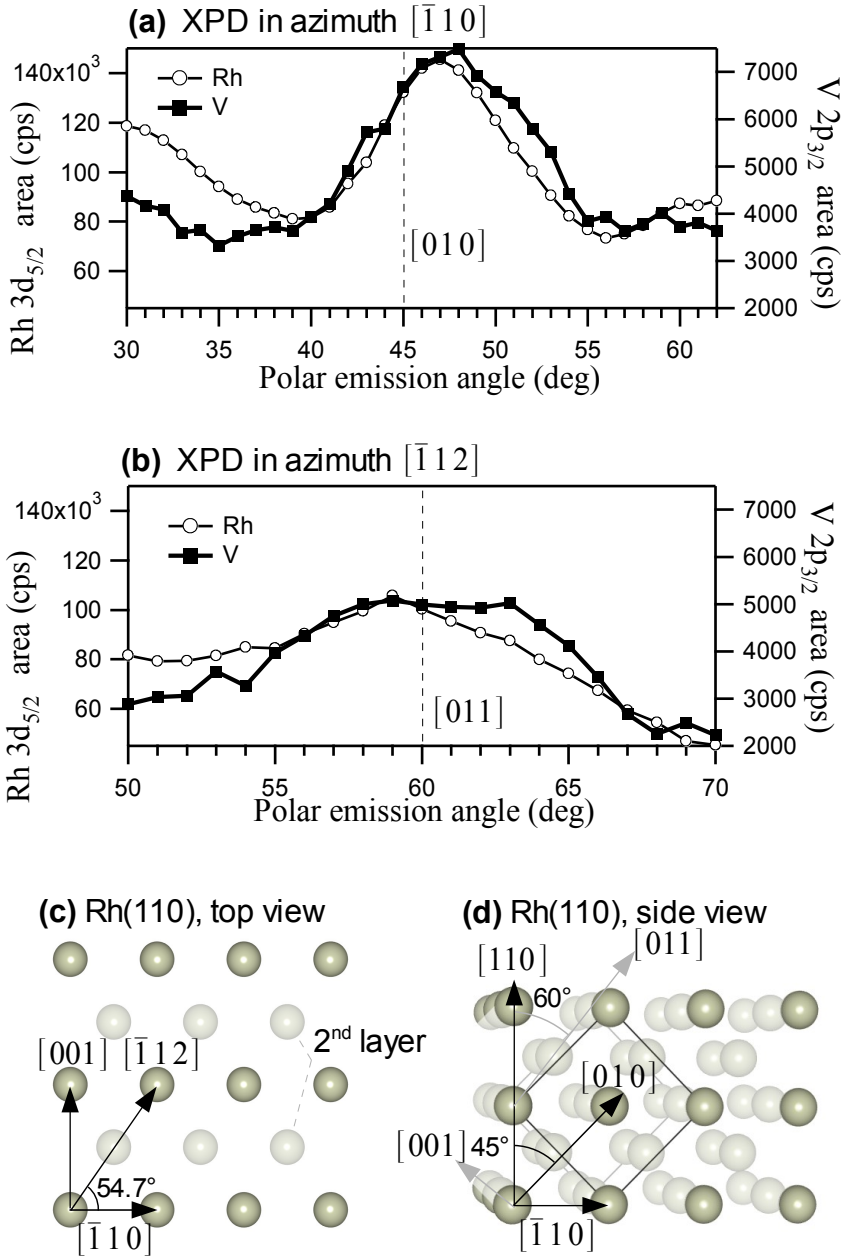

Fig. 4.39: Polar emission angle dependence of Rh $3d_{5/2}$ and V $2p_{3/2}$ integrated intensities at V–Rh(110)–(1×2) in azimuth $[\bar{1}10]$ *(a) and* $[\bar{1}12]$ *(b). Ball model of the ideal fcc(110) surface atomic structure is depicted in (c), (d). The XPD curves were obtained by Al Kα X-ray radiation. Polar emission angle values are referred to the surface normal.*

More information about the surface atomic structure was obtained by STM measurements. In Fig. 4.40, STM images of the clean Rh(110) surface and Rh(110) with 2 ML of V post-annealed at 973 K are compared. In the STM images atomic positions in the Rh(110) surface lattice are resolved. At the surface of the V–Rh(110)–(1×2) alloy, deep grooves of random length between the $[\bar{1}10]$ rows

appeared. The electron density along the $[\bar{1}10]$ rows on the both sides of these troughs displays periodicity correspondent to the double lattice parameter in the $[\bar{1}10]$ direction, as shown in the *A-B* and *C-D* line scans in Fig. 4.40(c,d). This intensity modulation can be assigned to a geometrical effect of the reconstruction of the surface Rh atoms along $[\bar{1}10]$ rows. Such reconstruction explains the (2×1) pattern observed by LEED. No signs of the (2×1) reconstruction were visible in the $[\bar{1}10]$ rows without any deep groove on a side, as demonstrates the line scan *E-F* in Fig. 4.40(c,d).

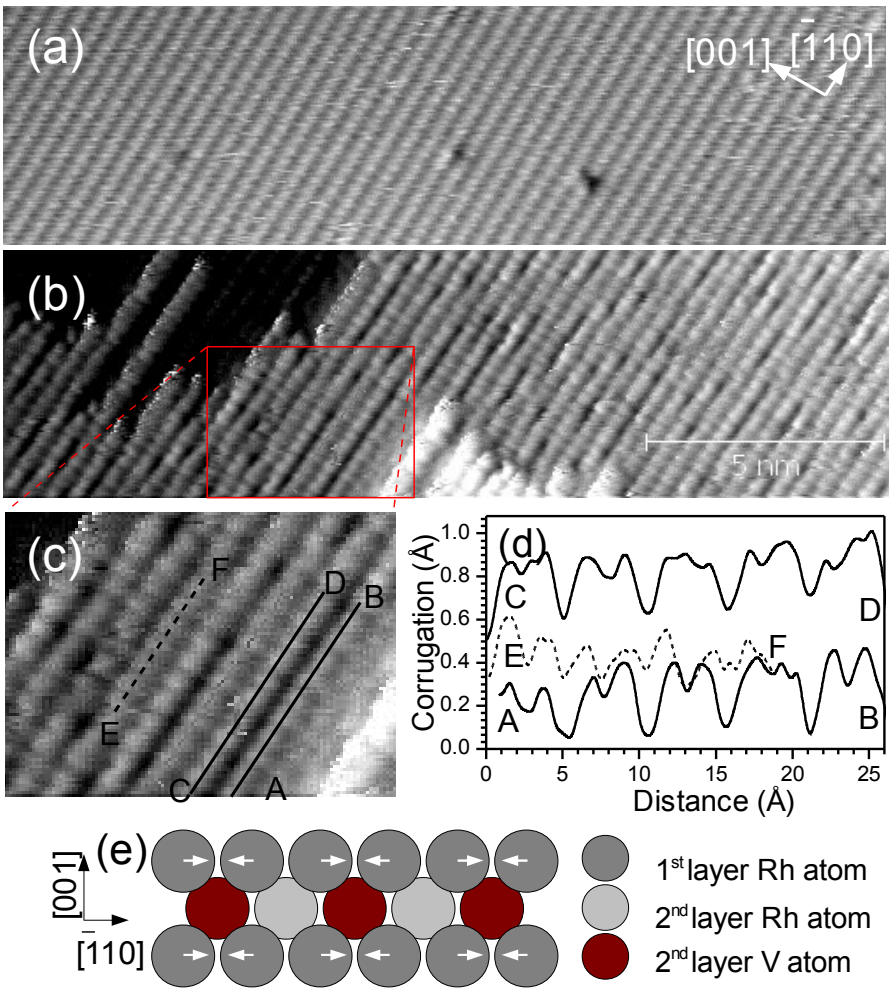

Fig. 4.40: (a) STM image of clean Rh(110) surface, (b) after deposition of 2 ML V at the substrate temperature of 823 K and post-annealing at 973 K. Image size 185 Å × 50 Å, tunnelling voltage 52 mV, tunnelling current 3.5 nA. (d) Line scan profiles showing the corrugation along the lines in the zoomed area (c).(e) Top view on ball model for the vanadium induced (2×1) surface reconstruction. The arrows indicate the direction of atom position shift.

Considering the fact that vanadium diffuses to the Rh near surface layers leaving topmost layer almost V free under the used experimental conditions and assuming that some V remain in the second layer in substitutional sites, we can conclude that the deep grooves correspond to the segments of the second layer $[\bar{1}10]$ rows containing V atoms. In these segments, each second lattice site is occupied by a V atom, which induces the Rh dimer formation in the rows lying above. A model proposed on the above results and assumptions is given in Fig. 4.40(e). The model partially agrees with the expected ordering correspondent to the $L1_2$ structure (Fig. 4.38). On the other hand, no signs of the $L1_2$-like structure at the Rh(110) surface have been observed in STM images. The deep grooves indicating the presence of the subsurface vanadium would be aligned next to each other in such case. Apparently such ordering was avoided. They hardly ever existed next to each other and, in fact, small areas where they appeared along the [001] direction in each second gap between $[\bar{1}10]$ rows could be observed in the STM images. This ordering could be the origin of the faint (1×2) spots observed in the LEED pattern. It indicates that under certain conditions a (2×2) phase with 25% vanadium concentration in the second surface layer could be formed. The formation of the V–Rh subsurface alloy with no V on the surface and relatively low V concentration in the second layer can be rationalized by analogy with the similar V–Pd subsurface alloy [22,25,98]. On Pd(111) surface, vanadium diffuses into Pd subsurface layers already at a temperature of 573 K and forms $(\sqrt{3}\times\sqrt{3})R30°$ structure with V atoms incorporated in the second layer. *Ab-initio* density-functional calculations showed that the formation of a strong heteroatomic Pd–V bond is the driving force that makes the formation of the Pd–V surface alloy an exothermic process. It was concluded that the total energy is lowered by (1) the avoidance of low-coordination sites of V atoms; (2) the avoidance of V–V nearest neighbours and of the V–V second or third neighbours sharing common Pd neighbours; and (3) because V positions in the subsurface Pd layer are slightly more favourable than V positions within the bulk. Since the third conclusion of the theory applies for submonolayer amounts of V, it can be neglected here. On the other hand, the first two principles most likely drives the (2×1) and the faint (1×2) V–Rh(110) structures observed by LEED and STM.

Taking into account the above mentioned model of the (2×1) reconstruction with V atoms located in the second layer under the deep grooves observed in STM

images, concentration of vanadium in the second layer after the annealing at 973 K can be estimated and yields to the value of 0.15 ML. That means that most of the deposited vanadium diffused into the deeper layers after the annealing. This behaviour has already been observed on polycrystalline Rh [6]. Annealing of the rhodium substrate at 950 K after the deposition of 1–2.5 ML of V leads to a state with the second Rh surface layer saturated with vanadium and excess vanadium dissolved in the bulk. Further annealing at 1073 K destabilizes the subsurface layer and V diffuses into the bulk. On the relatively opened Rh(110) surface, the temperature destabilization of the second layer with V can be more pronounced and can explain the estimated low V concentration after the annealing at 973 K.

The STM image of the Rh(110) surface with 2 ML of V after the annealing at 1073 K is displayed in Fig. 4.41(a). The STM revealed that the (1×2) LEED pattern created after the high temperature annealing originates from the (1×2) missing-row phase, which first layer is an ordered array of one-dimensional atomic chains along the $[\bar{1}10]$ direction. Apart from the areas of the missing-row phase, areas of (1×1) phase are visible in the STM image, too. No signs of the deep grooves with the (2×1) reconstruction have been observed, which indicates that the vanadium in the second layer diffused into deeper layers. Indication of the diffusion was visible also in photoemission spectra, as will be shown further. On the basis of the above mentioned results, a tentative model of the (1×2) missing-row reconstruction is proposed in Fig. 4.41(b).

The high temperature stability of the missing-row reconstruction is rather surprising. *Ab-initio* calculations [99] showed that the missing row reconstruction of the bare Rh(110) surface is energetically unfavoured. It can be achieved by H_2 titration of the (2×2)*p*2*mg* oxygen structure at about 400 K but it is thermodynamically unstable and irreversibly converts to the (1×1) phase upon heating at temperatures above 480 K [100]. In order to be sure that no impurities were responsible for the (1×2) reconstruction at the high temperature, pure Rh(110) crystal was treated in the exactly same way as the one with vanadium. No reconstruction other than (1×1) was observed. It proofed the stimulation of the (1×2) missing-row reconstruction by subsurface vanadium.

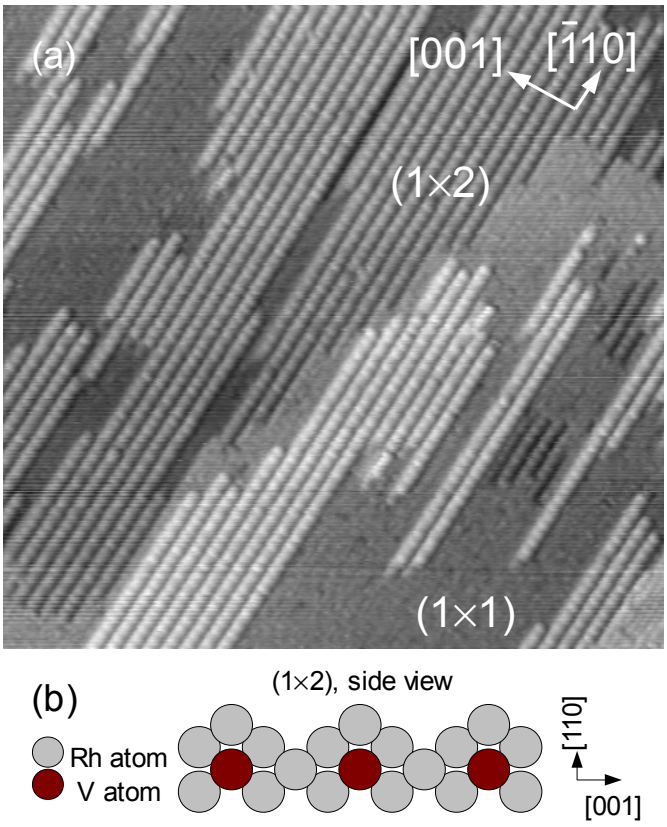

Fig. 4.41: (a) The STM image of Rh(110) surface with 2 ML of V after annealing at 1073 K. Image size 341×341 Å, tunnelling voltage -77 mV, tunnelling current 3.5 nA. (b) Side view of tentative ball model of the (1×2) missing-row reconstruction at the Rh(110) surface after the deposition of 2 ML of V and post-annealing at 1073 K.

4.4.4 SRPES characterisation

The electronic properties of the V–Rh(110) subsurface alloys were probed by means of photoemission spectroscopy employing synchrotron radiation. Photoemission from vanadium is displayed in Fig. 4.42. The BE of the V $2p_{3/2}$ peak was detected at 512.8 eV, at the BE very close to the case of V–Rh(111) subsurface alloy (512.7 eV, Fig. 4.9, Sec. 4.3.3). The BE of the V $2p_{3/2}$ peak was the same for the both Rh(110) surface reconstructions. Only the intensity decreased after the annealing at 1073 K and formation of the (1×2) missing-row reconstruction. The decrease in the intensity supports the assumption about the vanadium diffusion into the deeper layers.

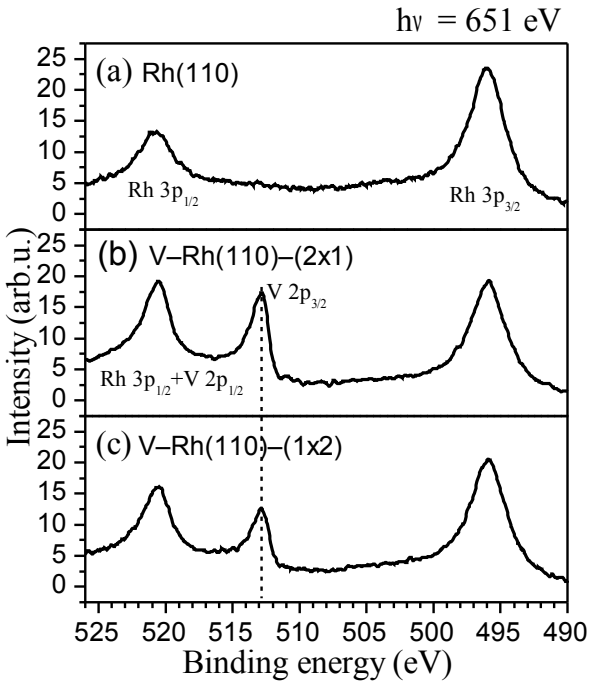

Fig. 4.42: V 2p and Rh 3p photoemission spectra of the (a) clean Rh(110); (b) V–Rh(110)–(2×1); (c) V–Rh(110)–(1×2) subsurface alloys. The spectra were detected at a photon energy of 651 eV.

Photoemission spectra of the Rh $3d_{5/2}$ core level of the clean Rh(110) surface and V–Rh(110) alloy with both surface reconstructions are displayed in Fig. 4.43. The spectra were measured at 380 eV excitation energy, at which the component from the top-most surface atoms was readily resolved (Fig. 4.43(a)). The spectra were decomposed into bulk and surface components using Shirley-type background [35] and Doniach-Šunjić line shapes [35,75] convoluted with Gaussian profile. The BE values of the peak positions are estimated with the accuracy of 0.05 eV. Bulk component (*B*) at the clean unreconstructed Rh(110) surface was detected at 307.06 eV and the surface component (*S*) at 306.39 eV. The surface core level shift of 0.67 eV on the Rh(110) is in good agreement with previously reported SCLS values (0.675±0.005 [101]; 0.65 [102]). A third component was necessary to be added in the spectrum from the V–Rh(110)–(2×1) alloy in order to get a good fit of the experimental curve (Fig. 4.43(b)). The third component (S_a) was found at a BE of 306.68 eV and it can be assigned to the Rh atoms at the surface with a vanadium neighbour located in the second layer. The energy shift from the surface component

of the clean Rh surface atoms is +0.29 eV, which is comparable with the shift +0.22 eV observed at the V–Rh(111)–(2×2) subsurface alloy (see, for instance, Table 4 in Sec. 4.3.3).

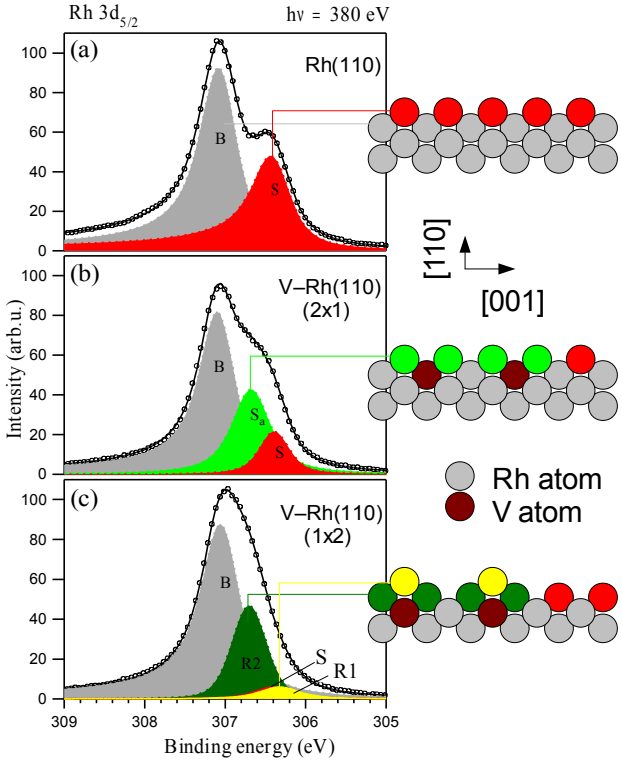

Fig. 4.43: Rh 3d$_{5/2}$ core-level photoemission spectra of (a) the clean Rh(110), (b) V–Rh(110)–(2×1) and (c) V–Rh(110)–(1×2) alloy surface. The data measured after the background subtraction (circles) were decomposed into components (dashed curves). The solid curves correspond to the fit results. The components are described in the text.

The fitting of the Rh 3d$_{5/2}$ spectrum of the V–Rh(110) with the (1×2) reconstruction is more delicate and less reliable, since four components must be taken into consideration. Apart from the bulk component, surface component from the non-reconstructed (1×1) areas and two components from the (1×2) areas were taken into consideration (Fig. 4.43(c)). One component (*R1*) is due to the emission from the (1×2) first layer atoms with the lowest coordination number and the second component (*R2*) corresponds to the emission from the underlying atoms in the troughs along the $[\bar{1}10]$ direction. These two components were measured at metastable (1×2) missing-row reconstruction of bare Rh(110) surface with SCLS at -0.715 (*R1*) and -0.445 eV (*R2*) [101]. The binding energies of the clean surface

component and the component *R1* of the (1×2) missing-row reconstruction are very similar. Their values were fixed during the fitting procedure. The component *R1* was found at a BE of 306.66 eV with a SCLS of 0.34 eV. The shift of the *R1* component to higher BE as compared with bare Rh might be again due to the influence of the subsurface vanadium.

4.4.5 Interaction with CO

The Rh(110) and V–Rh(110)–(1×2) surfaces were exposed to 10 L of CO at a temperature of 300 K. Under such conditions, Rh(110) surface is covered by a saturation CO layer with CO molecules adsorbed predominantly in bridge sites [95,96]. The saturation coverage of CO adsorbed on unreconstructed Rh(110) surface corresponds to 1 ML with respect to (1×1) Rh(110) surface with an ordered *p2mg*(2×1)–2CO structure, where the CO molecules are arranged in a zig-zag fashion along the $[\bar{1}10]$ direction with the CO molecular axis oriented approximately 24° from the surface normal [103].

The photoemission spectra of O 1s core-levels recorded after exposing the clean and V–Rh alloy surfaces to a CO saturation dose at room temperature are plotted in Fig. 4.44(a,b). The spectra were decomposed into two components using Voigt functions after linear background subtraction. The spectrum from the CO on Rh(110) (Fig. 4.44(a)) is in good agreement with previous photoemission studies of *p2mg*(2×1)–2CO overlayers on Rh(110) [96,104]. The component *b* at 530.8 eV was attributed to the CO molecules in bridge sites bounded to two surface Rh atoms and the component *t* at 531.9 eV to CO atoms in on-top sites. Considering the area of O 1s spectrum components proportional to CO surface coverage and assuming 1 ML CO coverage, the surface coverage correspondent to the two different adsorption sites can be determined. It gives 0.15 ML for CO in on-top sites and 0.85 ML for CO in bridge sites, in agreement with the study [104].

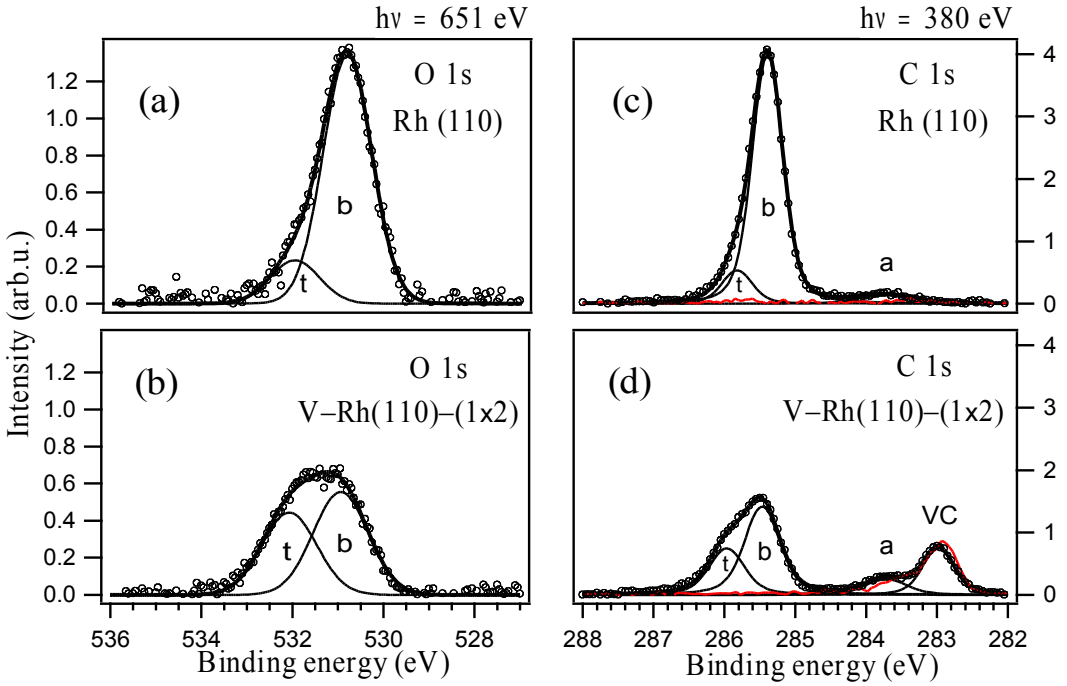

Fig. 4.44: C 1s and O 1s photoemssion spectra of (a),(c) the Rh(110) and (b), (d) V–Rh(110)–(1×2) surfaces after 10 L CO dose. Red curves correspond to the surfaces before the CO dose. The components b correspond to CO molecules adsorbed in short bridge positions; t to CO adsorbed in on-top positions; component a corresponds to atomic carbon and VC to vanadium carbide.

O 1s spectrum from the CO adsorbed on the V–Rh(110)–(1×2) surface is plotted in Fig. 4.44(b). The CO adsorption on the missing row V–Rh(110) surface was different in comparison with the Rh(110) surface but very similar to the CO adsorption observed on the metastable (1×2) missing row Rh(110) surface [96] as far as the O 1s photoemission is concerned. The LEED and XPS study of the CO adsorption on the metastable (1×2) reconstructed Rh(110) surface showed equivalent amounts of CO adsorbed in bridge and on-top positions which exhibited (2×2)*p2mg* LEED pattern. Moreover, the CO layer on the reconstructed Rh(110) showed the same saturation coverage as on the unreconstructed, i.e. one monolayer. The O 1s spectrum of the CO layer on the V–Rh(110)–(1×2) surface also indicates two bonding configurations characterized by O 1s peak components at 530.9 and 531.2 eV binding energies with intensity ratio 1.3. In analogy with the study of CO adsorption on the metastable (1×2) missing row Rh(110) reconstruction, the two states can be assigned to the CO atoms adsorbed in the short bridge sites on the $[\bar{1}10]$ rows and CO atoms adsorbed in the on-top sites on the (111) nano-facets

between the rows. On the other hand, the total O 1s intensity shows CO coverage reduction down to about 0.7 ML.

The C1s region was also examined and is presented in Fig. 4.44(c,d). On the clean Rh(110) surface, two C 1s components were found at 285.4 and 285.8 eV (Fig. 4.44(c)). In correspondence with the O 1s spectrum, the components are attributed to the CO molecules in bridge and on-top sites, respectively. Another small component at a BE of 283.7 eV was detected after the CO adsorption and it can be attributed to atomic carbon from CO dissociation on surface defects [105]. The C 1s spectrum from the V–Rh(110)–(1×2) surface before the CO adsorption revealed also the presence of the atomic carbon and in addition, a carbon C 1s peak at a BE of 283 eV. The latter one can be attributed to vanadium carbide VC [106]. None of the carbon peaks were present when the V–Rh(110) alloy was formed. Atomic carbon and VC appeared during the cycles of flash heating which were done to keep the surface free of molecules adsorbed from the ambient atmosphere. Most likely, the carbon contaminants appeared due to a molecule dissociation on surface defects. No more VC was formed after the CO adsorption but its presence could be the reason of the reduced CO saturation coverage.

The C 1s peak binding energies of the CO molecules adsorbed in bridge and on-top sites were found at 285.5 and 286.0 eV, slightly shifted to higher binding energies similarly as in the case of the O 1s spectra. The shift to the higher binding energies can be explained by weaker final state screening induced by a charge transfer from rhodium atoms towards their bond with vanadium atoms. It indicates weaker CO–Rh(110) surface bond, and the energy difference between 4σ and $5\sigma/1\pi$ CO molecular orbitals supports this assumption. The CO molecular orbitals from CO adsorbed on the Rh(110) and V–Rh(110)–(1×2) measured at 50 eV photon energy are compared in Fig. 4.45. The energy difference between the molecular orbital increased by 0.2 eV, which indicates the weakening of the CO-Rh bond, as it was already observed at the V–Rh(111) alloy surfaces (Fig. 4.14, Sec. 4.3.4).

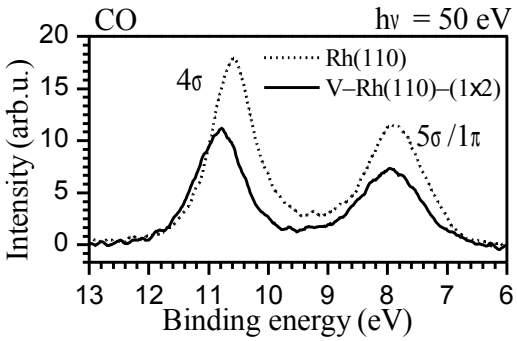

Fig. 4.45: Photoemission spectra of the 4σ and 5σ/1π orbitals of CO molecules adsorbed on the Rh(110) (dotted curve) and V–Rh(110)–(1×2) surface (solid curve). The spectra were recorded after the CO saturation dose at 300 K.

4.4.6 Valence band structure

Valence bands of the Rh(110) and V–Rh(110) subsurface alloys were studied by means of ARUPS employing synchrotron radiation and photon energies 35 and 55 eV. Within the used experimental parameters, The valence band spectra are dominated by photoemission from rhodium. (Sec. 4.3.7) Valence band spectra from the clean Rh(110) and V–Rh(110)–(1×2) subsurface alloy, taken at several different photoemission angles, are compared in Fig. 4.46. The valence band spectra from the V–Rh(110)–(2×1) surface exhibited very similar changes as those observed on the alloy with (1×2) reconstruction (not shown). In general, the alloying induced a decrease of the intensity at and near the Fermi level and increase of the intensity around 2 eV BE. This change is visible more clearly in the angle-integrated valence band spectra shown in Fig. 4.47. The angle-integrated valence band spectra reflect joint density of states at the surface. The alloying stimulated a shift of the valence band centre-of-mass to higher binding energies of about 0.06±0.02 eV. The same shift was measured at both 35 and 55 eV photon energies.

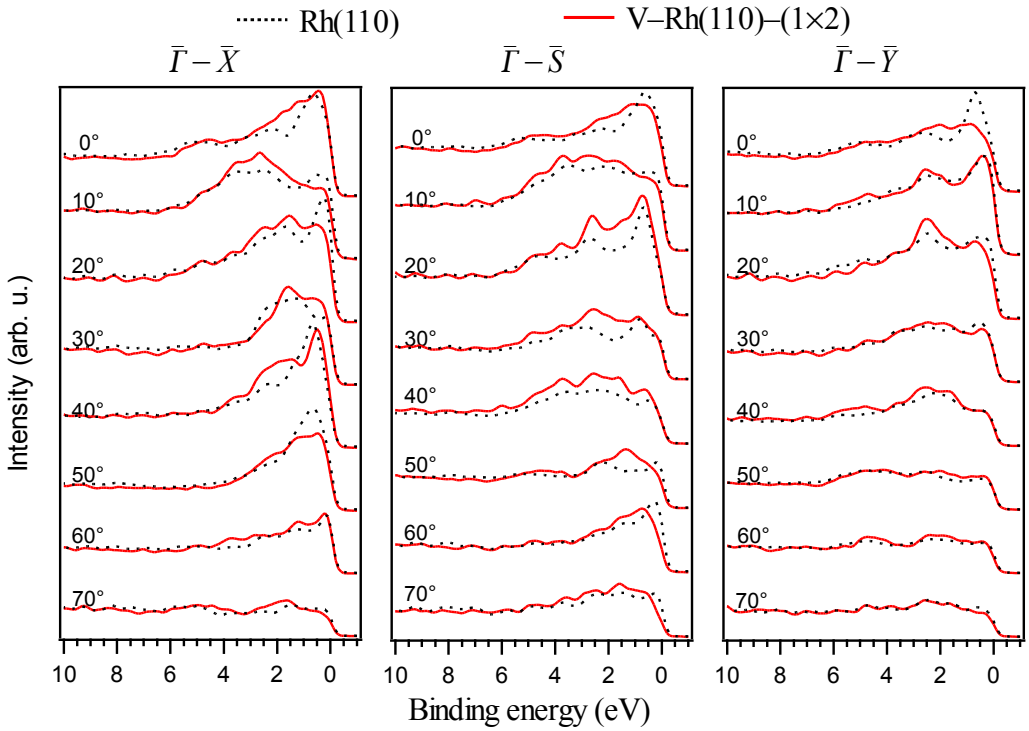

Fig. 4.46: Valence band spectra of the clean Rh(110) (dashed curves) and the V–Rh(110)–(1×2) alloy (solid lines) taken at different polar emission angles along directions $\bar{\Gamma}-\bar{X}$, $\bar{\Gamma}-\bar{S}$, $\bar{\Gamma}-\bar{Y}$ in surface Brillouin zone. Spectra were obtained at a photon energy of 55 eV.

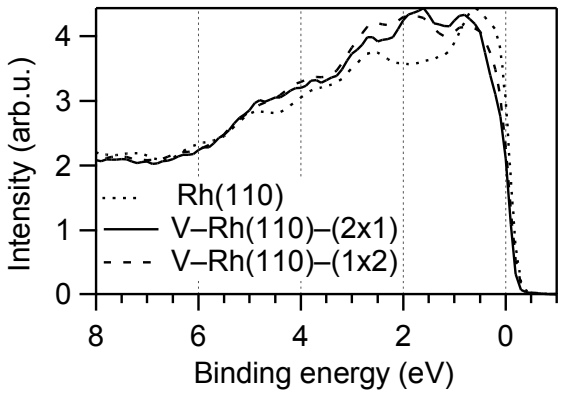

Fig. 4.47: Angle-integrated valence band spectra of the clean Rh(110), V–Rh(110)–(2×1) and V–Rh(110)–(1×2) surface measured at 55 eV photon energy.

Valence band maps of the Rh(110) and V–Rh(110)–(1×2) surfaces along $\bar{\Gamma}-\bar{\mathrm{X}}$ and $\bar{\Gamma}-\bar{\mathrm{S}}$ directions (see Attachment) are compared in Fig. 4.48. The transformation

from ARUPS spectra to the reciprocal space was done as described above (Sec. 2.5). Surface states, marked by red guidelines, were found following the procedure described in details in Sec. 4.3.7 . To recapitulate, the bands were measured at two photon energies (35 and 55 eV) before and after the CO saturation dose. The states which were quenched strongly by the adsorption, and their parallel component of the ***k*** vector remained unchanged at different photon energy, were classified as surface states.

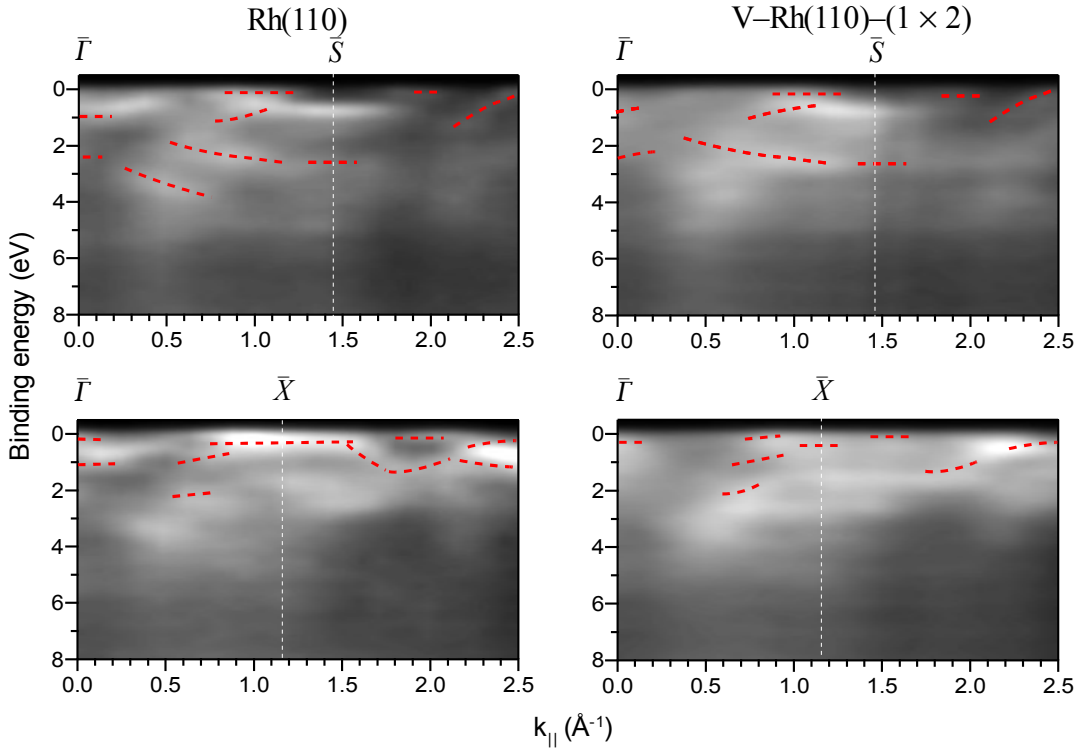

Fig. 4.48: Valence band maps of the Rh(110) and V–Rh(110)–(1×2) surfaces measured at 55 eV photon energy along the $\bar{\Gamma}-\bar{\mathrm{S}}$ *and* $\bar{\Gamma}-\bar{\mathrm{X}}$ *directions in the surface Brillouin zone. The red dashed guidelines mark surface states.*

The experimentally determined surface states of the clean Rh(110) can be compared with theoretically calculated dispersion relations. The ground state valence band electronic structure of Rh(110) have been investigated by Eichler et al.[76,89] by self-consistent *ab-initio* local-density-functional theory. The surface dispersion relations determined experimentally in this work are quite comparable with the theoretical prediction as shows Fig. 4.49, where the dispersion relations along the $\bar{\Gamma}-\bar{\mathrm{S}}$ direction are compared. For instance, the surface states at $\bar{\Gamma}$ point were predicted at BE 1.0 and 2.5 eV. The experimental values are 1.0 and 2.3 eV. At the

$\bar{S}$ point, surface states at a BE range of 3–3.5 eV were predicted. The experiment showed surface states at a slightly lower BE of 2.7 eV. Some surface states determined experimentally, such as those around the ($\bar{\Gamma} + \bar{S}$)/2 point, are missing in the presented theoretical calculation. However, the theoretical study showed that surface dispersion relations at Rh(110) are affected by surface relaxation. The difference between the theory and experiment might be due to different surface relaxation considered in the theoretical model. Another reason might be only in the criterion used in the theory to define surface states.

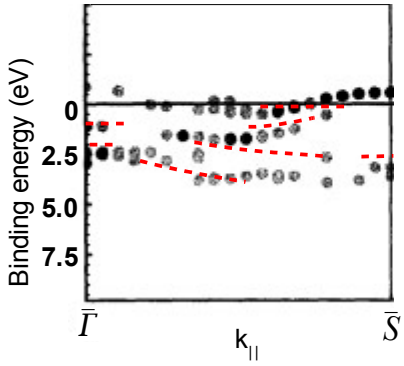

Fig. 4.49: Dispersion relations of electronic surface states at Rh(110) calculated by A. Eichler et al [76] *(black and grey dots) and determined experimentally in this work (red dashed lines).*

The bands of surface states on the V–Rh(110) alloy were reduced in amount as well as in the intensity. The decrease in the intensity is the most significant in the states near the Fermi level, as can be seen clearly in Fig. 4.48 in the $\bar{\Gamma} - \bar{X}$ direction. The depletion of the surface states might be caused by a surface reconstruction and relaxation and/or by a partial charge transfer to the bonds with the subsurface vanadium. Since the both V–Rh(110) surfaces with different reconstructions displayed very similar changes in the valence band spectra, it is likely that the latter case was dominant.

The shift of the Rh *d*-band electrons to the bimetallic bond explains the weakening of the CO bond with the metal surface and indicates the same electronic mechanism as at the V–Rh(111)–(2×2) subsurface alloy. By the reduction of the density of states near the Fermi level less *d*-electrons are available to the bond with CO $2\pi^*$ orbital.

4.4.7 Conclusions

The study of the V–Rh(110) bimetallic system prepared by the evaporation of two monolayers of V onto the Rh(110) surface at elevated temperature and further annealing at higher temperatures confirmed general behaviour of this bimetallic system already observed under the similar experimental conditions. Similarly as it has been observed on Rh(111) and polycrystalline Rh, the vanadium diffuses into the Rh bulk at temperatures higher than 823 K, leaves the top-most layer vanadium free and forms subsurface substitutional alloy with V atoms located in Rh lattice sites. On the Rh(110) surface, annealing at a temperature of 973 K resulted in (2×1) reconstruction. The STM images showed that the reconstruction corresponds to a dimer-like structure along the $[\bar{1}\,1\,0]$ rows.

After the annealing at 1073, the vanadium diffused into deeper layers, (2×1) reconstruction disappeared and areas with (1×1) unreconstructed and (1×2) missing-row phase were formed. The presence of V in subsurface region is essential for the missing-row reconstruction, since such surface structure is unstable on the pure Rh(110) surface. The (1×2) missing-row reconstructions on (110) face are stable on fcc 5*d* metals Au, Pt, and Ir. Their stability have been the subject of attention for several theoretical studies [99,107,108]. The *ab-initio* DFT calculations showed that in case of Au and Pt(110) surface the delocalisation of *d*-electrons at the surface and the accumulation of *sp*-electrons close to the surface associated with multilayer relaxations, are important factors in stabilizing the missing-row configurations. Our measurements of the Rh and V–Rh valence band maps obtained by the angle-resolved photoemission spectroscopy revealed a pronounced depletion of the surface localized states at Rh(110) upon alloying with subsurface vanadium. Thus, the possible *d-d* hybridisation between the Rh and V atoms could stimulate a delocalisation of the Rh *d*-electrons at the surface by a movement of electron charge from the top of Rh toward the bonds with subsurface V, induce a significant relaxation and stabilize the missing-row reconstruction.

Noteworthy is the thermal stability of the (1×2) missing-row reconstruction. It is expected that the missing row reconstruction can exhibit interesting chemical reactivity. Previous study of the hydrogen and NO adsorption on the metastable (1×2) reconstructed Rh(110) surface showed strong influence of the structure on the

adsorption [109]. The stable reconstruction can, for instance, serve as a template for preparation of new materials such as various 1D nano-structures or self-assembled layers.

The alloying and formation of (1×2) missing-row reconstruction modified also CO adsorption properties of the metal surface. Due to the reconstruction, the ratio between the population of bridge and on-top sites was changed in favour of on-top positions. The alloying caused a weakening of the CO-metal bond. Similarly as at the other V–Rh subsurface alloys studied in this work, the weaker CO-metal surface bond was in a correlation with the reduction of the surface states near the Fermi level.

5 SUMMARY

Thin mixed Rh–V layers deposited on polycrystalline γ-Al_2O_3, as well as Rh–V bimetallic model systems prepared by V deposition onto polycrystalline Rh, Rh(111) and Rh(110) single crystals, have been studied by means of surface sensitive techniques XPS, TPD, SRPES, XPD, ARUPS and STM. The results of this study improve the understanding of atomic and electronic structure of the bimetallic system and their relation to the interaction with CO and O_2 gas molecules. The main results and conclusions are summarised as follows.

Rh−V layers supported by γ-Al_2O_3

Thin mixed Rh–V layers supported by polycrystalline γ-Al_2O_3 were prepared by UHV vapour deposition and studied by XPS and TPD. The investigated films were different in the order of the metal evaporation. The obtained results showed a noticeable influence of a small amount of V on the chemisorption properties of Rh thin layers and particles supported on γ-Al_2O_3. The presence of vanadium in the subsurface regions of the bimetallic Rh–V phase caused the relative increase of CO molecules desorbing from sites with lower desorption energy. A noticeable CO dissociation was observed on the mixed layers. The performed study also showed a strong dependence of the chemisorption properties on the amount of V and on the way of preparation of the mixed film.

V on polycrystalline Rh foil

One monolayer of V was deposited on the polycrystalline Rh foil at temperatures 295 K and 795 K. At the former case, vanadium remains on the surface where it is rapidly deactivated as far as CO adsorption on RT is concerned. On the other hand, vanadium diffuses into Rh subsurface region at the elevated temperature and modifies the chemisorption properties of surface layer. The strength of the CO bond with the rhodium is lowered on the alloy and the thermo-desorption from hollow and bridge like sites is favoured in comparison to the pure Rh surface.

V on Rh(111)

V–Rh(111) model systems were prepared by vapour deposition of 0.4 ML and 2.5 ML of V in vacuum on the Rh(111) surface at an elevated temperature of 823 K.

The latter one was further annealed up to 1023 K and a long-range ordered (2×2) surface reconstruction appeared. In both cases, a subsurface alloy was formed and both surfaces exhibited very similar composition, electronic structure and CO and O_2 adsorption properties. XPD at the V–Rh(111)–(2×2) subsurface alloy revealed V atoms located in substitutional positions in the Rh crystal lattice. Rh_3V alloy with $L1_2$-like structure was formed. The topmost layer consisted of Rh atoms in (2×2) reconstruction above the subsurface vanadium atoms with an inward relaxation. A model of the surface reconstruction was derived from the diffraction measurements.

The alloying resulted in Rh $3d_{5/2}$ surface core-level shift to higher BE by 0.2 eV and in changes in the metal valence band. The electronic changes are very likely caused by the formation of heteroatomic Rh–V bond accompanied by a strong *d-d* hybridisation. As a result, valence band surface states under the Fermi level, which hybridise with CO molecular orbitals, were reduced considerably upon alloying. This effect correlated with lower activity towards CO adsorption. CO saturation coverage at 300 K was reduced and the CO-metal surface bond was weaker. Desorption from hollow sites was favoured over desorption from on-top sites.

Oxygen adsorbed on the alloy surface interacted with the subsurface vanadium already at 300 K. Further annealing resulted in formation of a stable surface vanadium-oxide, which reduced the Rh–V heteroatomic bonds and blocked the CO adsorption sites. The oxide could be reduced by vacuum annealing at temperatures between 873–1073 K. Annealing at higher temperatures leads to dissolution of the vanadium in the Rh bulk.

V on Rh(110)

Deposition of 2 ML of V onto Rh(110) surface at a substrate temperature of 823 K and further annealing at elevated temperature lead to diffusion of vanadium into the Rh bulk and formation of V–Rh(110) subsurface alloy with vanadium atoms incorporated in the Rh fcc lattice, as implies from XPD, LEED and STM measurements. Annealing at 973 K leads to formation of (2×1) surface structure with chains of Rh dimers along the $[\bar{1}10]$ surface rows induced by the vanadium atoms located in the underlying rows in the second layer. Annealing at 1073 K causes diffusion of the subsurface vanadium into deeper layers and formation of (1×2) missing-row reconstruction of the Rh(110) surface induced by vanadium atoms

located, most probably, in the second subsurface layer.

The alloying shifted the surface component of the Rh $3d_{5/2}$ core level as well as the centre-of-mass of the valence band towards higher binding energies and reduced the density of surface states near the Fermi level very much in the manner of the V–Rh(111) subsurface alloys. Detailed valence band maps showed depletion of the surface localised states upon the alloying. The charge transfer towards the bonds with subsurface vanadium could be the mechanism stabilizing the missing-row reconstruction. In addition, vanadium stimulated changes in the electronic structure which are most likely weakening the adsorption of CO molecules on Rh(110) surface, similarly as at the other Rh surfaces.

In conclusion, the properties observed at the mixed Rh–V layers supported by γ-Al_2O_3 and their interaction with carbon monoxide and oxygen can be understood by comparison with V–Rh(111), V–Rh(110) and V–polycrystalline Rh model systems At a temperature around 800 K and higher, subsurface alloy at all the studied model systems was formed and similar changes in the electronic structure were observed. Thermode-sorption spectra which corresponded to CO molecular adsorption and desorption from the supported layers were well reproduced on the model systems. That indicates the same type of electronic effects on both types of bimetallic systems. The study of the model systems also showed that the CO dissociation observed on the supported bimetallic layers is not related to the Rh–V alloying but to the morphology of the thin layer. These findings might play an important role in a design of a real catalyst based on Rh and V constituents.

BIBLIOGRAPHY

[1] Ertl, G. *Reactions at solid surfaces*. New Jersey: Wiley, 2009. ISBN 978-0470261019.

[2] Lee, HI and White, JM. Carbon-monoxide oxidation over Ru(001). *J. Catal.*, 1980, **63**, 261-264. ISSN 0021-9517.

[3] Over, H, Kim, YD, Seitsonen, AP, Wendt, S, Lundgren, E, Schmid, M, Varga, P, Morgante, A and Ertl, G. Atomic-scale structure and catalytic reactivity of the RuO_2(110) surface. *Science*, 2000, **287**, 1474-1476. ISSN 0036-8075.

[4] Assmann, J, Crihan, D, Knapp, M, Lundgren, E, Loffler, E, Muhler, M, Narkhede, V, Over, H, Schmid, M, Seitsonen, AP and Varga, P. Understanding the structural deactivation of ruthenium catalysts on an atomic scale under both oxidizing and reducing conditions. *Angew. Chem. Int. Ed.*, 2005, **44**, 917-920. ISSN 1433-7851.

[5] Gandhi, HS, Graham, GW and McCabe, RW. Automotive exhaust catalysis. *J. Catal.*, 2003, **216**, 433-442. ISSN 0021-9517.

[6] Reichl, W and Hayek, K. The vanadium subsurface alloy on polycrystalline rhodium: formation and catalytic properties. *J. Catal.*, 2004, **222**, 53-64. ISSN 0021-9517.

[7] Hanyš, P. *Low temperature co oxidation on bimetallic structures*. Prague, 2011. Doctoral thesis. Faculty of Mathematics and Physics, Charles University in Prague. Supervisor: Václav Nehasil.

[8] Rodriguez, JA and Goodman, DW. The nature of the metal metal bond in bimetallic surfaces. *Science*, 1992, **257**, 897-903. ISSN 0036-8075.

[9] Rodriguez, JA. Physical and chemical properties of bimetallic surfaces. *Surf. Sci. Rep.*, 1996, **24**, 223-287. ISSN 0167-5729.

[10] Law, YT, Skála, T, Píš, I, Nehasil, V, Vondráček, M and Zafeiratos, S. Bimetallic nickel-cobalt nanosized layers supported on polar ZnO surfaces: metal-support interaction and alloy effects studied by synchrotron radiation x-ray photoelectron spectroscopy. *J. Phys. Chem. C*, 2012, **116**, 10048-10056. ISSN 1932-7447.

[11] Lykhach, Y, Masek, K and Nehasil, V. Influence of the alumina surface orientation to the Rh particle growth and reconstruction. *Surf. Sci.*, 2002, **507**, 655-661. ISSN 0039-6028.

[12] Masek, K, Matolin, V and Gillet, M. Study of the growth of rhodium particles on different substrates. *Thin Solid Films*, 1995, **260**, 252-258. ISSN 0040-6090.

[13] Nehasil, V, Stara, I and Matolin, V. Study of desorption activation-energy on Rh-CO systems. *Czech. J. Phys.*, 1993, **43**, 957-961. ISSN 0011-4626.

[14] Nehasil, V, Janecek, P, Korotchenkov, G and Matolin, V. Investigation of behaviour of Rh deposited onto polycrystalline SnO_2 by means of TPD, AES and EELS. *Surf. Sci.*, 2003, **532**, 415-419. ISSN 0039-6028.

[15] Nehasil, V, Hrncir, T, Zafeiratos, S, Ladas, S and Matolin, V. Study of CO adsorption on Rh/alumina model catalysts in dependence on substrate orientation. *Surf. Sci.*, 2000, **454**, 289-294. ISSN 0039-6028.

[16] Stara, I, Di Salvo, JP, Nehasil, V, Matolin, V and Gillet, E. SSIMS and XPS studies of reconstruction of alumina-supported Rh particles. *Surf. Rev. Lett.*, 1998, **5**, 375-379. ISSN 0218-625X.

[17] Campbell, CT. Ultrathin metal films and particles on oxide surfaces: structural, electronic and chemisorptive properties. *Surf. Sci. Rep.*, 1997, **27**, 1-111. ISSN 0167-5729.

[18] Hüfner, S. *Photoelectron spectroscopy principles and applications*. Berlin: Springer, 2003. ISBN 3-540-41802-4.

[19] Hammer, B, Morikawa, Y and Nørskov, JK. CO chemisorption at metal surfaces and overlayers. *Phys. Rev. Lett.*, 1996, **76**, 2141-2144. ISSN 0031-9007.

[20] Sa, S, Silva, H, Brandao, L, Sousa, JM and Mendes, A. Catalysts for methanol steam reforming-a review. *Appl. Catal., B*, 2010, **99**, 43-57. ISSN 0926-3373.

[21] Klötzer, B, Unterberger, W and Hayek, K. Adsorption and hydrogenation of CO on Pd(111) and Rh(111) modified by subsurface vanadium. *Surf. Sci.*, 2003, **532-535**, 142-147. ISSN 0039-6028.

[22] Konvicka, C, Jeanvoine, Y, Lundgren, E, Kresse, G, Schmid, M, Hafner, J and Varga, P. Surface and subsurface alloy formation of vanadium on Pd(111). *Surf. Sci.*, 2000, **463**, 199-210. ISSN 0039-6028.

[23] Reichl, W and Hayek, K. Strong and coverage-independent promotion of catalytic activity of a noble metal by subsurface vanadium. *Surf. Sci.*, 2003, **537**, 247-252. ISSN 0039-6028.

[24] Surnev, S, Sock, M, Ramsey, MG, Netzer, FP, Klötzer, B, Unterberger, W and Hayek, K. Chemical reactivity of the V-Pd(111) subsurface alloy: adsorption of CO. *Surf. Sci.*, 2002, **511**, 392-400. ISSN 0039-6028.

[25] Hirschl, R and Hafner, J. First-principles study of Pd-V surface alloys I. Electronic structure of clean surfaces. *Surf. Sci.*, 2002, **498**, 21-36. ISSN 0039-6028.

[26] Hirschl, R and Hafner, J. First-principles study of Pd-V surface alloys II. Chemical reactivity. *Surf. Sci.*, 2002, **498**, 37-52. ISSN 0039-6028.

[27] Schennach, R. A review of the adsorption dynamics, reactivity and structure of Pd–V and Rh–V surface alloys. Norris CP (Ed.) *Trends in surface science research*. New York: Nova Science Publishers, 2006, 223-256. ISBN 1-59454-178-7.

[28] Waterstrat, RM and Manuszewski, RC. Vanadium-rhodium constitution diagram. *J. Less-Common Met.*, 1977, **52**, 293-305. ISSN 0022-5088.

[29] Wolverton, C, Ceder, G, de Fontaine, D and Dreyssé, H. Ab-initio determination of structural stability in fcc-based transition-metal alloys. *Phys. Rev. B*, 1993, **48**, 726-747. ISSN 0163-1829.

[30] Konvicka, C. *Characterisation of vanadium, vanadium-palladium and vanadium-rhodium single crystal surfaces*. Vienna, 2001. Dissertation. Institut fur Allgemeine Physik, Technische Universitat Wien. Supervisor: Peter Varga.

[31] Schennach, R, Krenn, G, Klötzer, B and Rendulic, KD. Adsorption of hydrogen and carbon monoxide on Rh(111)/V surface alloys. *Surf. Sci.*, 2003, **540**, 237-245. ISSN 0039-6028.

[32] Hayek, K, Jenewein, B, Klötzer, B and Reichl, W. Surface reactions on inverse model catalysts: CO adsorption and CO hydrogenation on vanadia- and ceria-

modified surfaces of rhodium and palladium. *Top. Catal.*, 2001, **14**, 25-33. ISSN 1022-5528.

[33] Schennach, R, Krenn, G and Rendulic, KD. The influence of the translational energy of methanol during adsorption on Rh (111) and on a rhodium/vanadium surface alloy. *Vacuum*, 2003, **71**, 89-93. ISSN 0042-207X.

[34] Krenn, G and Schennach, R. Adsorption and reaction of methanol on clean and oxygen modified rhodium/vanadium surface alloys. *J. Chem. Phys.*, 2004, **120**, 5729-5735. ISSN 0021-9606.

[35] Briggs, D and Grant, JT. *Surface analysis by auger and x-ray photoelectron spectroscopy*. UK: IM Publications, 2003. ISBN 1901019047.

[36] Tanuma, S, Powell, CJ and Penn, DR. Calculations of electron inelastic mean free paths (IMFPs) .4. Evaluation of calculated IMFPs and of the predictive IMFP formula TPP-2 for electron energies between 50 and 2000 eV. *Surf. Interf. Anal.*, 1993, **20**, 77-89. ISSN 0142-2421.

[37] Píš, I, Kobata, M, Matsushita, T, Nohira, H and Kobayashi, K. Hard-x-ray photoelectron diffraction from Si(001) covered by a 0-7-nm-thick SiO_2 layer. *App. Phys. Exp.*, 2010, **3**, 056701. ISSN 1882-0778.

[38] García de Abajo, FJ, Van Hove, MA and Fadley, CS. Multiple scattering of electrons in solids and molecules: a cluster-model approach. *Phys. Rev. B*, 2001, **63**, . ISSN 0163-1829.

[39] Fadley, CS, Thevuthasan, S, Kaduwela, AP, Westphal, C, Kim, YJ, Ynzunza, R, Len, P, Tober, E, Zhang, F, Wang, Z, Ruebush, S, Budge, A and Van Hove, MA. Photoelectron diffraction and holography - present status and future-prospects. *J. Electron. Spectrosc. Relat. Phenom.*, 1994, **68**, 19-47. ISSN 0368-2048.

[40] Matsushita, T, Matsui, F, Daimon, H and Hayashi, K. Photoelectron holography with improved image reconstruction. *J. Electron. Spectrosc. Relat. Phenom.*, 2010, **178**, 195-220. ISSN 0368-2048.

[41] Osterwalder, J, Fasel, R, Stuck, A, Aebi, P and Schlapbach, L. Holographic interpretation of photoelectron diffraction. *J. Electron. Spectrosc. Relat. Phenom.*, 1994, **68**, 1-18. ISSN 0368-2048.

[42] Winkelmann, A, Fadley, CS and de Abajo, FJG. High-energy photoelectron diffraction: model calculations and future possibilities. *New J. Phys.*, 2008, **10**, 113002. ISSN 1367-2630.

[43] Winkelmann, A, Schroter, B and Richter, W. Simulation of high energy photoelectron diffraction using many-beam dynamical kikuchi-band theory. *Phys. Rev. B*, 2004, **69**, 245417. ISSN 1098-0121.

[44] Williams, JR, Pis, I, Kobata, M, Winkelmann, A, Matsushita, T, Adachi, Y, Ohashi, N and Kobayashi, K. Observation and simulation of hard x ray photoelectron diffraction to determine polarity of polycrystalline zinc oxide films with rotation domains. *J. Appl. Phys.*, 2012, **111**, 033525. ISSN 0021-8979.

[45] F Javier García de Abajo. *Electron diffraction in atomic clusters for core level photoelectron diffraction simulations* [online]. http://nanophotonics.csic.es/static/widgets/edac/index.html.

[46] Tomohiro Matsushita. *Electron holography analysis tools* [online]. http://es.sourceforge.jp/projects/tmcoca/.

[47] de Siervo, A, Soares, EA, Landers, R, Fazan, TA, Morais, J and Kleiman, GG. Pd on Cu(111) studied by photoelectron diffraction. *Surf. Sci.*, 2002, **504**, 215-222. ISSN 0039-6028.

[48] Saiki, RS, Kaduwela, AP, Sagurton, M, Osterwalder, J, Friedman, DJ, Fadley, CS and Brundle, CR. X-ray photoelectron diffraction and low-energy electron-diffraction study of the interaction of oxygen with the Ni(001) surface - c(2x2) to saturated oxide. *Surf. Sci.*, 1993, **282**, 33-61. ISSN 0039-6028.

[49] Chen, Y, de Abajo, FJG, Chasse, A, Ynzunza, RX, Kaduwela, AP, Van Hove, MA and Fadley, CS. Convergence and reliability of the rehr-albers formalism in multiple-scattering calculations of photoelectron diffraction. *Phys. Rev. B*, 1998, **58**, 13121-13131. ISSN 1098-0121.

[50] Synchrotron Elettra. *Atomic calculation of photoionization cross-sections and asymmetry parameters* [online]. http://ulisse.elettra.trieste.it/services/elements/WebElements.html.

[51] Yeh, JJ. *Atomic calculation of photoionization cross-sections and asymmetry parameters*. Langhorne, PE (USA): Gordon and Breach Science Publishers, 1993. ISBN 2-88124-585-4.

[52] Yeh, JJ and Lindau, I. Atomic subshell photoionization cross-sections and asymmetry parameters - $1 \leq z \leq 103$. *At. Data Nucl. Data Tables*, 1985, **32**, 1-155. ISSN 0092-640X.

[53] King, DA. Thermal desorption from metal-surfaces. *Surf. Sci.*, 1975, **47**, 384-402. ISSN 0039-6028.

[54] Dejong, AM and Niemantsverdriet, JW. Thermal-desorption analysis - comparative test of 10 commonly applied procedures. *Surf. Sci.*, 1990, **233**, 355-365. ISSN 0039-6028.

[55] Redhead, P. Thermal desorption of gases. *Vacuum*, 1962, **12**, 203-211. ISSN 0042-207X.

[56] Tersoff, J and Hamann, DR. Theory and application for the scanning tunneling microscope. *Phys. Rev. Lett.*, 1983, **50**, 1998-2001. ISSN 0031-9007.

[57] Nehasil, V, Masek, K, Moreau, O and Matolin, V. Miniature electron bombardment evaporation source: evaporation rate measurement. *Czech. J. Phys.*, 1997, **47**, 261-268. ISSN 0011-4626.

[58] Nehasil, V. *Studium vlivu struktury povrchu rhodia na mechanizmus adsopce a katalytické oxidace CO*. Prague, 1996. Doctoral thesis. Faculty of Mathematics and Physics, Charles University in Prague. Supervisor: Vladimír Matolín.

[59] Libra, J. *Studium bimetalických systémů metodami úhlově rozlišené fotoelektronové spektroskopie*. Prague, 2007. Doctoral thesis. Faculty of Mathematics and Physics, Charles University in Prague. Supervisor: Vladimír Matolín.

[60] Dvořák, F. *Investigation of thin ceo2 layers by scanning tunneling microscopy (STM) and spectroscopy (STS)*. Prague, 2010. Diploma thesis. Faculty of Mathematics and Physics, Charles University in Prague. Supervisor: Josef Mysliveček.

[61] Vašina, R, Kolařík, V, Doležel, P, Mynář, M, Vondráček, M, Cháb, V, Slezák, J, Comicioli, C and Prince, KC. Mechanical design aspects of a soft x-ray plane grating monochromator. *Nucl. Instrum. Methods Phys. Res., Sect. A*, 2001, **467-468**,

561-564. ISSN 0168-9002.

[62] Synchrotron Elettra. *Materials science beamline* [online]. http://www.elettra.trieste.it/elettra-beamlines/material_science.html.

[63] Píš, I. *Study of gas molecule interaction with supported noncontinuous bimetallic films*. Prague, 2007. Diploma thesis. Faculty of Mathematics and Physics, Charles University in Prague. Supervisor: Václav Nehasil.

[64] Stara, I and Matolin, V. The influence of particle-size on CO adsorption on Pd alumina model catalysts. *Surf. Sci.*, 1994, **313**, 99-106. ISSN 0039-6028.

[65] Baumer, M, Biener, J and Madix, RJ. Growth, electronic properties and reactivity of vanadium deposited onto a thin alumina film. *Surf. Sci.*, 1999, **432**, 189-198. ISSN 0039-6028.

[66] Biener, J, Baumer, M, Madix, RJ, Liu, P, Nelson, E, Kendelewisz, T and Brown, G. Growth and electronic structure of vanadium on alpha-Al_2O_3(0001). *Surf. Sci.*, 2000, **449**, 50-60. ISSN 0039-6028.

[67] Magg, N, Giorgi, JB, Frank, MM, Immaraporn, B, Schroeder, T, Baumer, M and Freund, HJ. Alumina-supported vanadium nanoparticles: structural characterization and CO adsorption properties. *J. Am. Chem. Soc.*, 2004, **126**, 3616-3626. ISSN .

[68] Wiltner, A, Rosenhahn, A, Schneider, J, Becker, C, Pervan, P, Milun, M, Kralj, M and Wandelt, K. Growth of copper and vanadium on a thin Al_2O_3-film on Ni_3Al(111). *Thin Solid Films*, 2001, **400**, 71-75. ISSN 0040-6090.

[69] Sawatzky, GA and Post, D. X-ray photoelectron and auger-spectroscopy study of some vanadium-oxides. *Phys. Rev. B*, 1979, **20**, 1546-1555. ISSN 1098-0121.

[70] Kierren, B, Gourieux, T, Bertran, F and Krill, G. Oxygen-adsorption observed during the epitaxy of V(110) on the (11(2)over-bar0) alpha-Al_2O_3 surface. *Appl. Surf. Sci.*, 1993, **68**, 341-345. ISSN 0169-4332.

[71] Altman, EI and Gorte, RJ. A comparison of the desorption of CO from Pt and Rh particles on alpha-Al_2O_3(0001). *Surf. Sci.*, 1988, **195**, 392-402. ISSN 0039-6028.

[72] Belton, DN and Schmieg, SJ. Effect of Rh particle-size on CO desorption from Rh/alumina model catalysts. *Surf. Sci.*, 1988, **202**, 238-254. ISSN 0039-6028.

[73] Alexander V Naumkin, Anna Kraut-Vass, Stephen W Gaarenstroom and Cedric J Powell. *Nist x-ray photoelectron spectroscopy database* [online]. http://srdata.nist.gov/xps/.

[74] Frank, M and Baumer, M. From atoms to crystallites: adsorption on oxide-supported metal particles. *Phys. Chem. Chem. Phys.*, 2000, **2**, 3723-3737. ISSN 1463-9076.

[75] Doniach, S and Sunjic, M. Many-electron singularity in x-ray photoemission and x-ray line spectra from metals. *J. Phys. C: Solid State Phys.*, 1970, **3**, 285. ISSN 0022-3719.

[76] Eichler, A, Hafner, J, Furthmuller, J and Kresse, G. Structural and electronic properties of rhodium surfaces: an ab initio approach. *Surf. Sci.*, 1996, **346**, 300-321. ISSN 0039-6028.

[77] Krenn, G, Bako, I and Schennach, R. CO adsorption and CO and O coadsorption on Rh(111) studied by reflection absorption infrared spectroscopy and

density functional theory. *J. Chem. Phys.*, 2006, **124**, . ISSN 0021-9606.

[78] Beutler, A, Lundgren, E, Nyholm, R, Andersen, JN, Setlik, BJ and Heskett, D. Coverage- and temperature-dependent site occupancy of carbon monoxide on Rh(111) studied by high-resolution core-level photoemission. *Surf. Sci.*, 1998, **396**, 117-136. ISSN 0039-6028.

[79] Eck, S, Castellarin-Cudia, C, Surnev, S, Prince, KC, Ramsey, MG and Netzer, FP. Adsorption and reaction of CO on a ceria-Rh(111) "inverse model catalyst" surface. *Surf. Sci.*, 2003, **536**, 166-176. ISSN 0039-6028.

[80] Hanyš, P, Janeček, P, Šutara, F, Tsud, N, Matolín, V and Nehasil, V. Study of CO adsorption on Sn/Rh(111). *Surf. Sci.*, 2007, **601**, 3717-3721. ISSN 0039-6028.

[81] Kandler, J, Eltester, B, Busse, H, Castro, GR and Wandelt, K. Interaction of CO with the ordered $Ni_3Al(111)$ surface. *Surf. Sci.*, 1995, **331-333**, 685-690. ISSN 0039-6028.

[82] Miranda, R, Wandelt, K, Rieger, D and Schnell, RD. Angle-resolved photoemission of CO chemisorption on Pd(111). *Surf. Sci.*, 1984, **139**, 430-442. ISSN 0039-6028.

[83] Schoiswohl, J, Eck, S, Ramsey, MG, Andersen, JN, Surnev, S and Netzer, FP. Vanadium oxide nanostructures on Rh(111): promotion effect of CO adsorption and oxidation. *Surf. Sci.*, 2005, **580**, 122-136. ISSN 0039-6028.

[84] Wu, Q, Thissen, A, Jaegermann, W, Schüz, M and Schmidt, PC. Resonant photoemission spectroscopy study of electronic structure of V_2O_5. *Chem. Phys. Let.*, 2006, **430**, 309-313. ISSN 0009-2614.

[85] Netzer, FP. Interfacial oxide layers at the metal-oxide phase boundary. *Surf. Rev. Lett.*, 2002, **9**, 1553-1563. ISSN 0218-625X.

[86] Lovis, F, Hesse, M, Locatelli, A, Mentes, TO, Nino, MA, Lilienkamp, G, Borkenhagen, B and Imbihl, R. Self-organization of ultrathin vanadium oxide layers on a Rh(111) surface during a catalytic reaction. Part II: a LEEM and spectromicroscopy study. *J Phys Chem C*, 2011, **115**, 19149-19157. ISSN 1932-7447.

[87] Schoiswohl, J, Surnev, S, Sock, M, Eck, S, Ramsey, MG, Netzer, FP and Kresse, G. Reduction of vanadium-oxide monolayer structures. *Phys. Rev. B*, 2005, **71**, 165437. ISSN 1098-0121.

[88] Chan, CM, Thiel, PA, Yates, JT and Weinberg, WH. Geometrical and vibrational properties of Rh(111) surface. *Surf. Sci.*, 1978, **76**, 296-310. ISSN 0039-6028.

[89] Eichler, A, Hafner, J, Kresse, G and Furthmuller, J. Relaxation and electronic surface states of rhodium surfaces. *Surf. Sci.*, 1996, **352**, 692. ISSN 0039-6028.

[90] Feibelman, PJ. Electronic-structure of clean and carbon-covered closed-packed rhodium and ruthenium surfaces. *Phys. Rev. B*, 1982, **26**, 5347-5356. ISSN 0163-1829.

[91] Feibelman, PJ and Hamann, DR. Electronic-structure of metal overlayers on rhodium. *Phys. Rev. B*, 1983, **28**, 3092-3099. ISSN 0163-1829.

[92] Arlinghaus, FJ, Gay, JG and Smith, JR. Surface-states on d-band metals. *Phys. Rev. B*, 1981, **23**, 5152-5155. ISSN 0163-1829.

[93] Wei, D, Sanjay, D, Smith, KE and Kevan, SD. Angle-resolved photoemission-study of the clean and hydrogen-covered Rh(111) surface. *Phys. Rev. B*, 1994, **49**(7), 4821-4826. ISSN 0163-1829.

[94] Methfessel, M, Hennig, D and Scheffler, M. Trends of the surface relaxations, surface energies, and work-functions of the 4d transition-metals. *Phys. Rev. B*, 1992, **46**, 4816-4829. ISSN 0163-1829.

[95] Weimer, JJ, Lobodacackovic, J and Block, JH. Phase-diagram and overlayer structures for CO on Rh(110). *Surf. Sci.*, 1994, **316**, 123-142. ISSN 0039-6028.

[96] Dhanak, VR, Baraldi, A, Comelli, G, Paolucci, G, Kiskinova, M and Rosei, R. CO adsorption on unreconstructed and reconstructed Rh(110) surfaces - LEED and XPS studies. *Surf. Sci.*, 1993, **295**, 287-294. ISSN 0039-6028.

[97] Fadley, CS. X-ray photoelectron spectroscopy: from origins to future directions. *Nucl. Instrum. Methods Phys. Res., Sect. A*, 2009, **601**, 8-31. ISSN 0168-9002.

[98] Hirschl, R, Jeanvoine, Y, Kresse, G and Hafner, J. Stability, electronic properties and chemical reactivity of palladium-vanadium(111) surface alloys. *Surf. Sci.*, 2001, **482**, 712-717. ISSN 0039-6028.

[99] Olivier, S, Treglia, G, Saul, A and Willaime, F. Influence of surface stress in the missing row reconstruction of fcc transition metals. *Surf. Sci.*, 2006, **600**, 5131-5135. ISSN 0039-6028.

[100] Dhanak, VR, Comelli, G, Cautero, G, Paolucci, G, Prince, KC, Kiskinova, M and Rosei, R. (1xn) reconstruction of the Rh(110) surface with n = 2, 3, 4, 5. *Chem. Phys. Lett.*, 1992, **188**, 237-240. ISSN 0009-2614.

[101] Baraldi, A, Lizzit, S, Bondino, F, Comelli, G, Rosei, R, Sbraccia, C, Bonini, N, Baroni, S, Mikkelsen, A and Andersen, JN. Thermal stability of the Rh(110) missing-row reconstruction: combination of real-time core-level spectroscopy and ab initio modeling. *Phys. Rev. B*, 2005, **72**, . ISSN 1098-0121.

[102] Prince, KC, Santoni, A, Morgante, A and Comelli, G. A synchrotron-radiation study of NO, CO and hydrogen adsorption on Rh(110). *Surf. Sci.*, 1994, **317**, 397-406. ISSN 0039-6028.

[103] Batteas, JD, Barbieri, A, Starkey, EK, Van Hove, MA and Somorjai, GA. A tensor LEED analysis of the Rh(110)-p2mg(2x1)-2CO structure. *Surf. Sci.*, 1994, **313**, 341-348. ISSN 0039-6028.

[104] Baraldi, A, Comelli, G, Lizzit, S, Cocco, D, Paolucci, G and Rosei, R. Temperature programmed x-ray photoelectron spectroscopy: a new technique for the study of surface kinetics. *Surf. Sci.*, 1996, **367**, L67-L72. ISSN 0039-6028.

[105] Rebholz, M, Prins, R and Kruse, N. Adsorption and dissociation of CO on Rh(210). *Surf. Sci.*, 1991, **259**, L797-L803. ISSN 0039-6028.

[106] Moulder, JF, Stickle, WF, Sobol, PE and Bomben, KD. *Handbook of x-ray photoelectron spectroscopy*. USA: Physical Electronics, 1992. ISBN 0-9648124-1-X.

[107] Nduwimana, A, Gong, XG and Wang, XQ. Relative stability of missing-row reconstructed (110) surfaces of noble metals. *App. Surf. Sci.*, 2003, **219(1-2)**, 129-135. ISSN 0169-4332.

[108] Ho, KM and Bohnen, KP. Stability of the missing-row reconstruction on fcc

(110) transition-metal surfaces. *Phys. Rev. Let.*, 1987, **59**, 1833-1836. ISSN 0031-9007.

[109] Baraldi, A, Dhanak, VR, Comelli, G, Prince, KC and Rosei, R. Comparative-study of the adsorption of CO, NO and hydrogen on (1x1) and (1x2) Rh(110). *Surf. Sci.*, 1993, **293**, 246-253. ISSN 0039-6028.

LIST OF TABLES

LIST OF ABBREVIATIONS

ARUPS: Angle-Resolved Ultraviolet Photoelectron Spectroscopy
BE: Binding Energy
DFT: Density-Functional Theory
DOS: Density of States
DSPS: Department of Surface and Plasma Science
EDJDOS: Energy Distribution of Joint Density of States
FS: Forward Scattering
GFM: Goodfellow Materials
IMFP: Inelastic Mean Free Path
L: Langmuir; a unit of exposure to gas (1 L = 1×10^{-6} Torr during 1s)
LUMO: Lowest Unoccupied Molecular Orbital
LEED: Low Energy Electron Diffraction
MEBES: Micro Electron Beam Evaporation Source
ML: Monolayer
MSB: Materials Science Beamline
PES: Photoelectron Spectroscopy
SBZ: Surface Brillouin Zone
SCLS: Surface Core Level Shift
SRPES: Synchrotron Radiation Photo-Electron Spectroscopy
STM: Scanning Tunnelling Microscopy
TPD: Temperature Programmed Desorption
UHV: Ultra-High Vacuum
UPS: Ultraviolet Photoelectrons Spectroscopy
VB: Valence Band
XPD: X-ray Photoelectron Diffraction
XPS: X-ray Photoelectron Spectroscopy

ATTACHMENT

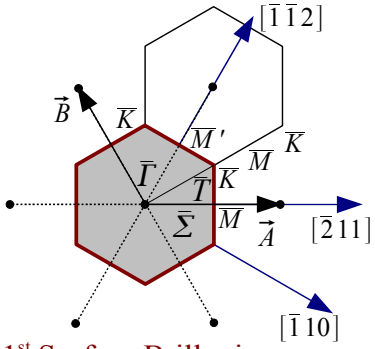

1st Surface Brillouin zone

$a_{Rh} = 3.8034\,\text{Å}$

$|\vec{A}| = |\vec{B}| = 2\sqrt{\frac{2}{3}}\frac{2\pi}{a_{Rh}} = 2.698\,\text{Å}^{-1}$

$|\bar{\Gamma}\bar{M}| = \sqrt{\frac{2}{3}}\frac{2\pi}{a_{Rh}} = 1.349\,\text{Å}^{-1}$

$|\bar{\Gamma}\bar{K}| = \frac{2\sqrt{2}}{3}\frac{2\pi}{a_{Rh}} = 1.557\,\text{Å}^{-1}$

$|\bar{K}\bar{M}| = \frac{\sqrt{2}}{3}\frac{2\pi}{a_{Rh}} = 0.779\,\text{Å}^{-1}$

FCC (111) surface reciprocal lattice. Some surface reciprocal lattice points ($\bar{\Gamma}, \bar{K}, \bar{M}, \bar{M}'$) and directions ($\bar{\Sigma}, \bar{T}$) are indicated together with a few real space directions. On the right, absolute values of some distances at the reciprocal surface are calculated for Rh(111).

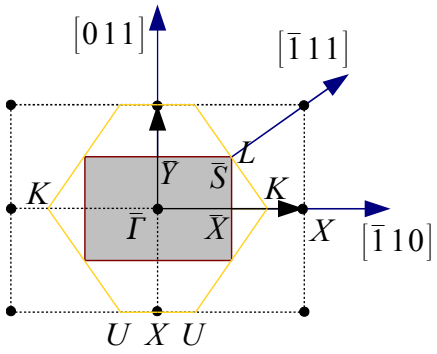

$a_{Rh} = 3.8034\,\text{Å}$

$|\vec{A}| = \sqrt{2}\frac{2\pi}{a_{Rh}} = 2.336\,\text{Å}^{-1}$

$|\vec{B}| = |\Gamma Y| = \frac{2\pi}{a_{Rh}} = 1.652\,\text{Å}^{-1}$

$|\bar{\Gamma}\bar{X}| = \frac{\sqrt{2}}{2}\frac{2\pi}{a_{Rh}} = 1.168\,\text{Å}^{-1}$

$|\bar{\Gamma}\bar{Y}| = \frac{1}{2}\frac{2\pi}{a_{Rh}} = 0.826\,\text{Å}^{-1}$

$|\bar{\Gamma}\bar{S}| = \frac{\sqrt{3}}{2}\frac{2\pi}{a_{Rh}} = 1.431\,\text{Å}^{-1}$

$|\Gamma K| = \frac{\sqrt{2}}{2}\frac{2\pi}{a_{Rh}} = 1.752\,\text{Å}^{-1}$

$|XU| = \frac{\sqrt{2}}{4}\frac{2\pi}{a_{Rh}} = 0.584\,\text{Å}^{-1}$

$\sphericalangle \bar{S}\bar{\Gamma}\bar{X} = 35.3°$

FCC (110) surface reciprocal lattice. Some reciprocal lattice points are indicated together with a few real space directions. The shaded rectangle in the middle represents the first surface Brillouin zone and the yellow lines indicate intersection of bulk Brillouin zone with (110) plane. On the right, absolute values of some distances on the reciprocal surface are calculated for Rh(110).